UNIVERSIDAD MICHOACANA DE SAN NICOLÁS DE HIDALGO

Instituto de Física y Matemáticas

STUDY OF DIRAC MATERIALS UNDER PERTURBATIONS

Tesis que para obtener el grado de
Doctor en Ciencias en el Área de Física

Presenta:
JULIO CÉSAR PÉREZ PEDRAZA

Asesor:
Dr. Alfredo Raya Montaño

Co-asesor:
Dr. José Eduardo Barrios Vargas

MORELIA, MICH., FEBRERO DEL 2024.

Agradecimientos

Agradezco a CONAHCyT por la beca de doctorado con la que fui apoyado, además de su apoyo por medio del proyecto FORDECYT-PRONACES/61533/2020.

Resumen

Los materiales de Dirac, como el grafeno, los aislantes topológicos y los semimetales de Dirac y Weyl, han ganado mucha atención recientemente tanto en la Física de la Materia Condensada como en la Física de Altas Energías debido a sus novedosas propiedades nunca vistas en materiales convencionales, originadas por partículas que siguen una ecuación de movimiento similar a la de Dirac. Además, surgen efectos muy interesantes como resultado de perturbaciones internas y externas en los sistemas Dirac, como la presencia de impurezas, tensiones o interacción de campos electromagnéticos externos con el sistema. Estos efectos son de gran interés en el desarrollo científico y las aplicaciones tecnológicas, ya que se pueden ajustar diferentes propiedades de los materiales, por ejemplo, propiedades de transporte, mecánicas o topológicas. En esta tesis estudiamos tres casos diferentes de materiales de Dirac perturbados: el modelo Su-Schrieffer-Heeger (SSH) con superredes de impurezas incrustadas, la representación no relativista del solitón Jackiw-Rebbi (JR) y los semimetales de Weyl bajo el efecto de campos electromagnéticos paralelos no uniformes generados por SUSY.

Palabras clave: Materiales de Dirac; superredes de impurezas; circuitos topoeléctricos; transformada FW; campos SUSY; quiralidad.

Abstract

Dirac materials, such as graphene, topological insulators and Dirac and Weyl semimetals, have recently gained a lot of attention both in Condensed Matter Physics and High Energy Physics due to their novel properties never seen in conventional materials, originated by particles following a Dirac-like equation of motion. Also, very interesting effect raise as result of internal and external perturbations in Dirac systems, such as presence of impurities, strain, or interaction of external electromagnetic fields with the system. These effects are of great interest in scientific development and technological applications as different properties of the materials, *e.g.* transport, mechanical or topological properties, can be tuned. In this thesis we study three different cases of perturbed Dirac materials: The Su-Schrieffer-Heeger (SSH) model with embedded impurity superlattices, the non-relativistic representation of the Jackiw-Rebbi (JR) soliton, and Weyl semimetals under the effect of SUSY-generated parallel non-uniform electromagnetic fields.

Keywords: Dirac materials; impurity superlattices; topolectrical circuits; FW transform; SUSY fields; chirality.

Contents

List of Figures

Chapter 1

Introduction

One of the cornerstones in Condensed Matter Physics is the low-energy excitations in materials, colloquially known as *band theory*, which has great importance in the intrinsic properties of the materials, as well as their response to external perturbations. In this context, materials can be classified in metals, semimetals, insulators, or semiconductors (see Fig. 1.1), depending on the separation between the valence and conduction bands. Conductors, typically metals, have a finite phase space with overlapping valence and conduction bands (Fig. 1.1a)), and their specific heat increases linearly (to leading order) with the temperature. In semimetals there is no energy gap between valence an conduction bands (Fig. 1.1b)), so that a minimal electric field is needed to generate a current. On the other hand, insulators present a large finite energy gap between valence and conduction bands (Fig. 1.1d)), so that thermally excited electron-hole pairs are exponentially suppressed at low temperatures. In between these, semiconductor materials are found, whose valence and conduction bands are still separated by a finite but not-so-wide energy gap (Fig. 1.1c)), with donor or acceptor levels between them (depending on the material doping) facilitating electron conduction. For the vast majority of metallic and semiconductor materials, the *nearly-free quasiparticles*, including their low-energy excitations, have been extremely successfully described by the Schrödinger equation with Hamiltonian $H_S = \mathbf{p}^2/2m^\star$, where $m^\star$ represents the effective mass. From the Schrödinger Hamiltonian, H_S, it can be noted the quadratic relation between energy and momentum of the particles (Fig. 1.2). These particles are often referred to as "Schrödinger fermions", and the materials constituted by them are colloquially named "conventional materials". Since the successful synthesis of graphene in 2004 [1], the field of Condensed Matter Physics has been going through a rapid expansion of novel materials which do not behave as conventional materials (quadratic energy-momentum relation), presenting low-energy excitations with linear energy-momentum relation (Fig. 1.2). Examples range from superfluid phases of ^{3}He [2, 3], d-wave superconductors [4], to topologi-

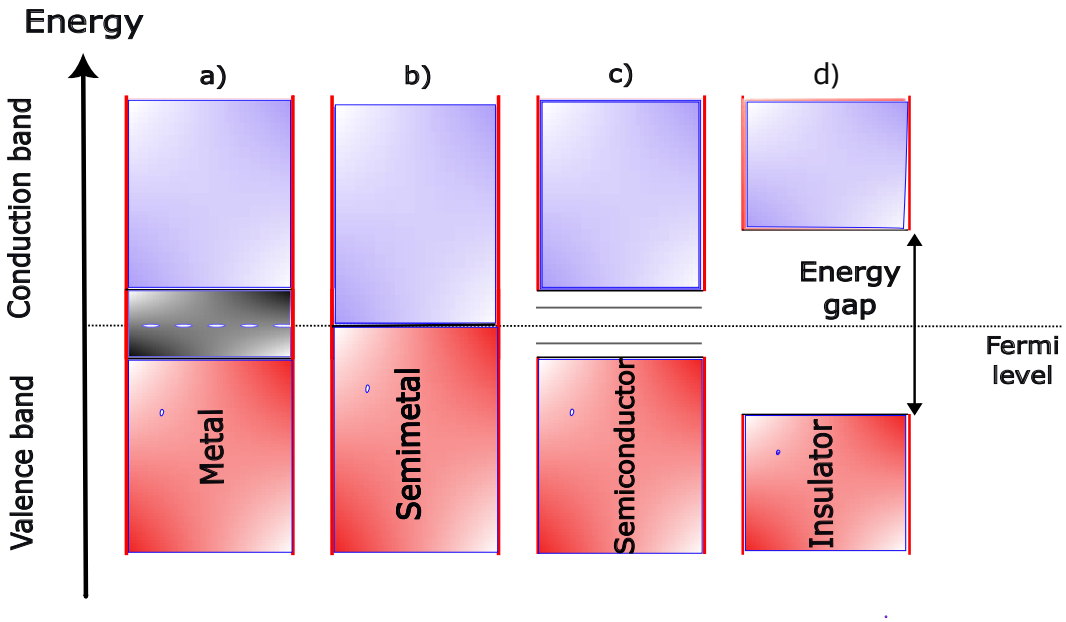

Figure 1.1: Band theory of solids. Valence and conduction bands for metals, semiconductors and insulators. Self-made figure.

cal insulators [5, 6] and Dirac and Weyl semimetals (SM) [7, 8]. The characteristic signature in these materials, as said before, is the linear relation between energy and momentum. Therefore quasiparticles are described by a Dirac-like equation (See Supplement 2.A for a review of the Dirac equation) with the Dirac Hamiltonian

$$H_D = c\boldsymbol{\sigma} \cdot \mathbf{p} + mc^2\sigma_z, \tag{1.1}$$

where $\boldsymbol{\sigma} = (\sigma_x, \sigma_y)$ and σ_z are the Pauli matrices, and c the effective "speed of light" in the material (which actually is the velocity of the conducting particles in the material) given by the Fermi velocity v_{F} ($v_{\mathrm{F}} \approx c/300$, where c is the actual speed of light in vacuum $c = 3 \times 10^8$ m/s). The above-mentioned materials are apparently diverse, but impressively they possess similar universal properties as a consequence of the linear spectrum. Examples of that are the fermionic specific heat relation, the response to impurities, the interaction with external magnetic fields, suppressed backscattering, transport properties, and optical conductivity [9]. Additionally, because of the *spinorial* nature of the Dirac equation governing these systems, electrons and holes are interconnected, having the same effective mass m directly related to the spectral gap $\Delta = 2mc^2$ [10]. This differs from the case of conventional materials where electrons and holes are described by separate Schrödinger equations with different effective masses, and there is no unique relation between gap and mass.

Therefore, systems with both massless and massive Dirac quasiparticle excitations are named as *Dirac materials*.

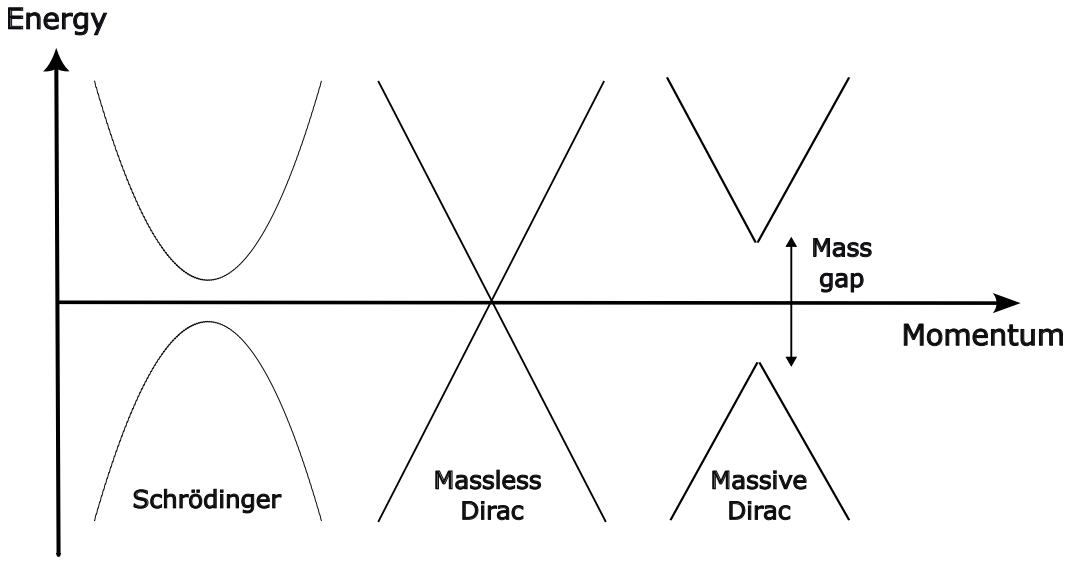

Figure 1.2: Energy-momentum dispersion relation for Schrödinger, massless Dirac and massive Dirac particles. Self-made figure.

Dirac materials have been the object of an enormous amount of studies in the past few years. Their extravagant, novel properties, never seen in conventional materials, have opened the door to possible revolutionary technological applications. Some examples of that are the wide applications of graphene in *spintronics* [11], *valleytronics* [12], *twistronics* [13], mechanical performance improvement [14], solar cells [15], etc.; applications of topological insulators in electronic steering [16], charge pumping [17], etc.; possible realization of high-temperature superconductivity [18]; among many other. On the other hand, from the scientific point of view, relativistic quantum mechanic effects (a quick review of relativistic quantum mechanics is shown in Supplement 2.A) can be tested in these materials. This is the case of the already tested Klein paradox (suppressed backscattering) [19] and the Zitterbewegung [20]. Additionally, the effects of external perturbations over the system generate fascinating, never-seen effects. Some examples are the quantization of the energy by the action of an external magnetic field perpendicular to a graphene sheet (Landau levels) [21], the *atomic collapse phenomenon* due to the presence of electrical impurities in graphene [22], the effects of strain in graphene [22, 23], the effects of electromagnetic fields in Weyl semimetals such as the Chiral Magnetic Effect (CME) [24] and the planar Hall Effect (PHE) [25], or even the presence of a chiral anomaly (some words on the chiral anomaly are presented in Supplement 2.C)

in Weyl semimetals as a result of external pseudo- and electromagnetic fields [26, 27]. In conclusion, Dirac materials are a fertile field with a high potential for technological and scientific development.

The goal of this thesis is to study some Dirac materials systems which are exposed to some perturbation. The work is presented as follows: In Chapter 2, we give a general description of different classes of Dirac materials, starting with the wide-studied graphene sheet; some topological insulators, in particular the case of the Su-Schrieffer-Heeger (SSH) model, the Jackiw-Rebbi (JR) model, the Kane-Mele model and the Haldane model; and 3D Dirac and Weyl semimetals. We treat its microscopic origin, experimental realization, symmetries, etc. We have included some important topics about the universal properties of Dirac materials and novel transport effects in Weyl semimetals. Next, in Chapter 3, we tackle the problem of the SSH chain with impurity superlattices, in which we study the effect of different settings of hopping parameters, superlattice length, and position of the impurity in the supercell over the topological properties and chiral symmetries of the system. In Chapter 4, the study of the non-relativistic representation of the Jackiw-Rebbi soliton is presented. In this case, the non-relativistic wave functions are computed through a Foldy-Wouthuysen transformation. In Chapter 5, we present the study of a novel Chiral Planar Hall effect generated by the effect of external Supersymmetric parallel electromagnetic fields in a type-I Weyl semimetal. We obtained the corresponding chiral densities and current probabilities and gave a visualization of the effect. At the end of Chapters 2, 3, and 5, we have added some related topics through Supplements, which help to better understand or develop the problem. Next, in Chapter 6, we discuss the obtained results and state some general conclusions. Finally, in Chapter 7, we discuss some future/in-process work that we are carrying out.

Chapter 2

Dirac Materials

2.1 Introduction

Dirac materials consist of all the Condensed Matter Physics systems whose charge carriers follow a linear Energy-Momentum dispersion relation, therefore being described by an effective Dirac equation. Dirac materials study has increased exponentially in the last few years owing to its high potential for technological and scientific applications. A variety of Dirac materials have been discovered recently, ranging from exotic quantum fluids to crystalline solids (c.f. Table 2.1).

As seen in Table 2.1, graphene, Silicene, and Germanene, as well as "artificial" graphene, are produced in the same crystalline order. On the other hand, topological insulators (TIs) present a fully gapped energy in the bulk but Dirac excitations at the surface. In the case of 3D Dirac materials, which have gained a lot of attention in recent years, if we consider the chiral symmetry of the system, the equation becomes a Weyl equation, and the materials with this spectrum at low-energies are then called Weyl semimetals (WSMs). If there exists a band degeneracy at the Dirac nodal point (without opening a gap), the materials are called 3D Dirac semimetals (DSMs).

Even though Dirac materials are widely different in nature, the observed similarity of the low-energy spectrum points to a powerful organizing principle. In fact, they are the symmetries of the systems which control the formation or annihilation of Dirac nodes. These symmetries differ in each material, such as time-reversal (TR) symmetry in TIs and sublattice symmetry in graphene. As a unifying principle, the presence of nodes leads to a sharp reduction of phase space dimensionality controlled by symmetries at low-energy for zero-energy excitations.

From the point of view of applications, first, it is possible to lift the protected

Material	Pseudospin	Energy scale	Refs.
Graphene, silicene, germanene	Sublattice	1-3 eV	[28, 29, 30, 31, 32]
Artificial graphenes	Sublattice	10^{-8}-0.1 eV	[33, 34, 35, 36, 37]
Hexagonal layered heterostructures	Emergent	0.01-0.1 eV	[38, 39, 40]
Hofstadter butterfly systems	Emergent	0.01 eV	[41]
Graphene–hBN heterostructures in high magnetic fields			
Band inversion interfaces: SnTe/PbTe, CdTe/HgTe, PbTe	Spin-orb. ang. mom.	0.3 eV	[42, 43, 44]
2D topological insulators: HgTe/CdTe, InAs/GaSb, Bi bilayer,...	Spin-orb. ang. mom.	<0.3 eV	[5, 6, 45, 46]
3D topological insulators: Bi1-xSbx, Bi2Se3, strained HgTe, Heusler alloys, ...	Spin-orb. ang. mom.	$\lessapprox$0.3 eV	[5, 6, 46, 47]
Topological crystalline insulators: SnTe, Pb1-xSnxSe	Orbital	$\lessapprox$0.3 eV	[48, 49]
d-wave cuprate superconductors	Nambu pseudospin	$\lessapprox$0.5 eV	[50, 51]
^{3}He	Nambu pseudospin	0.3 μeV	[2, 3]
3D Weyl and Dirac SM Cd3As2, Na3Bi	Energy bands	Unclear	[52, 53, 54]

Table 2.1: Dirac materials indicated by material family, pseudo-spin realization in the Dirac Hamiltonian, and the energy scale for which the Dirac spectrum is present without any other states. Adapted from [55].

symmetry of the Dirac node opening a gap that dramatically changes the material response [56]. Second and also very important is the fact that Dirac nodes suppresses dissipation.

This Chapter is organized as follows: In Sects. 2.2-2.4, we describe three rep-

resentative cases of Dirac materials, graphene, TIs (in particular the Su-Schrieffer-Heeger (SSH) model and the Jackiw-Rebbi (JR) model), and WSMs, respectively. We discuss the microscopic origin of the Dirac excitations, and the mass generation mechanisms and experimental realizations of each case. We have included three Supplements: In Suppl. 2.A, we review the historical development of relativistic quantum mechanics, finishing with the Dirac equation. In Suppl. 2.B, we review some universal properties that are present in Dirac materials. In Suppl. 2.C, we present some novel transport effects in WSMs.

2.2 Graphene

Undoubtedly, graphene is the most famous Dirac material. It consists of a two-dimensional layer of carbon atoms tightly packed in a honeycomb lattice (Fig. 2.1 (a)). If we only consider nearest-neighbor couplings in the sheet, then the lattice can be considered as bipartite, consisting of two triangular sublattices of atoms A and B, with the unit cell containing one of each atom species (Fig. 2.1 (a)).

For the case of pristine graphene, the primitive vectors generating the Bravais lattice are

$$\boldsymbol{a_1} = \frac{a}{2}(3, \sqrt{3}), \quad \boldsymbol{a_2} = \frac{a}{2}(3, -\sqrt{3}), \tag{2.1}$$

where a is the interatomic distance ($a \approx 1.42$Å) [57, 58]. Also, the vectors joining atoms with its three nearest-neighbors are

$$\boldsymbol{\delta_1} = \frac{a}{2}(3, \sqrt{3}), \ \boldsymbol{\delta_2} = \frac{a}{2}(3, -\sqrt{3}), \ \boldsymbol{\delta_3} = -a(1, 0). \tag{2.2}$$

Thus, any point in the honeycomb lattice can be represented by a traslation $\boldsymbol{T} = n\boldsymbol{a_1} + m\boldsymbol{a_2} + \boldsymbol{\delta_3}$, with n, m integers.

From the definition of the reciprocal lattice, $\boldsymbol{a_i} \cdot \boldsymbol{b_i} = 2\pi\delta_{ij}$, we obtain the basis vectors of the reciprocal space

$$\boldsymbol{b_1} = \frac{2\pi}{3a}(1, \sqrt{3}), \quad \boldsymbol{b_2} = \frac{2\pi}{3a}(1, -\sqrt{3}). \tag{2.3}$$

In this case, the First Brillouin Zone (FBZ) has also hexagonal shape (Fig. 2.1 (b)), with the high-symmetry points:

$$\boldsymbol{K} = \frac{2\pi}{3a}\left(1, \frac{1}{\sqrt{3}}\right), \ \boldsymbol{K'} = \frac{2\pi}{3a}\left(1, -\frac{1}{\sqrt{3}}\right), \ \boldsymbol{M} = \frac{2\pi}{3a}(1, 0), \ \boldsymbol{\Gamma} = (0, 0). \tag{2.4}$$

As we will see later, the points $\boldsymbol{K}$, $\boldsymbol{K'}$ are the well-known Dirac points.

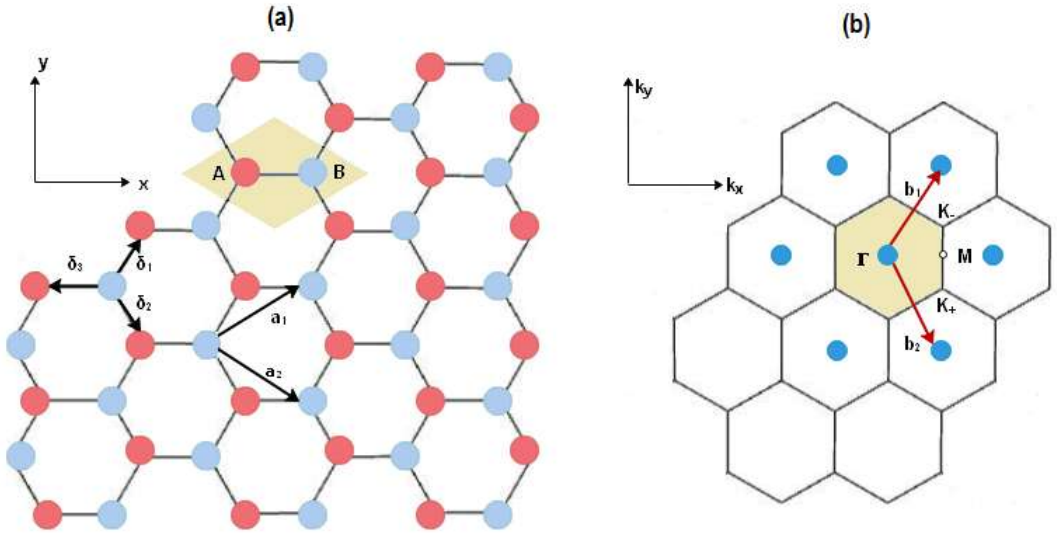

Figure 2.1: (a) Hexagonal graphene lattice formed by two triangular sublattices A and B. The primitive vectors $\mathbf{a}_1$ and $\mathbf{a}_2$, along with the vectors that join both sublattices, $\boldsymbol{\delta}_i$ are shown. (b) FBZ of the graphene lattice. Some important points ($\mathbf{\Gamma}$, $\mathbf{K}_-$, $\mathbf{K}_+$, $\mathbf{M}$) are also drawn. Figure taken from [59].

2.2.1 Electronic properties and Energy-momentum relation

Let us have a look at the electronic properties of carbon. First, its electronic configuration is $1s^2 2s^2 2p^2$, where $1s$ electrons are strongly bound to the nucleus; the remaining four electrons can hybridize in different forms, resulting in materials with different properties [28]. For example, when the four free electrons (orbitals) mix, sp^3 hybridization occur, forming the diamond structure's strong covalent bounds. In the case of graphene with a sp^2 hybridization of orbitals, it results in a string plane of σ-bonds and perpendicular weaker π-bonds formed by p_z orbitals. The π-bonds are responsible for the formation of the π-bands in the dispersion relation of graphene, as shown next.

To obtain the energy-momentum dispersion relation, we part from the Tight-Binding Hamiltonian [55]

$$\hat{H} = -t \sum_{\langle ij \rangle} a_i^\dagger b_j + a_j^\dagger b_i, \tag{2.5}$$

where a, b ($a^\dagger, b^\dagger$), annihilate (create) electrons in the unit cell i in sublattices A and B, respectively [57]. Here, t is the hopping to nearest-neighbours ($t \approx 2.7$ eV). As there are two atoms per unit cell, the Hamiltonian is represented by a 2×2 matrix

in momentum space representation

$$\begin{pmatrix} 0 & \zeta(\boldsymbol{k}) \\ \zeta^{\star}(\boldsymbol{k}) & 0 \end{pmatrix}, \tag{2.6}$$

with $\zeta(\boldsymbol{k}) = -t\left(e^{i\boldsymbol{\delta_1}\cdot\boldsymbol{k}} + e^{i\boldsymbol{\delta_2}\cdot\boldsymbol{k}} + e^{i\boldsymbol{\delta_3}\cdot\boldsymbol{k}}\right)$ (note that we have made use of the Bloch's theorem). The three terms represent the hopping processes connecting each atom in sublattice A with its nearest-neighbors in sublattice B through the vectors $\boldsymbol{\delta_i}$, and vice-versa. The energy bands result to be (for details please see Ref. [59])

$$E(\boldsymbol{k}) = \pm|\zeta(\boldsymbol{k})| = \pm t\sqrt{2\cos(\sqrt{3}ak_y) + 4\cos(\frac{\sqrt{3}}{2}ak_y)\cos(\frac{3}{2}ak_x) + 3}, \tag{2.7}$$

which is depicted in Fig. 2.2.

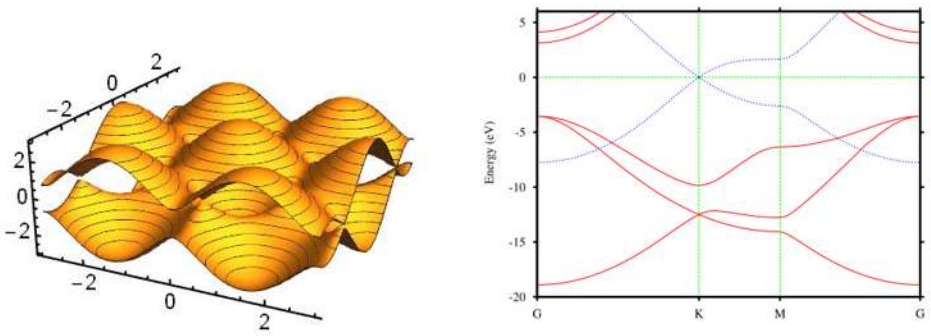

Figure 2.2: (Left) Three-dimensional energy-momentum dispersion bands, where valence and conduction bands touch in the Dirac points. (Right) Typical two-dimensional slice of the energy-momentum dispersion bands. Adapted from [59].

The dispersive terms vanishes in two inequivalent corners in the FBZ, *i.e.* $\boldsymbol{k}$ and $\boldsymbol{k'} = -\boldsymbol{k}$, known as Dirac points, where the two bands are degenerate at the Fermi level $E = 0$.

It can be demonstrated (see [59]) that an expansion of the Hamiltonian in the vicinity of the Dirac points yields

$$H(\pm\boldsymbol{k} + \boldsymbol{q}) = \hbar v_{\mathrm{F}} \begin{pmatrix} 0 & q_x \pm iq_y \\ q_x \mp iq_y & 0 \end{pmatrix}, \tag{2.8}$$

with $\boldsymbol{q}) = (q_x, q_y)$ a vector given in reciprocal space [60]. Equation (2.8) corresponds to a 2D massless Dirac Hamiltonian (Eq. (1.1)). Experimental evidence of the Dirac spectrum in graphene has been obtained through angled-resolved photo-emission

spectroscopy (ARPES), and scanning tunneling spectroscopy (STS) (references can be found in [55]).

Graphene possesses four flavor Dirac fermions: two (electron) spin degenerate cones in each of the two valleys $\pm\boldsymbol{k}$. The pseudospin degree of freedom corresponds to the sublattice. Also, a 2π rotation of the graphene sheet causes the pseudospin to acquire a phase of π, similar to the spin-1/2 particles [61].

2.2.2 Stability of the Dirac spectrum

As seen, the emergence of Dirac cones in graphene is due to two ingredients: first, the destructive interference of the three nearest neighbor hoppings at the Dirac points, and second, the absence of a mass term (mass gap) entering as σ_z. The latter is a consequence of the fact that the two sublattices transform into each other under real-space inversion, and are therefore equivalent. The inversion transformation in momentum space is then given by

$$I \ : \ H(\boldsymbol{k}) = \sigma_x H(-\boldsymbol{k})\sigma_x. \tag{2.9}$$

In the absence of magnetic field, the system also possesses time-reversal (TR) symmetry

$$T \ : \ H(\boldsymbol{k}) = H^\star(-\boldsymbol{k}). \tag{2.10}$$

The combination of both symmetries results in

$$TI \ : \ H(\boldsymbol{k}) = \sigma_x H^\star(\boldsymbol{k})\sigma_x, \tag{2.11}$$

forcing the terms proportional to σ_z to vanish in Eq. (1.1) [62].

If, on the other hand, sublattice asymmetry (chiral symmetry breaking) is present in graphene, the Dirac spectrum is gapped, *i.e.* a mass generation takes place. Many theoretical and experimental mechanisms have been shown to generate mass in graphene. Some examples are: theoretically, a Semenoff gap [60] caused by forced inequivalence of the sublattices through a staggered scalar potential, and a Haldane gap [63] where TR is broken by a staggered magnetic field; experimentally, sublattice-dependent substrates can cause the desired sublattice symmetry breaking [63, 64], as well as spin-orbit couplings [65, 66, 67], long-range Coulomb interactions [68], and finite-size confinement effects [69].

Apart from mass terms induced by symmetry breaking, it is also possible to induce a gap by merging two Dirac cones, a process in which the Berry phases of each cone annihilate each other, resulting in a progressively SM to insulator transition. This can be accomplished, as shown in Fig. 2.3 by increasing the value of one of the hopping parameters. For the case in Fig. 2.3, the two cones converge at $t' = 2t$ [70], with the spectrum linear in one direction and quadratic in the other [71]. This can also be accomplished through strains in the graphene sheet [34].

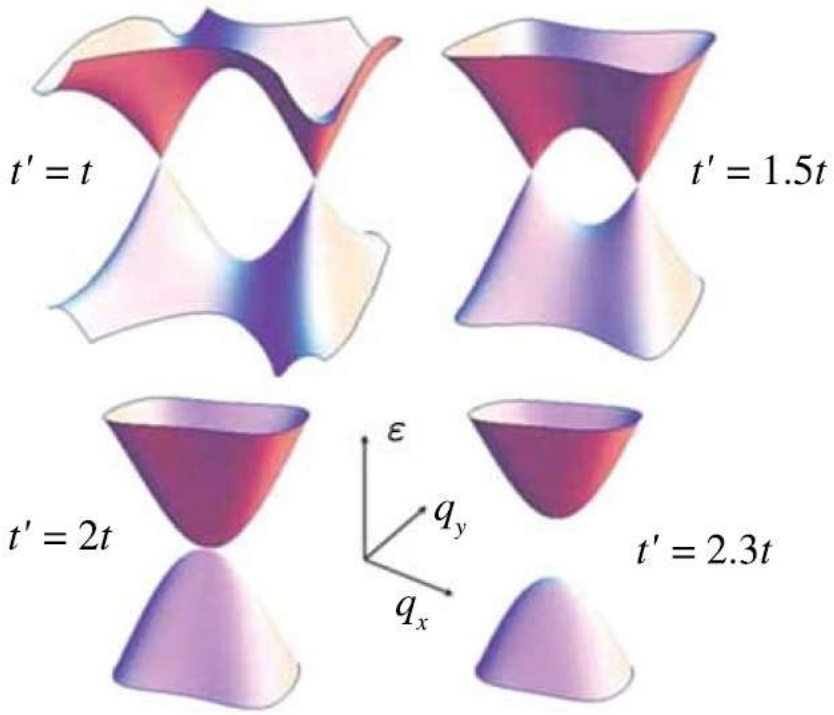

Figure 2.3: Evolution of the Dirac cones while third-neighbour interactions are increased. For $t' = 2t$ the spectrum becomes quadratic and for $t' > 2t$ an energy gap starts to open. Figure adapted from [55].

2.3 Topological Insulators

We base the following discussion on Refs. [55, 5, 72]. Historically, one of the main goals in Condensed Matter Physics has been the discovery and classification of different phases of matter. The usual classifications are generally based on the electric, magnetic, optical, or even transport properties of materials. However, since the discovery of the quantum Hall effect (QHE) in 1980, a new classification paradigm came to the scene based on the notion of *topological order* [73, 74]. During the QHE no symmetry is broken, but a new topological phase is defined in the sense that certain properties (Hall conductance and the number of gapless boundary nodes) are not affected by smooth changes in the material. This opened the door to a new kind of materials dubbed as topological insulators (TIs).

TIs have recently gained a lot of attention not only because of their topological nature, but also because they present the Dirac spectrum. Its main characteristic is that in the bulk valence and conduction bands are separated by a finite gap in all the

FBZ, behaving as an insulator; on the other hand, the surface of the material hosts Dirac surface states closing the gap between the bands (see Fig. 2.4). The surface states have a spin locked to the momentum, resulting in a spin-helical metal.

TIs are strongly spin-orbit coupled materials that preserve TR symmetry. Because of the Kramers' degeneracy, for a given energy, there exists a pair of states with opposite momenta and spins, where the backscattering between them is forbidden.

As the name suggests, TIs are related to the topological properties of the material. Insulators can be classified into topological equivalence classes characterized by a topological invariant $\nu \in \mathbb{Z}_2$ (Kane and Mele [75]), where ν is a bulk property taking the values $\nu = 0, 1$ [75, 76, 77]. The materials with $\nu = 1$, which present robustness against disorder or impurities, are denoted "topological insulators", whereas materials with $\nu = 0$ are called "normal insulators".

Two insulators are defined to be topologically equivalent if their Hamiltonians can be smoothly deformed into each other without closing the energy gap. In general, n-dimensional TIs host $n-1$-dimensional gapless edge states.

The simplest model of a TI consists of two copies of the Hamiltonian (1.1) describing a pair of counter-propagating time-reversed states

$$H_{TI}(\boldsymbol{k} = \begin{pmatrix} H(\boldsymbol{k}) & 0 \\ 0 & H^{\star}(-\boldsymbol{k}) \end{pmatrix}. \tag{2.12}$$

By means of a unitary transformation, $\sigma_y H^{\star}(-\boldsymbol{k})\sigma_y = v_{\mathrm{F}}\boldsymbol{k}\cdot\boldsymbol{\sigma} - m\sigma_z$, equivalente to $H(\boldsymbol{k})$ for the $m = 0$ case.

2.3.1 Stability of the Dirac spectrum

In TI's, a gap can be opened by breaking TR symmetry. Theoretically, magnetic fields and magnetic impurities have been proposed to open a gap in these materials. However, it has not been visualized experimentally. On the other hand, confinement effects, as well as strain engineering effects, have been experimentally confirmed to produce a gap. Additionally, the effects of circularly polarized light, which evidently breaks TR, present the gap-opening effects (references about these studies can be found in [55].

Fu and Kane proposed $Bi_{1-x}Sb_x$ as the first candidate of a 3D TI [47], which was later experimentally verified [78]. Also, Zhang *et al.* [79] and Xia *et al.* [80] predicted that Bi_2Te_3 and Bi_2Se_3 were topological insulators with a single Dirac cone of surface states, behavior that was posteriorly proven by means of ARPES [80, 81].

Reducing the system to one dimension is very helpful to gain insight into topological properties. In the next section, we review the Su-Schieffer-Heeger model (SSH) [82], which consists of a one-dimensional chain presenting topological features. Then, we present the continuum representation of the SSH model, the Jackiw-Rebbi (JR) model.

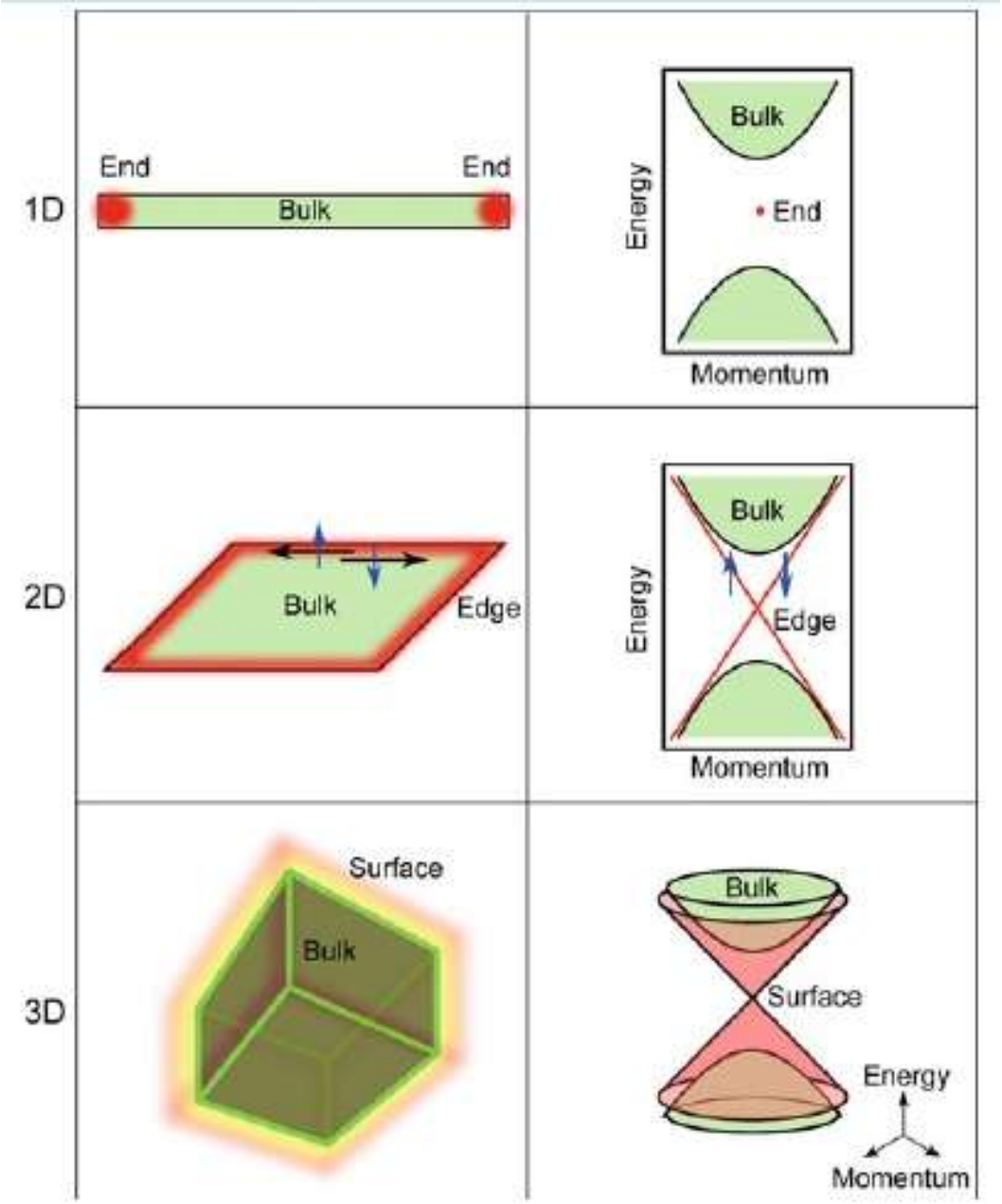

Figure 2.4: Boundary states and associated energies of d-dimendional topological insulators. Figure adapted from [72].

2.3.2 SSH Model

The Su-Schrieffer-Heeger (SSH) model [82] is one of the simplest models which behaves as a topological insulator, and it describes the behavior of spinless fermions hopping on a one-dimensional lattice with staggered hopping amplitudes v,w (such as the polyacetylene molecule (Fig. 2.5)). The chain consists of N unit cells, each one containing two sites labeled as A and B (sublattices), as shown in Fig. 2.5. This

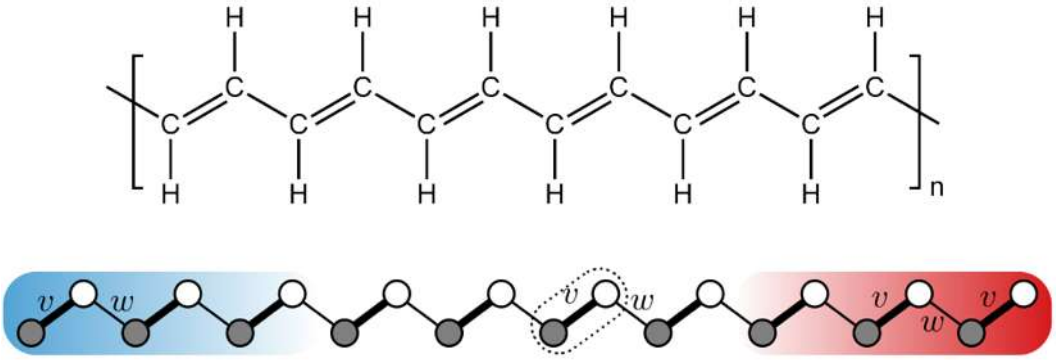

Figure 2.5: Top: polyacetylene molecule. Bottom: SSH model with staggered hoppings v, w. The unit cell contains one atom of each specie, A, B (dotted line). Adapted from Ref. [82].

model preserves chiral symmetry, *i.e.* a combination of particle-hole (charge conjugation, C) and TR symmetry. If we consider the Peierls' theorem, which states that a one-dimensional equally-spaced chain with one free electron per ion is unstable due to lattice distortion, the SSH model becomes energetically favorable to form a dimerized lattice, with the new band gap outweighing the elastic energy, making the system physically stable. This model is described by the Hamiltonian

$$H_{SSH} = v \sum_{m=1}^{N} (|m, B\rangle\langle m, A| + h.c.) + w \sum_{m=1}^{N-1} (|m+1, A\rangle\langle m, B| + h.c.), \tag{2.13}$$

where N is the number of unit cells in the chain. Performing the Fourier transform

$$|a_k\rangle = \frac{1}{\sqrt{N}} \sum_n e^{-ikna} |n, A\rangle, \;\; |b_k\rangle = \frac{1}{\sqrt{N}} \sum_n e^{-ikna} |n, B\rangle, \tag{2.14}$$

we obtain the k-space Hamiltonian

$$\begin{aligned} H =& v\sum_k \left(|a_k\rangle\langle b_k| + |b_k\rangle\langle b_k|\right) + w\sum_k \left(e^{-ik}|a_k\rangle\langle b_k| + e^{ik}|b_k\rangle\langle b_k|\right) \\ =& v\sum_k \left(|a_k\rangle\langle b_k| + |b_k\rangle\langle b_k|\right) + w\sum_k \left[\cos(k)(|a_k\rangle\langle b_k| + |b_k\rangle\langle a_k|\right) \\ & -i\sin(k)|a_k\rangle\langle b_k| + i\sin(k)|b_k\rangle\langle a_k|] \\ =& \sum_k \langle\Psi|[(v + w\cos(k))\sigma_x + w\sin(k)\sigma_y]|\Psi\rangle, \end{aligned} \tag{2.15}$$

where in the last equality we have defined the spinor

$$|\Psi\rangle = \begin{pmatrix} |a_k\rangle \\ |b_k\rangle \end{pmatrix}. \tag{2.16}$$

Equation (2.15) consists in a massless Dirac Hamiltonian $H = \boldsymbol{d}(k)\cdot\boldsymbol{\sigma}$ with the vector $\boldsymbol{d} = (d_x, d_y) = (v + w\cos(k), w\sin(k))$, resulting in eigenenergies given by

$$E = \pm\sqrt{d_x^2 + d_y^2} = \pm\sqrt{v^2 + w^2 + 2vw\cos k}, \tag{2.17}$$

as shown in Fig. 2.6 (top). It is easy to check that

$$\sigma_z H \sigma_z = -H, \tag{2.18}$$

which shows the chiral symmetry of the model. The (negative band) eigenstates are

$$\phi = \frac{1}{\sqrt{2}} \begin{pmatrix} sgn(d_x)\sqrt{1 - \frac{dx}{\sqrt{dx^2+d_y^2}}} \\ -\sqrt{1 + \frac{dx}{\sqrt{dx^2+d_y^2}}} \end{pmatrix}. \tag{2.19}$$

As seen in Fig. 2.6(top), as we change the values of v, w from $v > w$ to $v < w$, the dispersion relation looks the same, but the topological nature has suffered a phase change. This is observed by measuring the Berry phase

$$\gamma = \int_{-\pi}^{\pi} dk\langle\phi|i\partial_k|\phi\rangle = \begin{cases} \pi, & v < w, \\ 0, & v > w. \end{cases} \tag{2.20}$$

As shown in Fig. 2.6(bottom), the path of the $\boldsymbol{d}(k)$ vector gives a more intuitive form of the topological phases: when the circle of radius w and centred in v encloses the origin (*i.e.* $v < w$), the Berry (Zak) phase is equal to π, and the system is topologically non-trivial. On the other hand, if the circle does not enclose the origin,

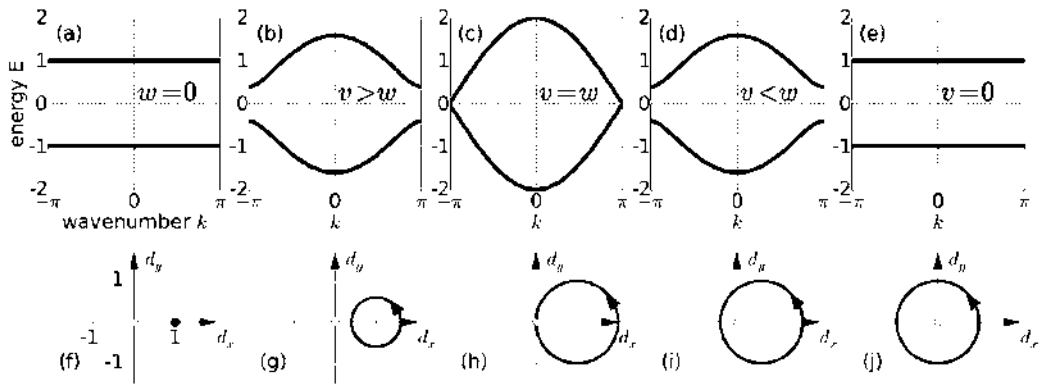

Figure 2.6: Top: energy bands. Bottom: Path of the vector $\mathbf{d}(k)$ representing the bulk momentum-space Hamiltonian. Adapted from [82].

then $\gamma = 0$, and the system is topologically trivial. Therefore, a topological phase change is suffered at the values $v = \pm w$, as shown in Fig. 2.7(e).

The existence of edge states at the ends of the finite chains is characteristic of the topological phase, that is, when the Berry phase is equal to π (the winding number is equal to 1). In Fig. 2.7(a), we can observe the appearance of these edge states at zero energy and the correspondent wave function localization of edge states (b) and (c) and bulk states (d).

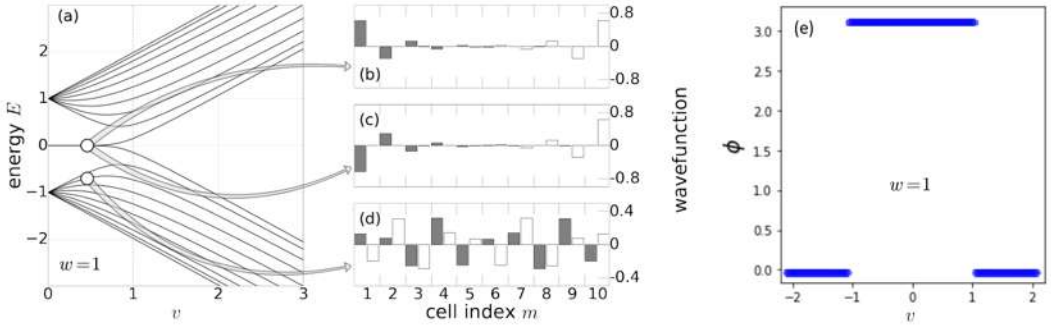

Figure 2.7: (a) Energy spectrum as a function of the v parameter, and (b)-(d) wave functions of a finite SSH model. (e) Zak number as a function of the v parameter. In al cases $w = 1.0$ was fixed. Adapted from [82].

However, the most famous excitations in the model are the soliton and anti-soliton, which present at the continuum limit of the SSH model in which two domains with opposite signs of the mass are separated by an interface. In the next subsection we present this model, known as the Jackiw-Rebbi (JR) model.

2.3.3 Jackiw-Rebbi Model

The Jackiw-Rebbi (JR) model [82] is a relativistic theoretical model of great historical relevance as it is considered one of the first models describing a TI. It consists of a one-dimensional Dirac equation coupled to a soliton field $\phi(x)$ which can be written in terms of an effective Dirac equation with a position dependent mass $m(x) \propto \phi(x)$ such that as $x \to -\infty$, $m(-x) \to -m_0$ whereas as $x \to \infty$, $m(x) \to m_1$, where $m_{0,1} \geq 0$ are constants which might in general be different. Assuming that the soliton field has no dynamics, one usually starts from the Dirac Hamiltonian

$$H_0 \equiv \alpha p_x + \beta m\left(x\right), \tag{2.21}$$

with the Dirac matrices obeying $\alpha^2 = \beta^2 = I_{2\times 2}$, where $I_{2\times 2}$ stands for the identity matrix. In solving

$$H_0\psi = E\psi, \tag{2.22}$$

we first consider the possibility of zero modes, $E = 0$. Thus,

$$\left(\alpha p_x + \beta m\left(x\right)\right)\psi_0 = 0. \tag{2.23}$$

By letting

$$\psi_0 = g\left(x\right)\chi \tag{2.24}$$

with $\alpha\beta\chi = -i\chi$, we straightforwardly find that

$$\psi_0\left(x\right) = e^{-\int_{x_0}^{x} dy\ m(y)}\chi, \tag{2.25}$$

which exhibits a kink behavior (see Figure 2.8 for the case of the step-function mass around the origin) around the point where $\phi(x) = m(x) = 0$, namely, when energy bands show no gap.

Far from this point, energy bands develop such a gap. Moreover, a truly remarkable property of this kink is that it describes a fractionally charged excitation [83], a phenomenon that was discussed even before the Fractional Quantum Hall Effect was discovered [84]. JR model has been realized experimentally in polyacetylene [85] and emerges naturally as the continuum limit of the SSH model for the electron-phonon interaction in these materials. It is also worth mentioning that it has renewed interest in connection with the physics of topological insulators [86, 87] since the gap closing resembles the emergence of topologically protected surface mode on these materials. Optical analogues of the JR model have been proposed [88, 89, 90, 91], whereas an electrostatic analogue was discussed in [92]. The cylindrical generalization of the model, namely, the so-called Dirac wires, was first introduced in [93]. The JR model has also been found as a non relativistic limit of some topological superconductors [94].

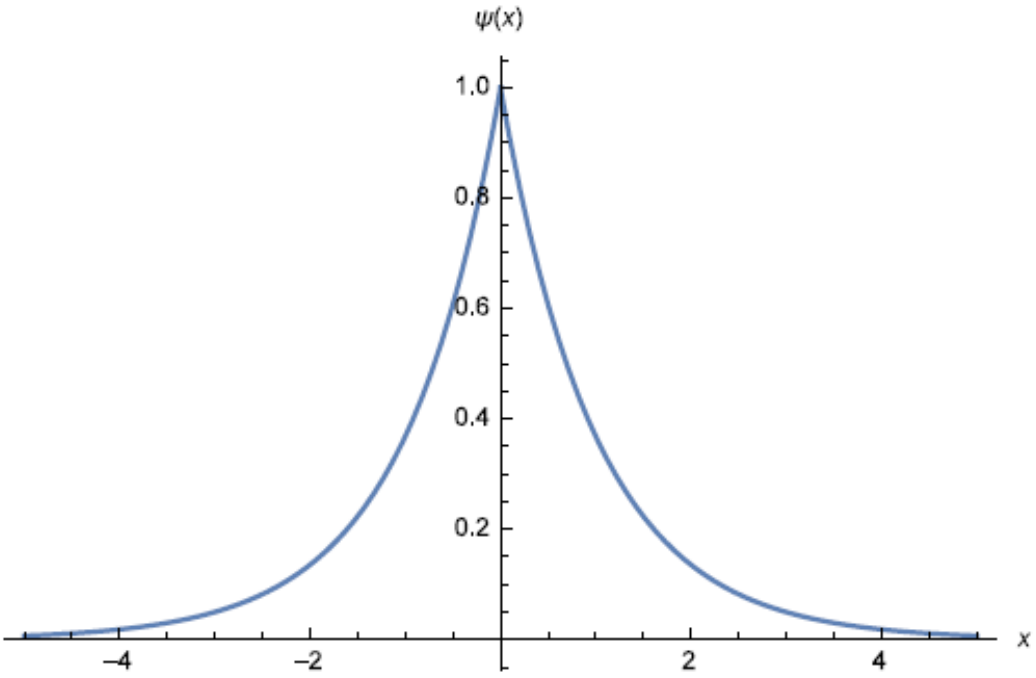

Figure 2.8: Wave function solution of the JR model for the case of the step-function mass around the origin. This behaviour is colloquially known as *kink*.

2.4 Dirac and Weyl Semimetals

As we have seen, there exist materials with a linear energy momentum dispersion relation (Dirac spectrum) in (2+1)-D as is the case of graphene and some topological insulators, and even in (1+1)-D such as the presented SSH model. If we now focus on (3+1)-D, a typical massless Dirac Hamiltonian is

$$H_D = \begin{pmatrix} 0 & v_{\mathrm{F}}\boldsymbol{\sigma}\cdot\boldsymbol{p} \\ v_{\mathrm{F}}\boldsymbol{\sigma}\cdot\boldsymbol{p} & 0 \end{pmatrix}. \tag{2.26}$$

We see that H is equivalent to having two double degenerate Dirac cones at the same point. Materials following this kind of Hamiltonian are called Dirac semimetals (DSM) [77, 95, 96]. It is important to point out that in these Dirac points both inversion (P) and TR symmetries are preserved, and they are responsible for the Dirac spectrum.

However, in 1929, only one year after the Dirac equation was formulated, Hermann Weyl proposed a simplification of the Dirac equation, in which, the degeneration can be lifted by breaking either P or TR symmetries. This gives rise to two

Weyl nodes with opposite chiralities described by the massless Weyl Hamiltonian

$$H_W = v_{\mathrm{F}}\boldsymbol{\sigma}\cdot\boldsymbol{p} = v_{\mathrm{F}}(\sigma_x p_x + \sigma_y p_y + \sigma_z p_z). \tag{2.27}$$

The band touching points can move around in momentum space as effect of perturbations, but the only way to gap out and disappear them is by annihilation with another node of opposite chirality. Materials of this type are known as Weyl semimetals (WSMs) [7, 97, 98, 99, 100, 101].

WSMs present unusual metallic surface states called *Fermi arcs*, which connect both Weyl nodes. As we will see later, these Fermi arcs are topologically protected by an invariant related to the bulk electronic wave functions of the material (similar to the Berry phase in TI's), known as *Chern number*. Figure 2.9 presents a schematic abstract of TI's and DSM/WSM materials.

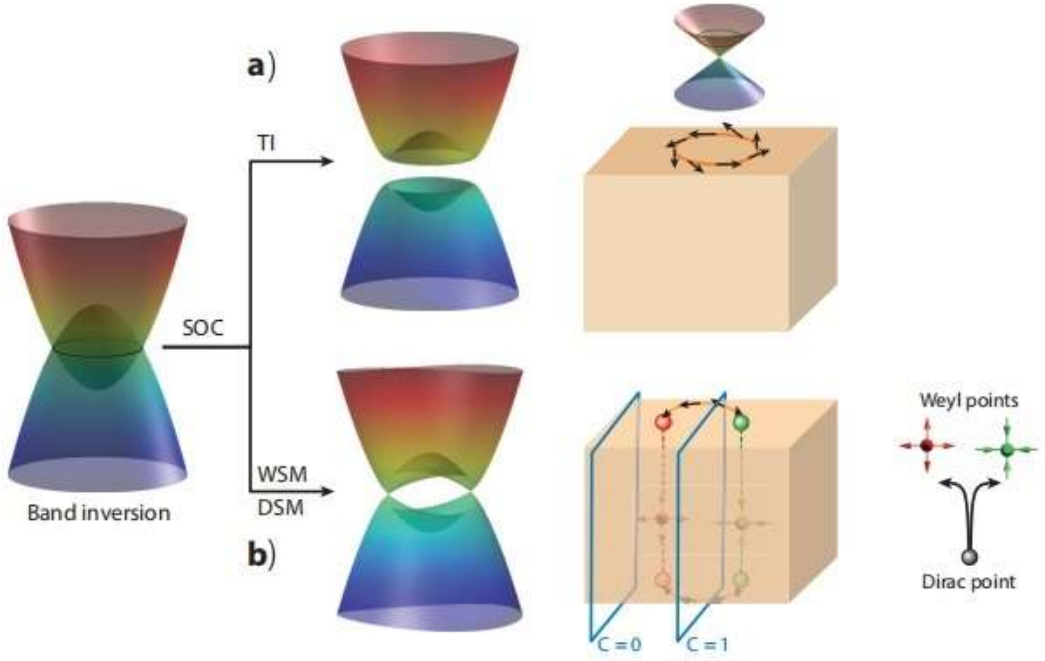

Figure 2.9: a) Topological insulators and b) Weyl or Dirac semimetals as result of spin-orbit coupling, generating for the former surface metallic states and for the latter novel conduction states, Fermi arcs. Adapted from [102].

In WSMs, the wave function of a fermion state acquires a geometric or Berry phase when tracing a closed loop in momentum space. This Berry phase is identical to that acquired by an electron tracing out a closed loop in the presence of a magnetic monopole. In this analogy with the magnetic monopole representing a

source or a sink of magnetic flux, we can think that WSMs host momentum-space monopoles (*pseudo-magnetic monopoles*) corresponding to sources or sinks of Berry curvature. These Berry curvature monopoles are precisely the nodes of the WSM. The existence of those pseudo-magnetic monopoles in WSMs suggests the existence of a bulk topological invariant protecting the surface states. However, different from the case of TIs where the Fermi surface consists of closed curves in momentum space, WSMs host exotic, anomalous surface-state band structures containing Fermi arcs, which form open curves connecting Weyl nodes.

As said before, the local stability of the Weyl points is related to a topological invariant named Chern number (C or χ), well-known from the integer quantum Hall effect (IQHE). The Chern number is defined as

$$\chi = \frac{1}{2\pi} \int \int \boldsymbol{\Omega} \cdot d\boldsymbol{S}, \tag{2.28}$$

where $\boldsymbol{\Omega} = \nabla_k \times \boldsymbol{A}$ is the Berry curvature, which characterizes the wave function entanglement between the conduction and valence bands ([103] and therein), and $\boldsymbol{A} = -i\langle k, n|\nabla_k|k, n\rangle$ is the Berry connection. In this 3D case, we must choose a closed 2D manifold within the bulk of the FBZ to calculate χ. We refer to χ as the *chiral charge* of the Weyl node. It is possible to connect ideas with Gauss' law in classical electrodynamics as follows: In the same way as for the electric charge, the chiral charge is quantized, and the Chern number on any manifold only depends on the enclosed chiral charge.

As seen in Fig. 2.10, it is possible to split the three-dimensional band structure in a set of slices with a tuning parameter, k_x, and compute the respective Chern number (Figure 2.10 (d)). If the slices lie between the two Weyl nodes, the net Berry flux accumulated leads to a non-zero Chern number with chiral edge states. On the other hand, if the slices are outside the two Weyl nodes, the Chern number is zero and the surfaces are trivial 2D insulators. If we focus on the one-dimensional edges of the slices, as shown in the surface FBZ square in Fig. 2.10(d), it is possible to conclude that edges associated with a non-zero Chern number in the bulk host gapless chiral modes (Fig. 2.10 (e)), whereas those with zero Chern number are gapped (Fig. 2.10(c)). The one-dimensional edge states assemble into a sheet of surface states that cover the region between the two Weyl nodes, forming a topological Fermi arc surface state. Also, since the net charge of all Weyl nodes has to be zero, then the Weyl nodes are always present in pairs [104].

Unlike the WSMs for DSMs the Dirac nodes are not topologically protected since their net Chern number vanishes everywhere. However, some other symmetries can play the protecting role of Dirac nodes, such as TR, P, and crystal symmetries.

If we consider a WSM with anisotropic Fermi velocity now, the effect is to introduce an overall tilt of the Weyl cones. This new semi-metallic phase, which does not preserve Lorentz invariance, has been named *type-II* WSM [106]. Although type-I

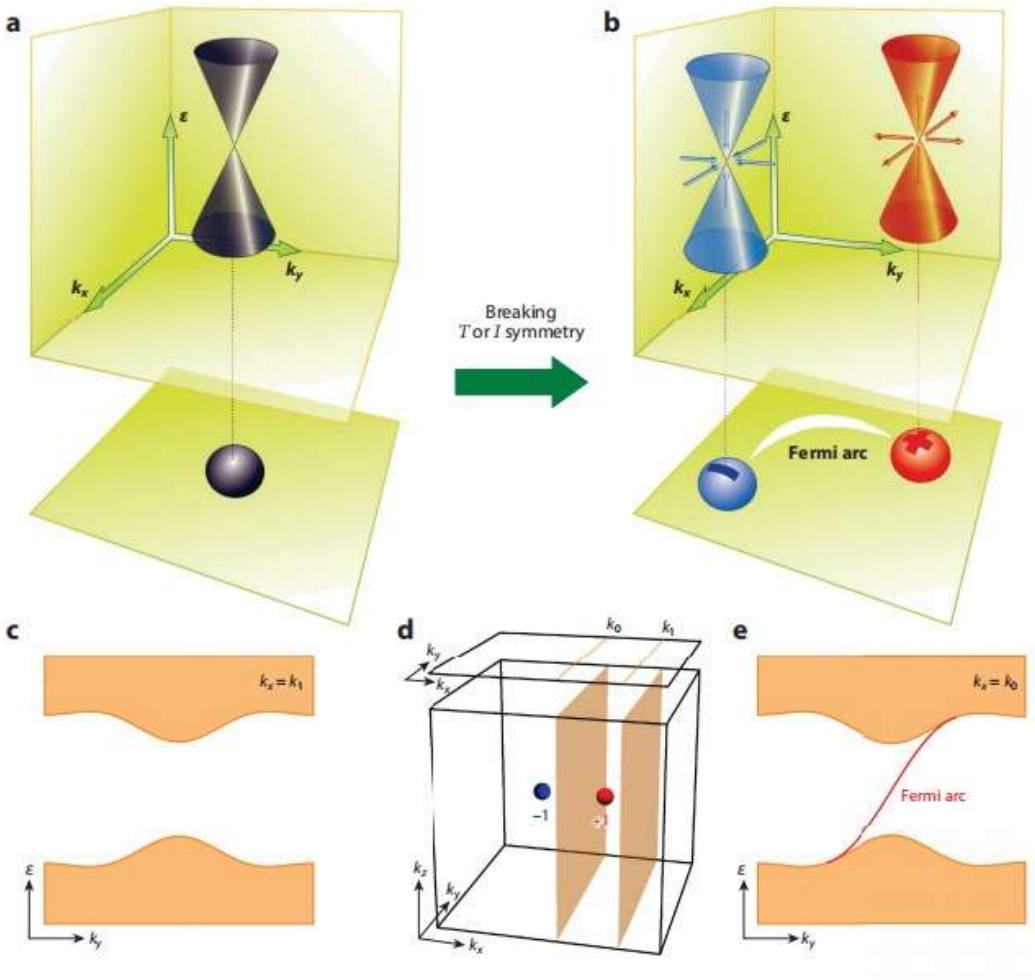

Figure 2.10: a) Energy-momentum dispersion of a Dirac semimetal conserving both time-reversal (TR) and inversion (P) symmetries, with two double-degenerate bands. b) When TR, P or both symmetries are broken, the Dirac cone splits into a pair ow Weyl nodes of opposite chiralities, each associated to a Chern number responsible of the fermi arcs states connectiong the projection of the Weyl nodes in the surface Brillouin zone. d) When a slice is placed between twom Weyl nodes the Chern number changes by ± 1, representing a topological phase transition with a Fermi arc arising from all the chiral edge states (d)), whereas when slices are placed out of the Weyl nodes the Chern number remains equal and no surface states arise (c)). Adapted from [105].

and type-II WSMs cannot be smoothly deformed into each other, they share electronic behavior. This is because type-II WSMs support surface Fermi arcs which terminate at the surface projections of their band node points (see Fig. 2.11).

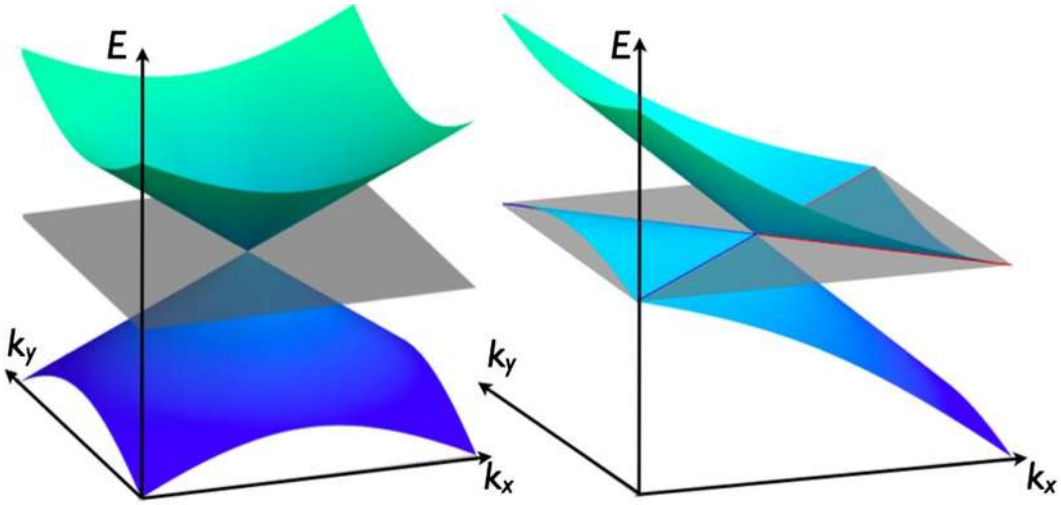

Figure 2.11: (Left) Type-I Weyl semimetal with point-like Fermi surface, and (right) type-II Weyl semimetals with tilted Weyl cones, whose Fermi surface is the intersection of isoenergy with both electron and hole pockets. Adapted from [107].

Experimentally, the first discovered material with WSM behavior was TaAs [105]. Some other compounds of the TaAs family, namely NbAs, TaP, and NbP have also been discovered recently by ARPES techniques [105].

WSMs give rise to new fascinating transport phenomena as a chiral anomaly in the presence of parallel electromagnetic fields, an anomalous Hall effect, or even novel particles obeying non-Abelian statistics with potential application in spintronics or topological qubits [108, 109, 110]. We discuss some of these novel effects in the Supplements.

Supplements

2.A Relativistic quantum mechanics

We follow the discussion given in Ref. [59]. As we previously discussed, the low-energy Hamiltonian which describes the electronic properties of Dirac materials can be approximated near the Dirac nodes as

$$\hat{H}_D = \hbar v_F \boldsymbol{\sigma} \cdot \mathbf{q}, \tag{2.29}$$

which has the form of a Dirac equation describing relativistic massless fermions. This Supplement is specially devoted to giving a brief introduction to Relativistic Quantum Mechanics (RQM).

We start with a historical review of the elaboration of RQM in the late 20ies of the last century. Then, we focus on the Dirac equation, particularly in the two-dimensional case (two space and one time dimensions), which is important in the case of graphene, deriving some of its properties. Finally, a brief introduction to chirality is presented[1].

2.A.1 Relativistic quantum mechanics

High energy systems are those in which the particles acquire very high velocities, close to c. So, it is required a relativistic wave equation to describe its quantum dynamics. The new wave equation is required to satisfy both, quantum mechanics and special relativity postulates. In particular, it has to satisfy:

1. The equation has to be invariant under Lorentz transformations.

2. Spatial and temporal coordinates have to be treated equally. From this assumption we immediately see that Schrödinger equation, whose temporal and spatial derivatives are of different order, cannot describe relativistic systems.

3. The Heisenberg uncertainty principle:

$$\Delta x \Delta p > \hbar \Rightarrow \Delta x > \frac{\hbar}{m_0 c}, \tag{2.30}$$

   tells us that a relativistic particle cannot be localized more accurately than $\approx \hbar/m_0 c$, otherwise pair creation takes place. Thus, the idea of a free particle only makes sense for particles that are not confined to volumes smaller than

[1] The discussion about RQM and the Klein-Gordon equation is followed from [111]. On the other hand, the discussion about the Dirac equation in (3+1) and (2+1) dimensions is based on [111, 112], with some historical notes followed from [113]. Finally, the chirality discussion is based on [112].

approximately the Compton wavelength $\lambda_c = \hbar/m_0 c$. Furthermore, the time is also uncertain since

$$\Delta t \sim \frac{\Delta x}{c} > \frac{\hbar}{m_0 c^2}. \tag{2.31}$$

Therefore, we recognize the necessity to reconsider the concept of probability density, $\rho(\mathbf{r}, t)$, which describes the probability of finding a particle at a definite place $\mathbf{r}$ at a fixed time t. This problem does not occur in the non-relativistic case, where $c \to \infty$, having arbitrarily small values of Δt.

4. At high energies, pair creation (particle-antiparticle pair) and annihilation process occur. In consequence, the particle conservation assumption is no longer valid.

2.A.2 The Klein-Gordon equation

The first efforts to obtain an equation satisfying these assumptions were made independently by Schrödinger, Klein and Gordon in 1926/27 [114, 115, 116]. They departed from the relativistic dispersion relation

$$p^2 = \frac{E^2}{c^2} - \mathbf{p}^2 = m_0^2 c^2, \tag{2.32}$$

with $p^\mu = \left(\frac{E}{c}, \mathbf{p}\right)$ is the four-momentum. Replacing this four-momentum by its respective four-momentum operator in Hilbert space:

$$\begin{aligned} \hat{p}^\mu &= i\hbar \left\{ \frac{\partial}{\partial(ct)}, -\frac{\partial}{\partial x}, -\frac{\partial}{\partial y}, -\frac{\partial}{\partial z} \right\} \\ &= i\hbar \left\{ \frac{\partial}{\partial(ct)}, -\nabla \right\} = \left\{ \hat{p}_0, \hat{\mathbf{p}} \right\}, \end{aligned} \tag{2.33}$$

we obtain the Klein-Gordon equation for free particles

$$\hat{p}^\mu \hat{p}_\mu \psi = m_0^2 c^2 \psi, \tag{2.34}$$

where m_0 is the rest mass of the particle and c the speed of light in vacuum. This equation can be brought to the form:

$$\left(\frac{1}{c^2}\frac{\partial^2}{\partial t^2} - \frac{\partial^2}{\partial x^2} - \frac{\partial^2}{\partial y^2} - \frac{\partial^2}{\partial z^2} + \frac{m_0^2 c^2}{\hbar^2} \right) \psi = \left(\Box + \frac{m_0^2 c^2}{\hbar^2} \right) \psi = 0, \tag{2.35}$$

where the d'Alambertian operator $\Box = \frac{1}{c^2}\frac{\partial^2}{\partial t^2} - \frac{\partial^2}{\partial x^2} - \frac{\partial^2}{\partial y^2} - \frac{\partial^2}{\partial z^2}$ is defined. It can be inferred immediately from Eq. (2.34) the Lorentz covariance of the Klein-Gordon

equation, as $\hat{p}^\mu \hat{p}_\mu$ is Lorentz invariant. In addition, Eq. (2.35) can be recognized as the classical wave equation including the mass term, whose solutions are

$$\psi = \exp\left[-\frac{\mathrm{i}}{\hbar}(\mathrm{p_0 x^0} - \mathbf{p}\cdot\mathbf{r})\right] = \exp\left[\frac{\mathrm{i}}{\hbar}(\mathbf{p}\cdot\mathbf{r} - Et)\right]. \tag{2.36}$$

Substituting this solution in Eq. (2.34) we recover the dispersion relation

$$\frac{E^2}{c^2} - \mathbf{p}^2 = m_0^2 c^2 \Rightarrow E = \pm\sqrt{m_0^2 c^4 + \mathbf{p}^2 c^2}. \tag{2.37}$$

Therefore, solutions exist for both positive and negative energies. This unexpected behavior of the spectrum represented a severe problem to the quantum theory at that time, as the ground state may not be correctly defined for an energy spectrum with no lower bound. In principle, a particle in a higher energy level would "fall" to one of lower energy by the emission of a photon with energy given by the difference in energy between the initial and final states, but without a lower bound, this process would occur infinitely. This "problem" represented an important advance in the field, when it was cleverly interpreted.

Another problem of the Klein-Gordon equation is related to its second order time derivative. To illustrate this point let us construct the four-current connected with Eq. (2.35). Multiplying Eq. (2.35) from the left by ψ^*

$$\psi^*\left[\Box + \left(\frac{m_0 c}{\hbar}\right)\right]\psi = 0. \tag{2.38}$$

Then, taken the complex conjugate of Eq. (2.35) and multiplying from the left by ψ

$$\psi\left[\Box + \left(\frac{m_0 c}{\hbar}\right)\right]\psi^* = 0. \tag{2.39}$$

Subtracting Eq. (2.38) - Eq. (2.39), we get

$$\psi^*\Box\psi - \psi\Box\psi^* = 0 \Rightarrow \partial_\mu\left(\psi^*\partial^\mu\psi - \psi\partial^\mu\psi^*\right) \equiv \partial_\mu j^\mu = 0, \tag{2.40}$$

where we have used the covariant and contravariant definitions of the four-gradient

$$\partial_\mu = \left(\frac{\partial}{\partial ct}, \frac{\partial}{\partial x}, \frac{\partial}{\partial y}, \frac{\partial}{\partial z}\right), \tag{2.41}$$

$$\partial^\mu = \left(\frac{\partial}{\partial ct}, -\frac{\partial}{\partial x}, -\frac{\partial}{\partial y}, -\frac{\partial}{\partial z}\right), \tag{2.42}$$

and where we defined the four-current

$$j_\mu \equiv (\rho, \mathbf{j}) = \frac{i\hbar}{2m_0}\left(\psi^*\partial_\mu\psi - \psi\partial_\mu\psi^*\right). \tag{2.43}$$

Explicitly, Eq. (2.40) has the form

$$\frac{\partial}{\partial t}\left[\frac{i\hbar}{2m_0c^2}\left(\psi^*\frac{\partial\psi}{\partial t}-\psi\frac{\partial\psi^*}{\partial t}\right)\right]+\nabla\cdot\left[-\frac{i\hbar}{2m_0}\left(\psi^*\nabla\psi-\psi\nabla\psi^*\right)\right]=0, \tag{2.44}$$

which has the form of a continuity equation

$$\frac{\partial}{\partial t}\rho+\nabla\cdot\mathbf{j}=0, \tag{2.45}$$

with the probability density ρ given by

$$\rho(\mathbf{r},t)=\frac{i\hbar}{2m_0c^2}\left(\psi^*\frac{\partial\psi}{\partial t}-\psi\frac{\partial\psi^*}{\partial t}\right). \tag{2.46}$$

Therefore, as the Klein-Gordon equation is of second order in the time derivative, at a given time t, both ψ and $\frac{\partial\psi}{\partial t}$ may have arbitrary values, so that, $\rho(\mathbf{r},t)$ may be either positive or negative, and thus cannot be interpreted as a probability density. This is the deeper reason to consider the Klein-Gordon equation to be physically senseless. Then, it was required to seek a relativistic wave equation of first order in time.

2.A.3 The Dirac equation

After the problems with the Klein-Gordon equation, in 1928 Dirac was looking forward to develop a wave equation of the Schrödinger form [117, 117]

$$i\hbar\frac{\partial\psi}{\partial t}=\hat{H}\psi, \tag{2.47}$$

with positive definite probability density. Dirac understood that, in order to satisfy the Lorentz invariance, it had to be constructed an equation which were linear in time derivatives, and at the same time linear in space derivatives. So, the desired equation has to be of the form

$$i\hbar\frac{\partial\Psi}{\partial t}=\left[\frac{\hbar c}{i}\left(\hat{\alpha}_1\frac{\partial}{\partial x^1}+\hat{\alpha}_2\frac{\partial}{\partial x^2}+\hat{\alpha}_3\frac{\partial}{\partial x^3}\right)+\hat{\beta}m_0c^2\right]\Psi\equiv\hat{H}_D\Psi, \tag{2.48}$$

where $\hat{H}_D$ can be expressed as

$$\hat{H}_D=\frac{\hbar c}{i}\hat{\alpha}\cdot\nabla+\hat{\beta}m_0c^2. \tag{2.49}$$

From equation (2.48), the next conditions have to be satisfied:

1. The objects $\hat{\beta}$, and $\hat{\alpha} = (\hat{\alpha}_1, \hat{\alpha}_2, \hat{\alpha}_3)$ are dimensionless, and, in order to satisfy spatial rotation invariance, they cannot be simple numbers. Actually, they have to be matrices, and therefore, $\hat{H}_D$ is a $n \times n$ matrix. Additionally, in order that $\hat{H}_D$ be hermitian, $\hat{\beta}$, and $\hat{\alpha}$ have to be hermitian as well .

2. Then, Ψ cannot be a simple scalar function, but has to be a column vector

$$\Psi = \begin{pmatrix} \psi_1 \\ \psi_2 \\ . \\ . \\ . \\ \psi_n \end{pmatrix}. \tag{2.50}$$

3. The probability density is positive definite

$$\rho(x) = \Psi^\dagger \Psi = (\psi_1^*, ..., \psi_n^*) \begin{pmatrix} \psi_1 \\ . \\ . \\ . \\ \psi_n \end{pmatrix} = \sum_i \psi_i^* \psi_i, \tag{2.51}$$

   and it is the temporal component of a conserved four-current $j^\mu = (\rho, \mathbf{j})$, such that the continuity equation is satisfied

$$\partial_\mu j^\mu = 0 \Rightarrow i\hbar \frac{\partial}{\partial t}(\Psi^\dagger \Psi) = \frac{\hbar c}{i} \nabla \cdot (\Psi^\dagger \alpha \Psi), \tag{2.52}$$

   with $\rho = \Psi^\dagger \Psi$ and $\mathbf{j} = \Psi^\dagger \alpha \Psi$.

In order to satisfy the relativistic dispersion relation given by Eq. (2.32), from the square of Eq. (2.48) expressed in components

$$-\hbar^2 \frac{\partial^2 \psi_\sigma}{\partial t^2} = -\hbar c^2 \frac{\alpha_i \alpha_j + \alpha_j \alpha_i}{2} \frac{\partial^2 \psi_\sigma}{\partial x^i \partial x^j} + \frac{\hbar m_0 c^3}{i} \frac{\alpha_i \beta + \beta \alpha_i}{2} \frac{\partial \psi_\sigma}{\partial x^i} + \beta^2 m_0^2 c^4 \psi_\sigma, \tag{2.53}$$

the next relations are required:

1. $\alpha_i \alpha_j + \alpha_j \alpha_i = \{\alpha_i, \alpha_j\} = 2\delta_{ij}$, where δ_{ij} is the Kronecker delta.

2. $\alpha_i \beta + \beta \alpha_i = \{\alpha_i, \beta\} = 0$.

3. $\alpha_i^2 = \beta^2 = \mathbf{I}$, where $\mathbf{I}$ represents the $n \times n$ identity matrix. So that, the eigenvalues of these matrices are always ± 1.

4. To accomplish the hermiticity of the Hamiltonian, the matrices α_i and β have to be hermitian, and also from condition (3), they have to be unitary

$$\alpha_i = \alpha_i^\dagger = \alpha_i^{-1} \quad \text{and} \quad \beta = \beta^\dagger = \beta^{-1} \ .$$

5. By using the trace property $\mathrm{tr}[AB] = \mathrm{tr}[BA]$ in condition (2):

$$\alpha_i\beta = -\beta\alpha_i \Rightarrow \mathrm{tr}[\beta\alpha_\mathrm{i}\beta] = \mathrm{tr}[\beta^2\alpha_\mathrm{i}] = \mathrm{tr}[\alpha_\mathrm{i}] = \mathrm{tr}[-\beta^2\alpha_\mathrm{i}] = -\mathrm{tr}[\alpha_\mathrm{i}]$$

$$\Rightarrow \mathrm{tr}[\alpha_\mathrm{i}] = 0 = \mathrm{tr}[\beta] \ .$$

Thus, they are null-trace matrices, and, as their eigenvalues are only ± 1, it is immediately seen that their dimension n must be pair.

Conditions (1), (2), and (3) define the so-called *Clifford* algebra.

In the $(3+1)$ dimensional case, the minimal dimension of the matrices α_i and β is 4. One may satisfy the Clifford algebra by choosing, *e.g.*, the so-called standard representation

$$\beta = \begin{pmatrix} \mathbf{I} & 0 \\ 0 & -\mathbf{I} \end{pmatrix} \quad \text{and} \quad \alpha_i = \begin{pmatrix} 0 & \sigma_i \\ \sigma_i & 0 \end{pmatrix}, \tag{2.54}$$

where the σ_i matrices are the well-known Pauli matrices

$$\sigma_1 = \begin{pmatrix} 0 & 1 \\ 1 & 0 \end{pmatrix}, \quad \sigma_2 = \begin{pmatrix} 0 & -i \\ i & 0 \end{pmatrix}, \quad \sigma_3 = \begin{pmatrix} 1 & 0 \\ 0 & -1 \end{pmatrix}. \tag{2.55}$$

As a consequence, the Dirac Hamiltonian has a matrix structure

$$H_D^{3D} = \begin{pmatrix} m_0c^2 & c\hat{\mathbf{p}}\cdot\boldsymbol{\sigma} \\ c\hat{\mathbf{p}}\cdot\boldsymbol{\sigma} & -m_0c^2 \end{pmatrix}, \tag{2.56}$$

and the quantum state must be represented by the *four-spinor* $\Psi = \begin{pmatrix} \psi_1 \\ \psi_2 \\ \psi_3 \\ \psi_4 \end{pmatrix}$. If we represent it as formed by two two-spinors $\Psi = \begin{pmatrix} \phi \\ \xi \end{pmatrix}$, with $\phi = \begin{pmatrix} \phi_1 \\ \phi_2 \end{pmatrix}$ and $\xi = \begin{pmatrix} \xi_1 \\ \xi_2 \end{pmatrix}$, considering a particle at rest, we have the Dirac equation

$$\begin{pmatrix} m_0c^2 & 0 \\ 0 & -m_0c^2 \end{pmatrix} \begin{pmatrix} \phi \\ \xi \end{pmatrix} = E \begin{pmatrix} \phi \\ \xi \end{pmatrix}. \tag{2.57}$$

This equation has four solutions: Two with positive energy $E = m_0c^2$ corresponding to the components of the two-spinor ϕ, and which are related to the particle components of the four-spinor Ψ; the other two solutions, which possess a negative energy

value $E = -m_0c^2$, correspond to the components of the two-spinor ξ, related to the antiparticle components of the four-spinor Ψ. This interpretation of the ξ components as antiparticles was proposed for the first time by Dirac in 1931 [118], after Oppenheimer and Tamm argued that electron-proton annihilation in atoms would not be consistent with the stability of ordinary matter [119], breaking down the idea that the ξ components were related to protons. The existence of antiparticles was confirmed in 1932 when Anderson discovered the positron [120].

Furthermore, the components ϕ_1, ϕ_2 and ξ_1, ξ_2 of the two-spinors ϕ and ξ, respectively, correspond to both different possible spin states of the particle [121, 113].

By introducing the notation of the Dirac matrices γ^μ

$$\gamma^0 = \beta \ , \quad \gamma^i = \beta\alpha^i \quad \text{and} \quad \{\gamma^\mu, \gamma^\nu\} = 2g^{\mu\nu}, \tag{2.58}$$

and the Feynman "slash" notation

$$\not{a} = a_\mu \gamma^\mu, \tag{2.59}$$

we get the usually found covariant form (in natural units $\hbar = c = 1$) of the Dirac equation[2]

$$(i\not{\partial} - m_0)\Psi = 0. \tag{2.60}$$

(2+1) dimensional Dirac equation

In the $(2+1)$ dimensional case, which is of interest in the case of graphene, the Clifford algebra is satisfied by the identification of the α_i and β matrices with the Pauli matrices

$$\alpha_1 = \sigma_1, \quad \alpha_2 = \sigma_2, \quad \beta = \sigma_3, \tag{2.61}$$

so, the $(2+1)$ Dirac equation for massless particles can be written as

$$H_D^{2D} = c\sigma \cdot \mathbf{p}, \tag{2.62}$$

which, by the identification of c with the Fermi velocity v_F, has the same form as the Hamiltonian describing graphene, obtained in Chapter 2.

If we consider the $(2+1)$ Dirac equation for $m \neq 0$, it can be rewritten in the form

$$H_D^{2D} = \epsilon \begin{pmatrix} \cos\beta & \sin\beta \ e^{-i\phi_{\mathbf{p}}} \\ \sin\beta \ e^{i\phi_{\mathbf{p}}} & -\cos\beta \end{pmatrix}, \tag{2.63}$$

[2]The K-G equation is obtained by multiplying Eq. (2.60) by $(i\not{\partial} + m_0)$.

where we have defined the quantities

$$\epsilon = \sqrt{m_0^2 + \mathbf{p}^2},\ \cos\beta = \frac{m_0}{\epsilon},\ \sin\beta = \frac{|\mathbf{p}|}{\epsilon},\ \phi_{\mathbf{p}} = \arctan\left(\frac{p_y}{p_x}\right), \tag{2.64}$$

where additionally, we have taken the values $\hbar = c = 1$. The matrix in the right side of Eq. (2.63) is a unitary matrix, whose eigenvalues are $\lambda = \pm 1$, corresponding to the positive and negative energy states found earlier $E^\lambda = \lambda E = \lambda\sqrt{m_0^2 + \mathbf{p}^2}$.

Chirality

In high-energy physics it is defined the *helicity* [121, 113] of a particle as the projection of its spin onto the direction of propagation in 3-spatial dimensions,

$$h_{\mathbf{p}} = \frac{\mathbf{p}\cdot\boldsymbol{\sigma}}{|\boldsymbol{p}|}, \tag{2.65}$$

where the "$\boldsymbol{\sigma}$" here is a 4×4 matrix with the $2D$ Pauli matrices in the diagonal. It is an hermitian and unitary operator with eigenvalues $\eta = \pm 1$:

$$h_{\mathbf{p}}\,|\eta = \pm 1\rangle = \pm\,|\eta = \pm 1\rangle\,. \tag{2.66}$$

In this case, σ describes the real physical spin of the particle. The helicity operator $h_{\mathbf{p}}$ commutes with the Dirac Hamiltonian, and it is therefore a good quantum number.

In the case of graphene, the Pauli matrices no longer describe the real spin, but the sublattice isospin. In this case the helicity operator is called *chirality* operator, and it just commutes with the Hamiltonian in absence of a particle mass m_0.

The massless $(2+1)$ Dirac Hamiltonian for graphene can be rewritten in terms of the chirality operator as

$$H_D^{2D} = |\mathbf{p}|h_{\mathbf{p}}\ , \qquad H_D^{2D,\xi} = \xi H_D^{2D} = \xi|\mathbf{p}|h_{\mathbf{p}}\ , \tag{2.67}$$

where ξ refers to the two-fold *valley pseudospin degeneracy* ($\xi = \pm$). Then, the band index λ, which describes the valence and the conduction bands, is entirely determined by the chirality and the valley pseudospin

$$\lambda = \xi\eta\ . \tag{2.68}$$

This expression can be graphically seen in Fig. 2.12, where the valence and conduction bands for each valley ($\mathbf{K}$ and $\mathbf{K}'$) are shown, and define the chirality of the particles in them.

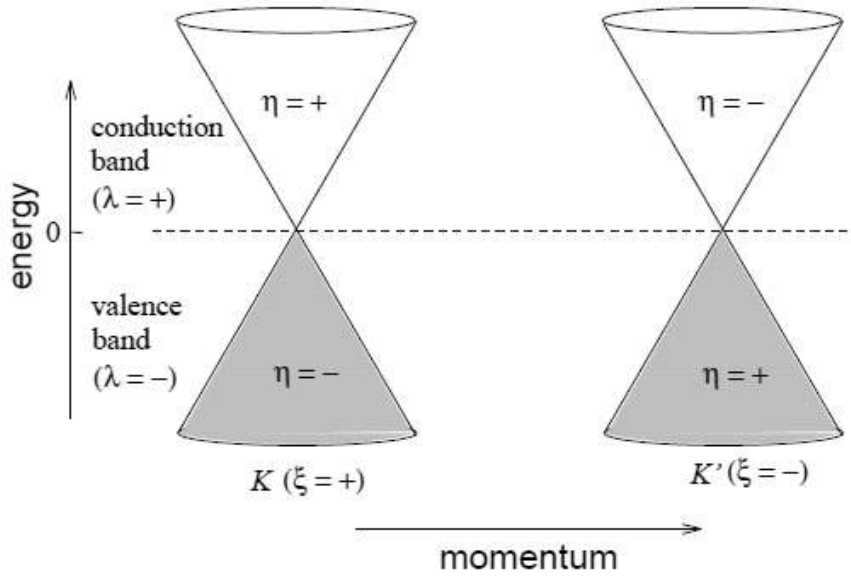

Figure 2.12: Relation between the band index λ, valley isospin ξ, and chirality η. Adapted from [112].

2.B Universal properties

As we have said before, there exist many common properties that Dirac materials share, independently of its diverse nature or dimensionality [55]. Some of them are related with collective many-body interactions of Dirac fermions, and others with the interaction of the material with external perturbations such as external electromagnetic fields or strains. In this Supplement we very economically review some of that universal properties, which are all produces by the unconventional linear spectrum of the fermions in Dirac materials

2.B.1 Many-body interactions

Many-body interactions, such as electron-electron or electron-phonon interactions, is a very complex issue in condensed matter physics, as it involves a macroscopic number of particles moving collectively. However, some many-body effects have been attributed to the peculiar low-energy spectrum in Dirac materials.

Electronic excitations

The main excitation present in metallic/semimetallic systems is the electron-hole excitation and its associated collective modes, as for example the quanta of plasma oscillations in an electron gas, that is, *plasmons*. Electron-hole pairs are excitations of the Fermi sea in which an electron with momentum $\boldsymbol{k}$ and energy E in excited to momentum $\boldsymbol{k}+\boldsymbol{q}$ and energy $E+\epsilon$, where $\epsilon \approx v_{\mathrm{F}}\boldsymbol{q}$. For conventional materials, the electron-hole excitations are always intra-band transitions since it is always possible to create the excitations for arbitrarily low energies (Fig. 2.13(a)). For this case it is also possible a plasmon excitation with $\epsilon\ \alpha\ \sqrt{q}$ [122]. For undopped Dirac materials, the Fermi level locates exactly at the Dirac point,. Therefore any excitation in inter-band (Fig. 2.13(b)) with plasmons all lying in the same band. When Dirac materials are dopped, intra-band electron-hole excitations are again permitted, as well as inter-band excitations for large-enough energies (Fig. 2.13(c)). In this case, the material behaves as a mixture of conventional and Dirac material. Also, in this case a plasmon excitation is again sustainable at long wavelengths.

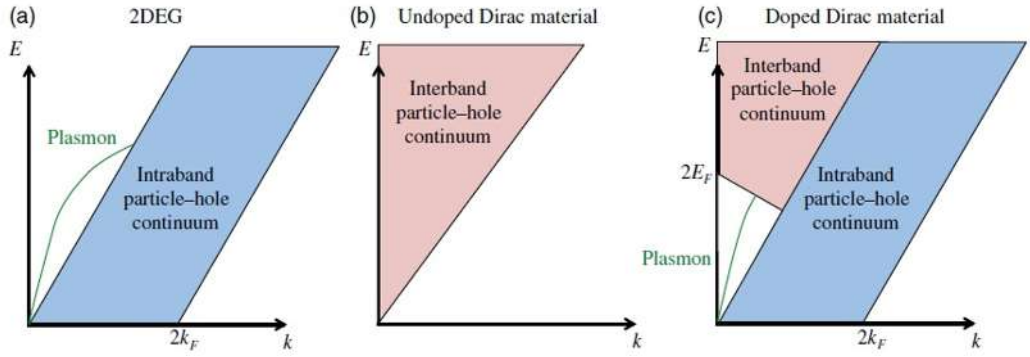

Figure 2.13: Energy-momentum plot for the electron-hole excitations in (a) a two-dimensional electron gas, (b) an undopped Dirac material (Fermi level at the Dirac point) and (c) dopped Dirac material (with a band gap). Adapted from [55].

Electronic screening

It results that in Dirac materials, in particular in graphene, there exists a lack of electronic screening [55]. As a consequence, long-distance Coulomb interactions remain unchanged in these systems [123, 124]. This can be formulated as if there is no charge renormalization in Dirac materials.

Velocity renormalization

In counterpart, as a direct consequence of the lack of screening in Dirac materials, since Lorentz invariance is broken by the long-range instantaneous Coulomb repulsion, then the Fermi velocity should be renormalized, of course, without exceeding the speed of light. Some evidence has been found about velocity renormalization in Dirac materials [125, 126].

Excitonic state

There exists the possibility of a spontaneous generation of mass in Dirac materials as a result of the long-range Coulomb potential. That is, an excitonic state. Calculations on this phenomenon have been performed in recent years [127, 128, 129].

Superconductivity

Dirac materials present low or vanishing (for the undopped case) density of states (DOS) at the Fermi level. Therefore, these materials are propense to form an intrinsic superconducting state, as studied in Refs. [130, 131, 132, 133]. Aditionally, Cooper pairs and superconductivity can be induced in Dirac materials by proximity to an external superconductor. A clear example of that effect is the Josephson junction in graphene [134, 135, 136, 137].

2.B.2 Thermodynamic properties

The Dirac Hamiltonian produces a DOS, $N_0(E)$, around the Dirac points with the form

$$N_0 \sim E^{d-1}. \tag{2.69}$$

As a consequence, the thermodynamic response functions can be described in terms of a universal set of exponents describing their power-law dependence in temperature, T [55]. One example is the specific heat in Dirac materials which behaves as $C(T)_{T\to 0} \sim T^d$, very different from the behaviour in conventional materials where $C(T)_{T\to 0} \sim T$.

2.B.3 Magnetic field dependence

The response of Dirac materials to external magnetic fields results in novel phenomena in each case. Next we review the main example of these effects, that is, the generation of *Landau levels*. Some other novel effects in Weyl SMs are presented in the Suppl. 2.C.

Landau levels

The interaction of a graphene sheet with an external magnetic field perpendicular the the graphene plane results in the well-known quantization of the energy in term of the intensity of the magnetic field. Explicitly

$$E_n(B) = \hbar v_{\mathrm{F}} \sqrt{\frac{2eB|n|}{\hbar}}, \tag{2.70}$$

that is, energy levels go as the square-root of the principal quantum number, in contrast with the linear relation in Schrödinger fermions. These levels are known as Landau levels (Lls). Experimental realization of this effect have been done in 2D [138, 30, 139, 140, 141], as well as in 3D topological insulators [142, 143]. Another distinctive feature in Lls is the fact that at zero-energy, there exists a level composed by both electrons and holes in equal amounts. The existence of this zero-energy level gives rise to a quantum Hall effect with Hall conductance $\sigma_{xy} \sim n + 1/2$ [138, 30].

2.B.4 Suppression of backscattering

The effect of backscattering has been discussed in graphene [144, 19], d-wave superconductors [145] and TIs [146], consisting in a very universal phenomenon in Dirac materials. The origin of this effect comes from destructive interference between wave states produced by backscattering potentials which are diagonal in pseudo-spin space [144]. From this effect emerges the famous Klein tunnelling in Dirac materials [19].

2.C Novel transport properties in WSMs

2.C.1 Chiral anomaly

Let us consider a 3D WSM in the presence of an external magnetic field. The zero-energy level, $\varepsilon = \chi \hbar v_{\mathrm{F}} \boldsymbol{k} \cdot \boldsymbol{B}$ is a chiral mode whose dispersing direction is set by the chirality of the Weyl node, χ. If an external electric field is also applied to the sample in the same direction as the magnetic field, all the states will move according to $\hbar \boldsymbol{k} = -e\boldsymbol{E}$, that is, in the electric field direction. This implies that, for the zero-energy state, electrons are either appearing or disappearing depending on the chirality of the Weyl node. Therefore, charge is not conserved around each Weyl node, resulting in a modified chiral charge continuity equation

$$\frac{\partial n}{\partial t} + \nabla \cdot \boldsymbol{J} = \pm \frac{e^2}{4\pi^2 \hbar^2} \boldsymbol{E} \cdot \boldsymbol{B}. \tag{2.71}$$

This non-conservation of charged particles in each single Weyl point is known as the *chiral anomaly*, or the Adler-Bell-Jackiw anomaly [147, 148].

Some consequences of the chiral anomaly are the valley polarization between Weyl nodes with opposite chirality given by

$$\frac{\partial(n_+ + n_-)}{\partial t} = \frac{e^2}{4\pi^2\hbar^2}\boldsymbol{E}\cdot\boldsymbol{B}. \tag{2.72}$$

Another important effects consequence of the chiral anomaly anomaly are the large longitudinal conductivity along the applied magnetic field and negative magnetoresistance, that is the *chiral magnetic effect* (studied next) [149, 150, 151], as well as the anomalous quantum Hall effect (AQHE) in which the Hall conductance

$$G_H = \frac{e^2}{2\pi\hbar}\sum_i \boldsymbol{\chi}_i \boldsymbol{k}_i, \tag{2.73}$$

is directly proportional to the momentum space separation between the two Weyl points [150].

2.C.2 Chiral Magnetic effect and planar Hall effect

Important effects given as a result of the interaction of Weyl fermions with external electromagnetic fields are the chiral magnetic effect (CME) [152] and the planar Hall effect (PHE) [153]. The CME consists in the generation of an electric current, along the direction of an applied external magnetic field, induced by chirality imbalance in the material. It is a macroscopic phenomenon induced by the chiral anomaly, therefore, it does not require a spontaneous symmetry breaking. An important feature about the chiral current in CME is that it is non-dissipative, that because the current is topologically protected [55]. In Fig. 2.14 are shown two different approaches to analyse the CME: the firt (left), is that a topological charge of the background gauge field generates a spatially non-uniform chiral imbalance around the object. The secon case (right), is based in the idea of a chiral chemical potential, μ_5, which generates a spatially uniform chiral imbalance in matter. In both cases a uniform electric current is induced by the external magnetic field [154].

On the other hand, the PHE also implies the application of an external electric field forming an angle, θ, between both field directions. The PHE consists in the generation of a Hall current living at the plane generated by the electromagnetic external fields (Fig. 2.15). As well as the CME, the PHE is thought to have its origins in the chiral anomaly [26].

2.C.3 Axion electrodynamics

Transport effects such as CME and AQHE can be represented compactly with the definition of a new class of electrodynamics known as *axion* electrodynamics. The

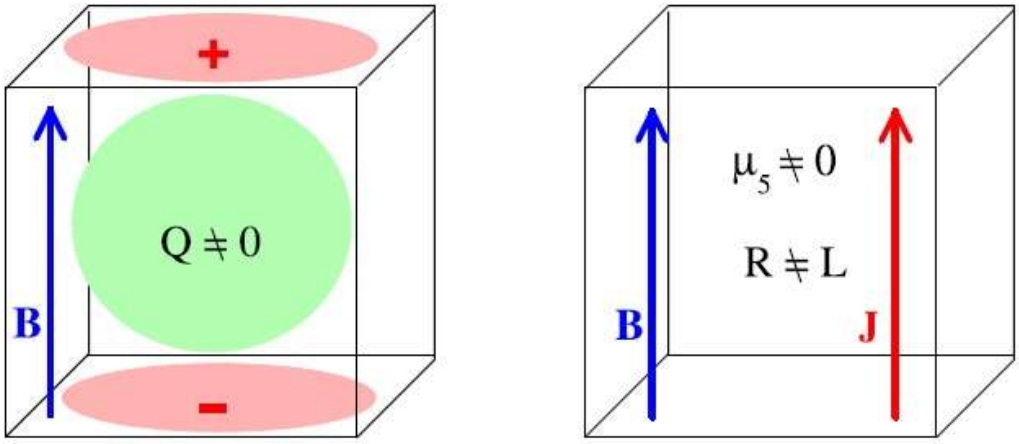

Figure 2.14: Two different approaches to understand the chiral magnetic effect: (left) through the existence of a topological charge of the background gauge field generating a spatially non-uniform chiral imbalance around it. (right) A non-vanishing chemical potential generating spatially uniform chiral imbalance in matter. Figure adapted from [154].

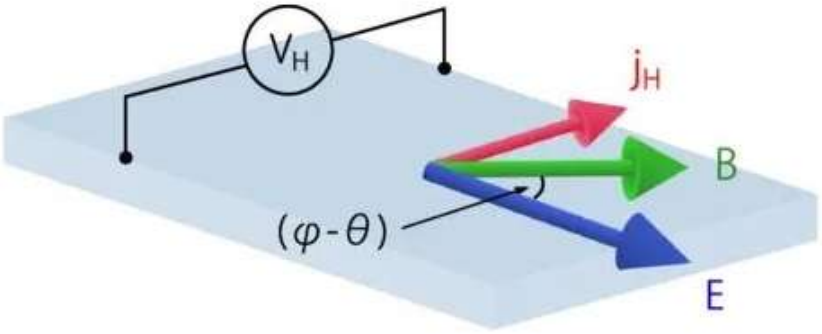

Figure 2.15: Sketch of the planar Hall effect in which a Hall current appears in the same plane generated by the external electric and magnetic fields. Adapted from [155].

changes to classical electrodynamics enters as the denoted axion term $\sim \varepsilon^{\mu\nu\rho\lambda}F_{\mu\nu}F_{\rho\lambda}$ in the electrodynamic Lagrangian [107]. The action produced by this term is

$$S_\theta = \frac{1}{2\pi}\frac{e^2}{h}\int dtd\boldsymbol{r}\theta(\boldsymbol{r},t)\boldsymbol{E}\cdot\boldsymbol{B}, \tag{2.74}$$

where $\theta(\boldsymbol{r}, t) = 2(\boldsymbol{k}_0 \cdot \boldsymbol{r} - b_0 t)$. Here, $\boldsymbol{k}_0$ is the position of the Weyl nodes and $2b_0$ is the chemical potential shift between Weyl nodes. This term leads to macroscopic observable effects in the bulk material. The corresponding charge and current densities are

$$\rho = \frac{1}{2\pi}\frac{e^2}{h} 2\boldsymbol{k}_0 \cdot \boldsymbol{B}, \tag{2.75}$$

$$\boldsymbol{J} = \frac{1}{2\pi}\frac{e^2}{h} \left(2\boldsymbol{k}_0 \times \boldsymbol{E} - 2b_0 \boldsymbol{B}\right). \tag{2.76}$$

Equation (2.75) and the first term in Eq. (2.76) represent the AQHE, whereas the second term in Eq. (2.76) refers to the CME [107].

Chapter 3

SSH Model with Periodical Impurities

We study the SSH model, perhaps the simplest realization of a topological insulator, in the presence of an embedded impurity superlattice. We consider the impact of the said impurity by changing the hopping amplitudes between them and their nearest neighbors in the topological boundaries and the edge state localization in the chain of atoms. Within a tight-binding approach and through a topolectrical circuit simulation, we consider three different impurity-hopping amplitudes. We found a relaxation of the condition between hopping parameters for the topologically trivial and non-trivial phase boundary and a more profound edge state localization given by the impurity position within the supercell. We base our discussion in our article shown in Ref. [156].

3.1 Introduction

The emergence of topological matter has challenged the point of view of the classification of quantum materials in terms of their symmetry properties as described by unitary transformations and opened the possibility of a wider classification. In that direction, number of studies have been carried out to understand the mechanisms responsible for topological properties [157, 158, 159, 75, 160, 161, 162]. Time-reversal, particle-hole, and chiral symmetries, namely, unitary or antiunitary transformations that commute or anticommute with the Hamiltonian, are the building blocks of the so-called periodic table of topological insulators [163]. The *Su-Schrieffer-Heeger* model (SSH) [164, 165] is one of the simplest models which represents a topological insulator (see, for instance, Refs. [166, 167, 168, 160, 17, 169, 170, 171] and references therein). It describes the behavior of spinless electrons hopping through a one-dimensional lattice build up by two interspersed sublattices of atoms with alter-

nating nearest neighbors (NNs) *hopping* amplitudes. As first introduced, this model is useful for studying one-dimensional molecules such as polyacetylene $(CH)_x$. Its topological features, nevertheless, have boosted the interest in studying it and its extensions in a variety of situations, such as modulations of the hoppings and on-site energies (driven SSH model [172, 173, 174]), long-range interactions [175, 176, 110], two coupled SSH chains [177, 178, 179], dimensional extended models [180, 181, 182, 183], and other modifications [184, 185]. Depending upon the relative strength of the hopping parameters, the model exhibits a topologically trivial or nontrivial phase, which is distinguished by the emergence of a zero mode in the spectrum. The topologically invariant quantity turns out to be the Zak phase, which is either zero or one in the trivial and nontrivial phases, respectively [186]. These features make the SSH a favorite model to predict a nontrivial topological structure of some systems from the symmetries of the underlying Hamiltonian and the corresponding equations of motion.

The topological features of the SSH model have also been found in mechanical [187], photonic [188, 189], acoustic [190, 172] and other systems [191, 192, 193, 194, 195, 196]. The basic idea is that these *metamaterials* can be described by a two-band Hamiltonian, which yields similar equations of motion in the tight-binding regime as the model in question. In this regard, in the emergent field of topoelectric circuits [197, 198, 199, 200, 201, 202] one can map the current flow in electric circuits with a network of passive elements like capacitors and inductors in similar form to a tight-binding Hamiltonian where capacitances C and inductances L serve to define the hopping parameters. Hence, crystal systems like the SSH model, graphene and others with remarkable properties have found realization within these topoelectric circuits [203, 200, 204, 205]. For the case of the SSH model, an alternating network of capacitors and inductors play the role of a unit cell in a crystal whereas products of capacitances and inductances define the hopping parameters. The impedance of the system as generated by a resistor probe and a sinusoidal signal with varying frequency can be used to measure the response of the system. In the topological phase, such an impedance is found to diverge at a certain frequency in the topological phase of the system. This resonant regime can be expressed entirely in terms of the hopping parameters of the crystal. Moreover, localization of states can be visualized in terms of edge states formation in the topologically non-trivial phase. This opens the possibility of studying interesting crystallographic properties of crystals in terms of a network of LC circuits [197, 198, 199, 200, 201, 202, 203, 204, 205].

Of special interest is the role of impurities in the system from both the crystallographic and the electronic point of view. In this chapter, we explore the role of an impurity into the system in different setups by defining the N, i-super-SSH model. First, we consider an impurity in a super-cell that interacts with the network and observe its impact on the position of the resonance in the impedance. Then, we study the impact of its position within the sites of the super-cell. We explore the phase

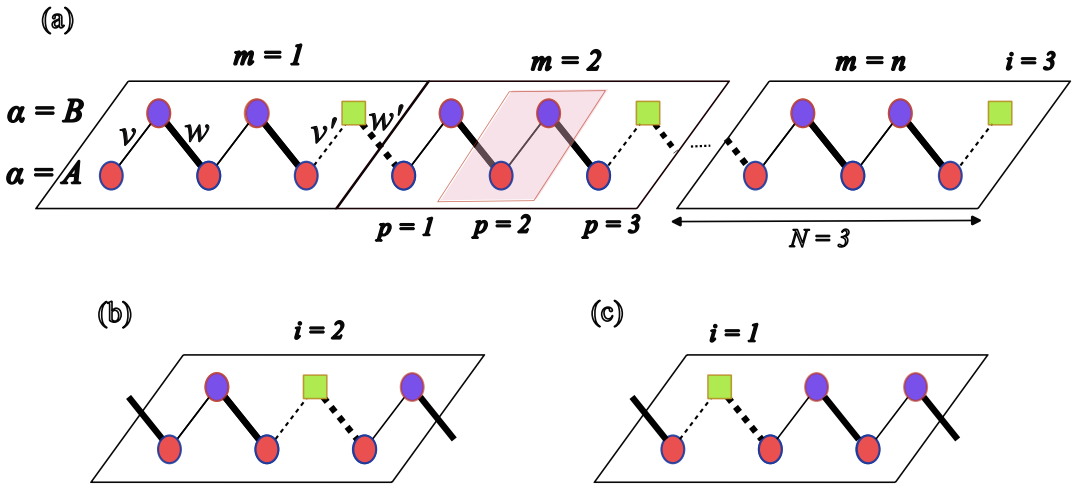

Figure 3.1: (a) Scheme of the N, i-super-SSH model for $N = 3$, $i = 3$. The shaded area denotes the SSH-unit cell, the supercell number is given by the parameter m, the supercell position by p, the species parameter is α and the impurity position is denoted by i. (b) and (c): Supercells of the case $N = 3$, $i = 2$(b) and $i = 1$(c), respectively. In all cases the green rectangles indicate the impurity atoms, the solid thin and thick lines correspond to the hopping parameters v and w, respectively, while the dashed thin and thick lines denote the v' and w' impurity hopping parameters, respectively. Figure reproduced from Ref. [156].

diagram in the parameter space of the hoppings of the chain and the emergence of edge states in the topological phase of the system. We analyze the dynamics both from the tight-binding perspective and then from an electric circuit simulation. The rest of this chapter is organized as follows. In the next section, we present the model under consideration. In section 3.4, we analyze the system in the Tight-Binding (TB) approach through the Python package "Pythtb" (Python Tight-Binding) [206]. In Section 3.5, we perform a numerical simulation of a topoelectrical circuit equivalent to our model. We conclude in Section 3.6 and present some details of the framework of topological circuits in a Supplement.

3.3 SSH model with embedded impurity superlattices

Let us begin our discussion by considering a one-dimensional chain of alternating atoms of species A and B, from which we define the species parameter $\alpha = A, B$, and hopping parameters v and w for the $A - B$ and $B - A$ links, as in the standard presentation of the SSH model, in which a unit cell consists of a pair of atoms A and B (see shaded area in Fig. 3.1(a)). Let us also consider a supercell constructed by

concatenating N SSH-unit cells. Such supercell has length N and we label the sites within the supercell as $p = 1, 2, ..., N$. Notice that each site consists of one SSH-unit cell in which one atom of species B is replaced by an impurity consisting of an atom of a third species C located in $p = i$, as shown in Fig. 3.1(a) for the case $N = 3$, $i = 3$. The system can then be described by four principal numbers: $m = 1, 2, 3, ..., n, ...$ denoting the number of supercells in the array, N denoting its length, p representing the label of the site position within the supercell, α denoting the atomic species, and an additional label i indicating the position of the impurity within the supercell. We dub this arrangement the (N, i)-*super-SSH model*. Figure 3.1(a) shows cases of the $(3, 3)$-super-SSH model, while Figs. 3.1(b) and (c) show the supercells of the $(3, 2)$- and $(3, 1)$-super-SSH model, respectively.

The effect of the impurities is based on the change of the hopping amplitudes between sites $A - C$ and $C - A$ to the new hoppings v' and w', respectively. Under this assumption, the system can still be thought as periodic, but now with a new unit supercell. In the general case, the quantities v' and w' can be considered as independent parameters or even functions of v and w. Moreover, for the purposes of this study, we explore electronic and topological properties of the system considering them as scalar parameters $v' = v + \delta v$ and $w' = w + \delta w$, under different assumptions for three different cases. We consider the periodic and the finite cases varying the supercell length N and the impurity position i within the supercell. As a first approach, below we consider a TB description of the system.

3.4 Tight-Binding Calculations

In this Section, we compute the electronic and topological properties of our system from a TB perspective. We write the TB Hamiltonian as

$$H_{super} = H^N_{SSH} + V_{N,i}, \tag{3.1}$$

where we define the extended SSH Hamiltonian as

$$\begin{aligned} H^N_{SSH} = \sum_{p=1}^{N-1} &\left(v|m,p,B\rangle\langle m,p,A| + w|m,p+1,A\rangle\langle m,p,B|\right) \\ &+ v|m,N,B\rangle\langle m,N,A| + w|m,1,A\rangle\langle m,N,B|, \end{aligned} \tag{3.2}$$

and the impurity potential

$$V_{N,i} = \begin{cases} \delta v|m,p,B \to C\rangle\langle m,p,A| \\ +\delta w|m,p+1,A\rangle\langle m,p,B \to C|, \text{ for } i = 1,2,...,N-1, \\ \\ \delta v|m,p,B \to C\rangle\langle m,p,A| \\ +\delta w|m+1,1,A\rangle\langle m,p,B \to C|, \text{ for } i = N. \end{cases} \tag{3.3}$$

It is important to note that in Eq. (3.3), the notation $B \to C$ means the replacement of an atom B by an impurity atom C. The exact algebraic diagonalization of the Hamiltonian in Eq. (3.1) gives as result tremendously intricate expressions for the energy-momentum dispersion, which results very difficult to manipulate. For this reason, we employ the Pythtb package [206] in order to get the eigenvalues and eigenvectors of the problem numerically. We consider three different configurations of the impurity-hopping amplitudes: In Case I, we consider $w = 1.0$ fixed and $v' = w'$, namely, equal impurity hopping to both nearest neighbours, rendering v and v' as the free parameters which we vary. In Case II, we explore the well-known topologically non-trivial phase of the SSH model with $w = 1.0$ and $v = 0.5$, and vice versa, namely, the topologically trivial phase [160, 161, 162]. We retain these values fixed, while varying the free parameters v' and w'. Finally, in Case III, we consider $w = w' = 1.0$ for which the impurity does not affect the $A - C$ hopping amplitude. This permits the variation of the free parameters (v, v').

For these three cases, we first explore the topological phase of the infinite periodic system imposing periodic boundary conditions with the hopping parameters as defined in each case. In order to do so, we first divide the First Brillouin Zone (FBZ) of the system into a discrete grid of M equally spaced intervals. In each point of the grid, we consider its corresponding wave vector $|u_k\rangle$, and we calculate the *Berry (Zak) Phase [186]* which represents the geometrical phase of the system through a closed loop as

$$\gamma_n(C) = -\mathrm{Im} \sum_{k=0}^{M} \langle u_k | \partial_k u_k \rangle, \tag{3.4}$$

where the sum travels a closed path in reciprocal space, *i.e.*, $|u_0\rangle = |u_M\rangle$. The $\mathbb{Z}_2$ underlying topological structure of the model allows to distinguish the topologically trivial ($\gamma_n(C) = 0$) and non-trivial ($\gamma_n(C) = \pi$) phases of the system throughout the space of free parameters in each case.

We also explore the spatial wave function localization of the topological zero mode state for a chain of finite length, namely, the edge states of the system, considering different sizes of the chain n, supercell length N, and impurity location within the supercell, i. For this purpose, we compute $|\psi_0(i)|^2$ and observe its distribution along the location i.

3.4.1 Case A

In this case, we fix the parameter $w = 1.0$ and force the condition $v' = w'$, thus the parameters v and v' define the parameter space. As can be observed in Fig. 3.2, from the behavior of the Berry phase we notice that the trivial or non-trivial topological phase structure of the system is not modified from the original SSH case [160, 161, 162], in which the topological non-trivial phase is achieved so long as $v < w$. We

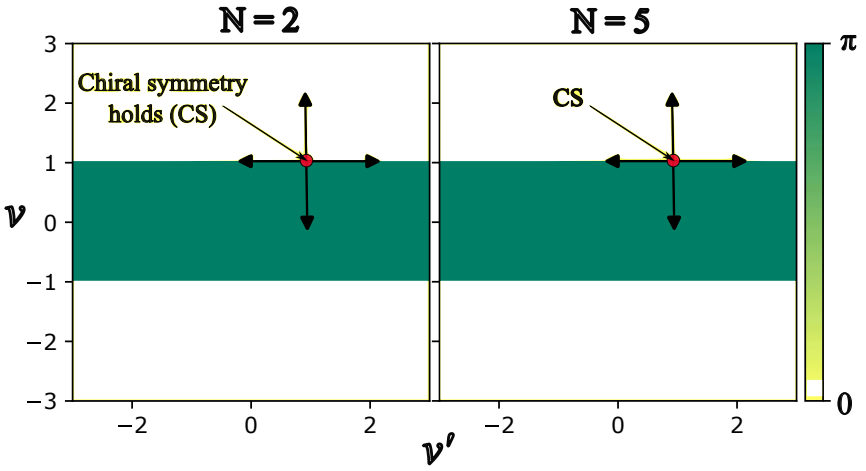

Figure 3.2: Berry phase in the space of free parameters of the periodic N, i-super-SSH model for Case I with $w = 1.0$, $v' = w'$ and for different values of N. Figure reproduced from Ref. [156].

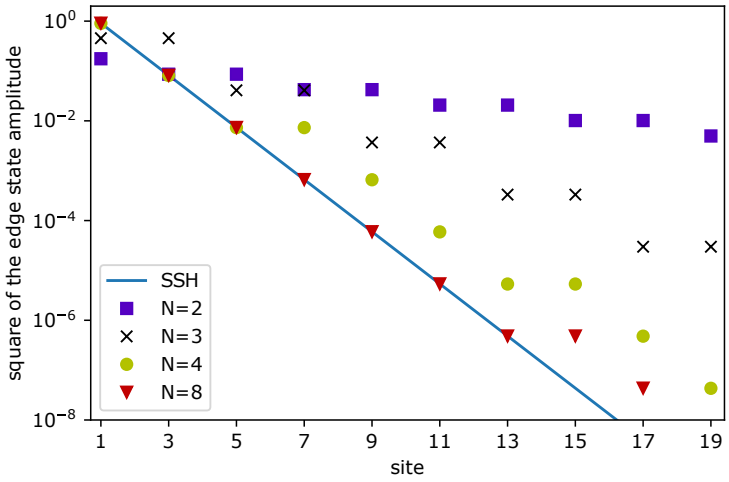

Figure 3.3: Edge state localization of a finite chain of the N, i-super-SSH model for the case $v = 0.3$, $w = 1.0$, $v' = w' = 0.5$ for different N values with the impurity in the position $i = N - 1$. Figure reproduced from Ref. [156].

can see that this condition is maintained independently of the supercell length, N. Note also that in the periodic case, the position of the impurity within the supercell is irrelevant.

Focusing now on the localization of the zero mode edge state, we notice that the

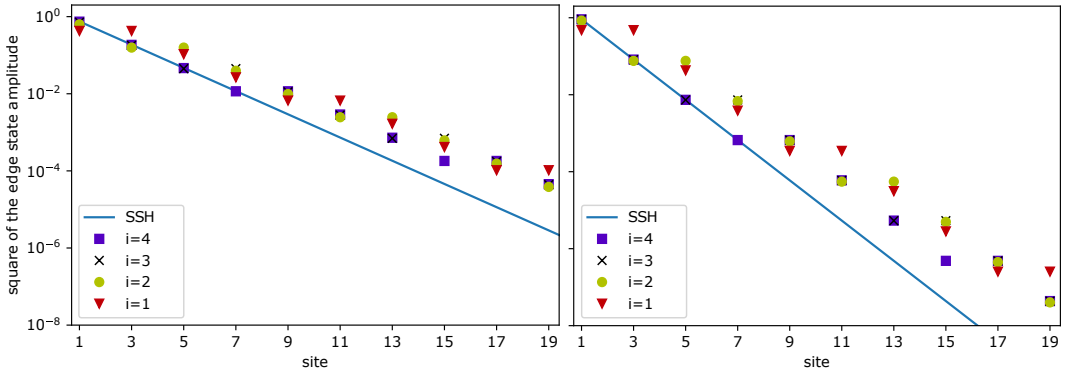

Figure 3.4: Edge state localization of the N, i-super-SSH model for the case $w = 1.0$ and (left) $v = 0.3$, $v' = w' = 0.5$ and (right) $v = 0.5$, $v' = w' = 0.3$, varying the position of the impurity, i, for $N = 4$. Figure reproduced from Ref. [156].

length of a finite chain composed by the concatenation of n supercells is unimportant for sufficiently long chains with $n \geq 10$. Graphics for these long chains where suppressed for space considerations in Fig 3.3. For the analysis, we work with $n = 12$. On the other hand, as can be seen in the same Figure, the supercell length N affects the edge state localization in a way that, as N increases, such state resembles more and more the zero mode of the original model already in the case of $N = 8$. This is completely expected since the impurity effects *dilute* with larger N, that is, the impurity density reduces for larger supercells. From this observations, we fix $n = 12$ and $N = 4$ in what follows, namely, we consider chains with 48 sites.

Now, from Fig. 3.4, we observe that the edge state localization is weakened compared to the original SSH model, so that as long as the condition $v < w$ is fulfilled; the parameter v' is not relevant in this case. On the contrary, the position of the impurity in the supercell is relevant, making the localization stronger for more to the right positions and weaker for more to the left positions. So that, the impurity in this case is promoting edge localization the closer it is to the right edge.

3.4.2 Case B

In this case, we have the two benchmark SSH scenarios: ($w = 1.0$; $v = 0.5$) which corresponds to a non-trivial topological phase in the SSH model and ($w = 0.5$; $v = 1.0$) for a trivial topological phase. The free-parameters are v' and w'.

As can be observed in Fig. 3.5, for the first scenario, it is possible to have both non-trivial and trivial topological phases depending on the values of v' and w'. These phases are separated by a linear boundary in parameter space. This is a counter-intuitive behavior as compared to the original SSH model. Note that for $N = 2$, there are many configurations in which it is possible to switch from the non-trivial

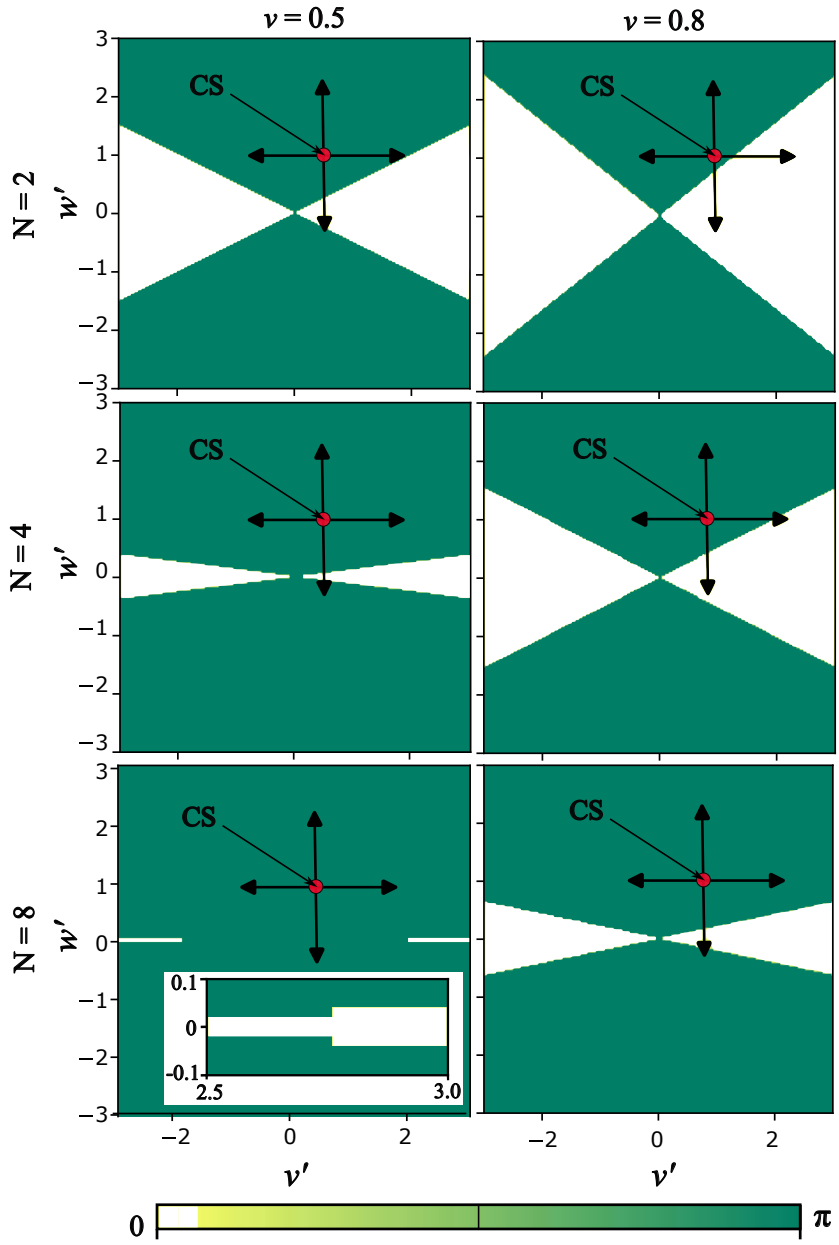

Figure 3.5: Berry phase in the space of free parameters (v', w') of the N, i-super-SSH model for the case $v < w$ ($v = 0.5, 0.8$ and $w = 1.0$ were taken) fixed for different N values. Figure reproduced from Ref. [156].

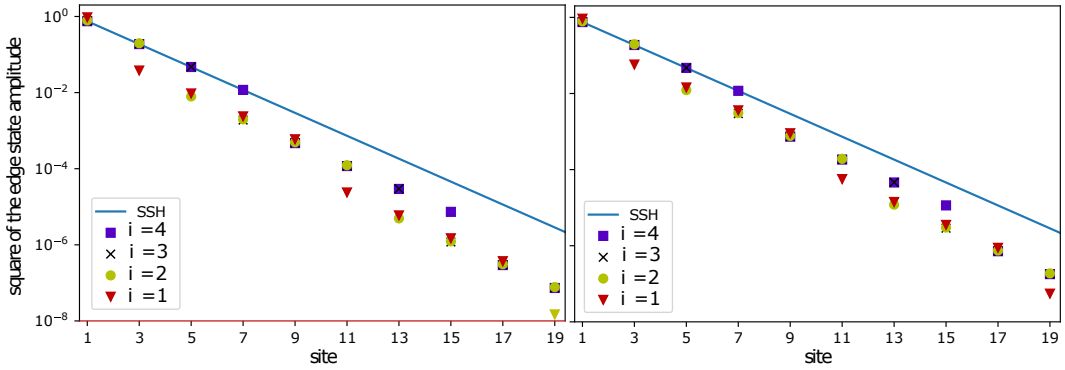

Figure 3.6: Edge state localization of the N, i-super-SSH model for the case $v < w$ ($v = 0.5$ and $w = 1.0$ were taken) fixed varying the free parameters v',w' and the position of the impurity for the case $N = 4$. (Top) $v' = 0.4$, $w' = 2.0$; (Bottom) $v' = 0.2$, $w' = 0.8$. Figure reproduced from Ref. [156].

to the trivial phase, and as the supercell length increases, the possibilities of swapping are reduced. For example, for $N = 8$, very large v' and very small v' hoppings are needed to flip between phases. Additionally, in Fig. 3.6 we can observe the possibility

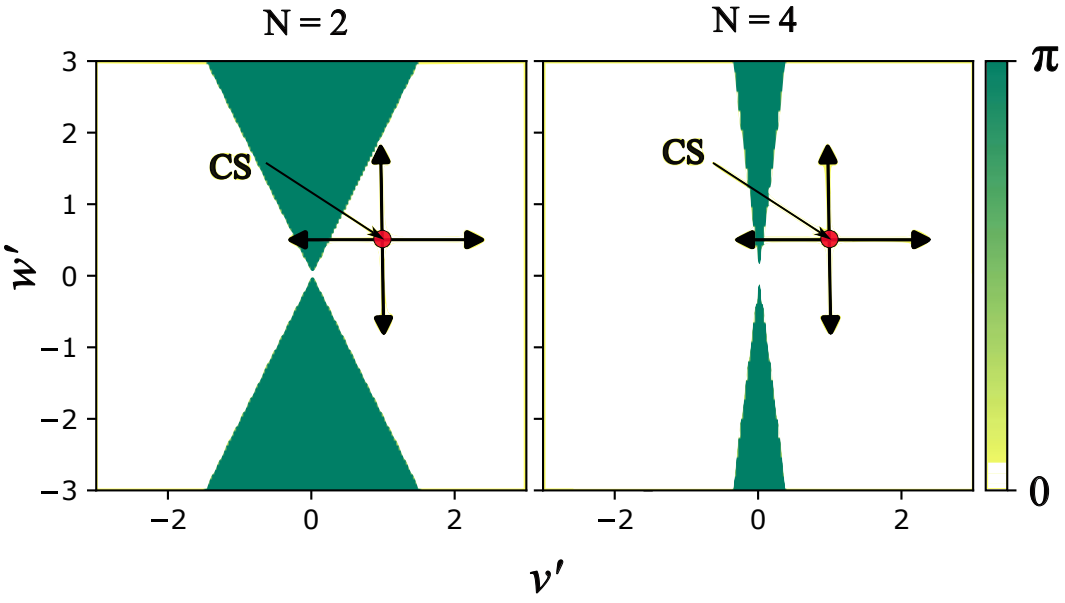

Figure 3.7: Berry phase in the space of free parameters of the N, i-super-SSH model for the case $v > w$ ($v = 1.0$ and $w = 0.5$ were taken) fixed for different N values. Figure reproduced from Ref. [156].

of reaching a more pronounced edge state localization as compared to the original SSH zero mode with the appropriate tuning of the parameters v' and w'. For example in case of Fig. 3.6 (top) it is accomplished with large values of w', whereas in the case of Fig. 3.6 (bottom) small values of v' are the responsible of this unexpected behavior. Different from Case I, here the edge localization is reinforced as the impurity locates more toward the left in the supercell, since, for example, for the impurity position $i = 1$, we obtain the largest localization.

A similar discussion follows in the scenario $w = 0.5$; $v = 1.0$, as observed in Fig. 3.7. It is well-known that for these values, the original SSH model exhibits a topologically trivial character. Surprisingly, in our model we see that it is possible to tune the system to a non-trivial topological phase by an appropriate choice of the impurity hopping. Thus, the possibility of switching to the non-trivial phase reduces as N becomes larger and the impurity dilutes. Notice also that just as in

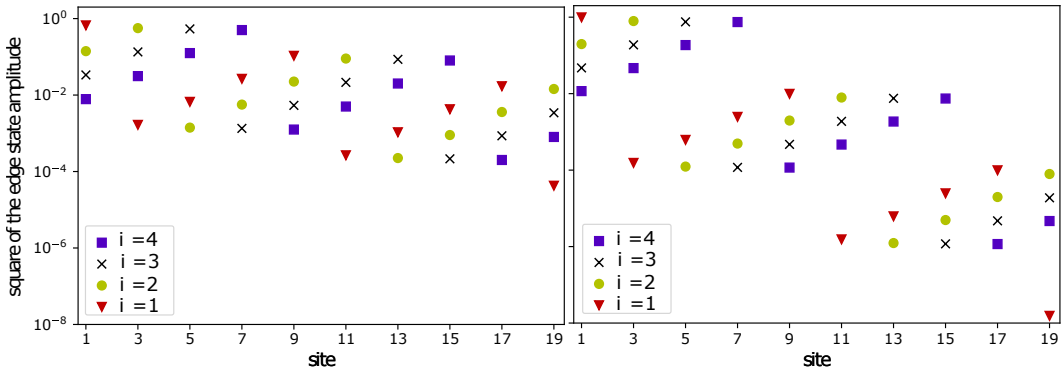

Figure 3.8: Edge state localization of the N, i-super-SSH model for the case $v > w$ ($v = 1.0$ and $w = 0.5$ were taken) fixed varying the free parameters v',w' and the position of the impurity for the case $N = 4$. (Top) $v' = 0.05$, $w' = 1.0$; (Bottom) $v' = 0.05$, $w' = 4.0$. Figure reproduced from Ref. [156].

the previous Case, a linear interface between topological and non-topological phases emerges.

Figure 3.8 shows the interesting and counter-intuitive behavior of the edge states localization in this case. From Fig. 3.7 we know that we require small values of v', and as w' is greater we find that the localization is reinforced. In addition, the position of the impurity again plays a key role since the edge state concentrates around its location, moving from previous sites and becoming more pronounced. Then, it presents a jump to a less localized form in the next supercell, where then it becomes mildly localized until eventually it becomes more localized and it jumps again. In this sense, the localization becomes more pronounced for impurities placed more toward the left in the supercell.

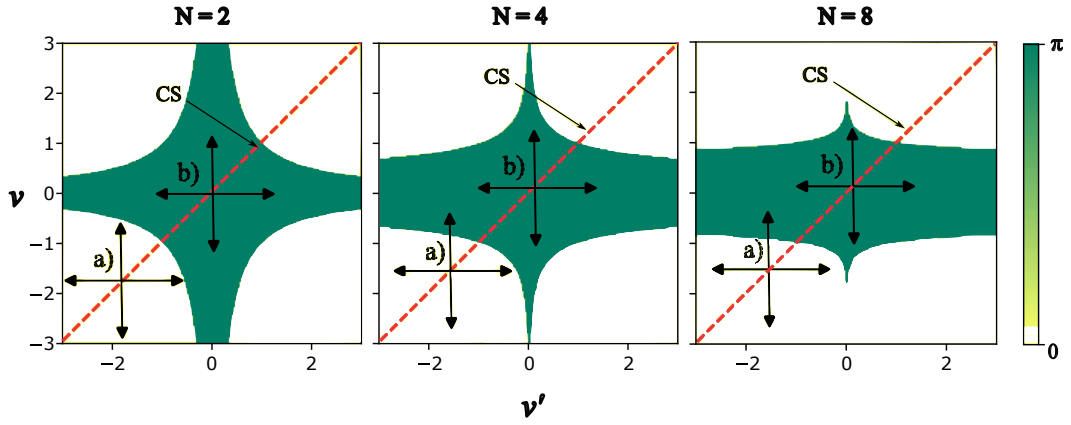

Figure 3.9: Berry phase in the space of free parameters of the N, i-super-SSH model for the case $w = w' = 1.0$ for different N values. Figure reproduced from Ref. [156].

3.4.3 Case C

Next we replicate the conditions of Case I with a different restriction over w', namely $w = w' = 1.0$. As can be observed from Fig. 3.9, the region in parameter space where the topological phase is found gets important modifications, relaxing the topological condition $v < w$ of the ordinary model. Furthermore, the topologically trivial and non-trivial phases are separated by a more intricated shape of the boundary. Note that for $N = 2$, the parameter space is symmetric under the exchange $v \leftrightarrow v'$. On the other hand, as the supercell length increases, the impact of the parameter v increases whereas the impact of v' reduces, and for large values of N, the boundaries of the topologically trivial and non-trivial phases of the model tends to be as in the original SSH model (Fig. 3.2). This makes sense because while N increases, the impurity density decreases and the effects of the impurity hoppings reduces.

Regarding the edge state localization, in Fig. 3.10 we observe the same behavior as in Case II. In Fig. 3.10(top), it can be seen that through the tuning of impurity hopping parameter, it is possible to reinforce the localization as compared to the original case. On the other hand, Fig. 3.10(bottom) shows the possibility of reaching to a non-typical non-trivial topological phase for values $v > w$. In both cases, the more to toward the left the impurity is located within the supercell, the more pronounced the localization becomes.

3.5 Topolectrical circuits Calculations

In this Section we explore again the topological phase structure of the (N, i)-super-SSH model from an analogue topolectrical circuit. For a self-contained discussion of

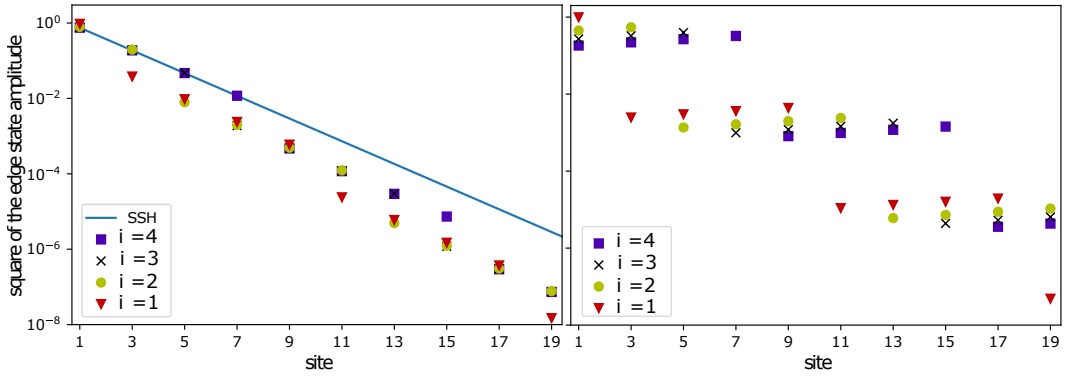

Figure 3.10: Edge state localization of the N, i-super-SSH model for the case $w = w' = 1.0$ varying the free parameters v,v' and the position of the impurity for the case $N = 4$. (Top) $v = 0.5$, $v' = 0.2$; (Bottom) $v = 1.1$, $v' = 0.05$. Figure reproduced from Ref. [156].

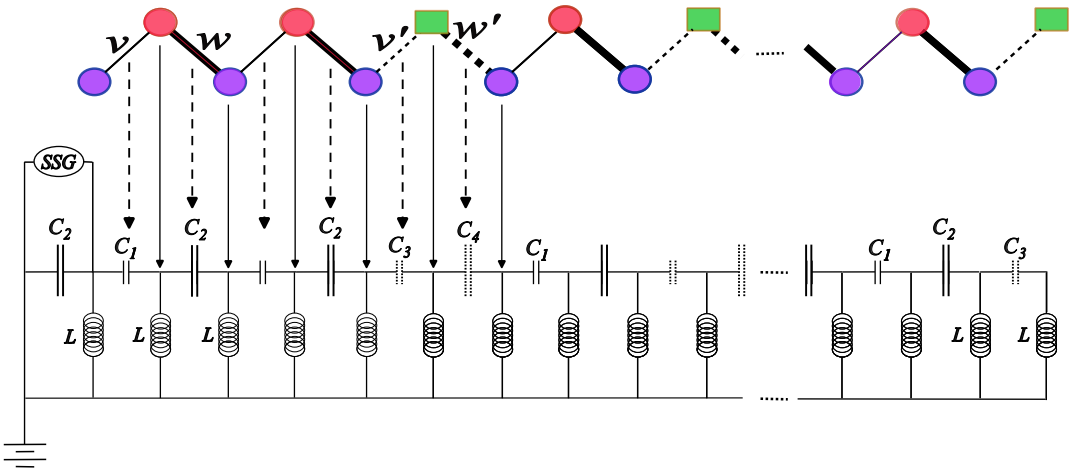

Figure 3.11: Topolectric circuit set up of the N, i-super-SSH model for $N = 4$ with the impurity placed in position $i = 4$. Figure reproduced from Ref. [156].

the subject, in the Supplement we present a brief introduction to the framework of topolectrical circuits and the analogy of their effective Hamiltonian with the Hamiltonian of a TB approach [197, 198, 199, 200, 201, 202]. The connection is established from the observation that the role of the hopping amplitudes in the TB approach are mapped to the capacitances C_i of capacitors in the network, whereas the "orbital" sites are considered as the nodes in which two capacitors and an inductor intersect. In order to get trace of the topological edge states, we look for a resonance in the impedance of the circuit with a sinusoidal signal probe. We further study the local-

ization of the states by the voltage drops in the nodes. We simulate our topolectrical circuit within the Pyspice package [207]. The topolectrical circuits in this case have the network structure shown in Fig. 3.11. For all the next calculations we computed the circuit's response to an sinusoidal input voltage current with amplitude of $V_0 = 10\text{V}$, frequency $f = 100\text{kHz}$, and inductance value $L = 10\mu\text{H}$.

3.5.1 Case A

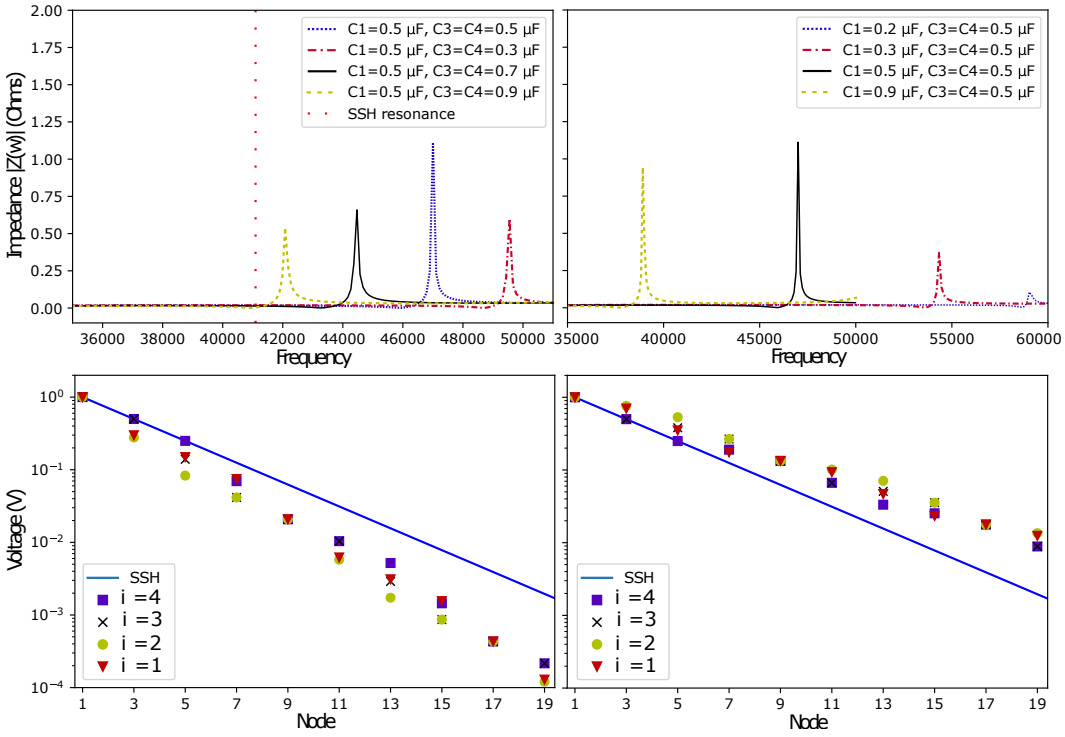

Figure 3.12: (Top) Impedance resonance $Z_r(\omega)$ for the values $C_2 = 1.0\mu\text{F}$ and (left) $C_1 = 0.5\mu\text{F}$, for different values of $C_3 = C_4$; (right) different values of C_1 with $C_3 = C_4 = 0.5\mu\text{F}$. (Bottom) Edge state localization of the N, i-super-SSH topolectrical circuit for the case $C_2 = 1.0\mu\text{F}$, (left) $C_1 = 0.5\mu\text{F}$, $C_3 = C_4 = 0.3\mu\text{F}$ and (right) $C_1 = 0.5\mu\text{F}$, $C_3 = C_4 = 0.7\mu\text{F}$, varying the position of the "impurity" (capacitors) for $N = 4$. Figure reproduced from Ref. [156].

In analogy with Case I of the TB calculation, we consider C_1 and C_3 as free parameters, fixing $C_2 = 1.0\mu\text{F}$ and with the condition $C_3 = C_4$, *i.e.* the same capacitance value to both nodes connected from the "impurity capacitor". In Fig. 3.12(top) we depict the expected resonances of the impedance (Z_r) of the circuit as a function of the frequency of the signal probe. Such resonance appears only when the systems

is found in the non-trivial topological phase [197, 198, 199, 200, 201, 202]. Figure 3.12(top, right) shows the behavior of the resonance under the variation of C_1. To understand the behavior of these curves, we recall that the resonance frequency for the original SSH model is found when

$$\omega_r = \frac{1}{\sqrt{L(C_1 + C_2)}}. \tag{3.5}$$

We draw these values of ω_r as vertical dotted lines in the Figure. We notice a deviation from these values in our model due to the "impurity" capacitances C_3 and C_4. We can conclude that, the value of C_1 slightly displaces the resonance peaks of the impedance. On the other hand, analyzing Fig. 3.12(top, left), as we fixed C_1 all

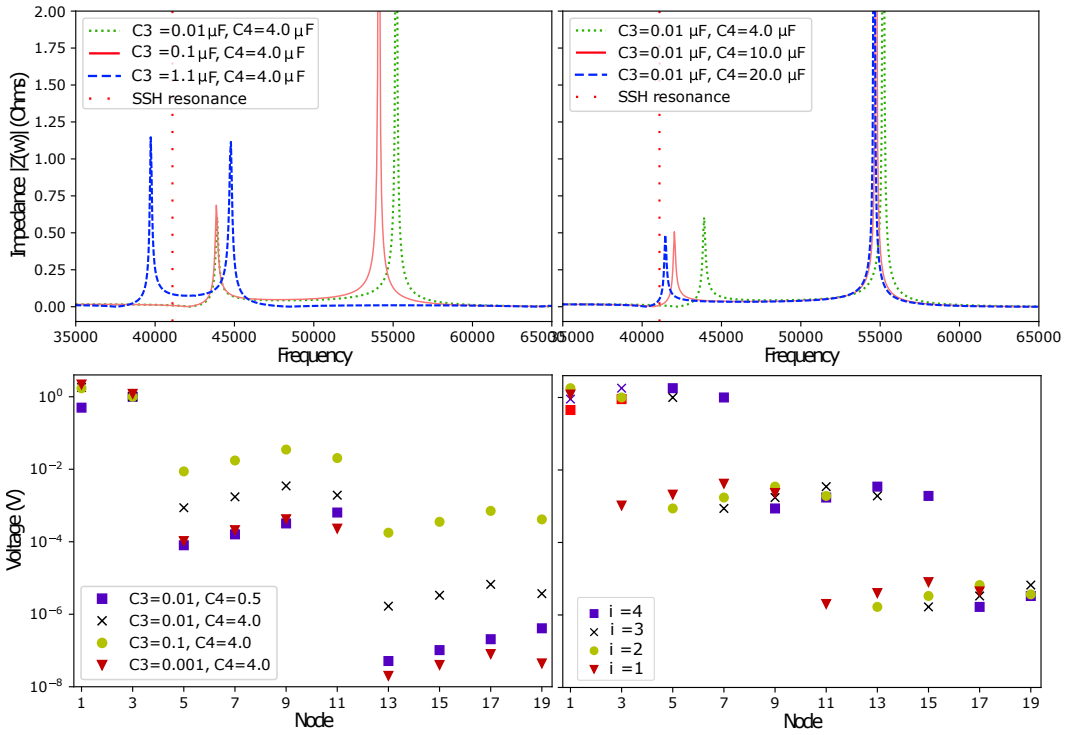

Figure 3.13: (Top) Impedance resonances $Z_r(\omega)$ for the values $C_2 = 1.0$ and (left) $C_1 = 0.5\mu$F, for different values of $C_3 = C_4\mu$F; (right) different values of C_1 with $C_3 = C_4 = 0.5\mu$F. (Bottom) Edge state localization of the N, i-super-SSH topolectrical circuit for the case $C_2 = 1.0\mu$F, (left) $C_1 = 0.5\mu$F, $C_3 = C_4 = 0.3\mu$F and (right) $C_1 = 0.5\mu$F, $C_3 = C_4 = 0.7\mu$F, varying the position of the "impurity" (capacitors) for $N = 4$. Figure reproduced from Ref. [156].

the resonance peaks share essentially the same impedance $Z(\omega)$ so that we can easily

detect that the effect of the variation of the $C_3 = C_4$ is to displace the resonance to the left of the frequency spectra as this parameter grows, approaching to the value of the original SSH resonance frequency, ω_r.

In close analogy with the wave function localization of the edge states, the voltage in the topological circuit is higher at the edge of the circuit. The voltage localization is shown in Fig. 3.12(bottom), where we can observe that for values $C_3 < C_1$ (bottom, left) the localization is reinforced with respect to the topolectrical SSH circuit shown in the blue line, while in the opposite case (bottom, right), the localization is weakened. The position of the "impurity" in the circuit also plays a role, reproducing the same behavior as in the TB calculations where the more to the right the impurity is located, the more pronounced the localization becomes. We must also mention that as in the TB calculation, the effect of the circuit length is irrelevant for long enough chains of circuit elements and that the effect of the supercell length is to dilute impurity effects as N gets large.

3.5.2 Case B

In this case we translate the conventions of Case II of the TB calculation, and study the well-known topologically nontrivial ($C_1 < C_2$) and trivial ($C_1 > C_2$) cases under the variation of the free parameters C_3 and C_4. We compute the impedance of the system and identify its resonant value Z_r upon varying the values of C_3 and C_4. We are mostly interested in the non-intuitive cases in which a non-trivial topological phase is found even though $C_1 > C_2$. In Fig. 3.13 we present the resonances of the impedance and the voltage localization for $C_1 = 1.1\mu$F, $C_2 = 1.0\mu$F, varying C_3 and C_4. From Fig. 3.13(top), we observe the appearance of a second resonance peak which contributes to voltage localization. It has been shown that Fano resonances [208] appear as a dispersion mechanism in the circuits [209, 210, 211], and that is the responsible of the asymmetry of the resonance peaks as well as the secondary peak appearance. The effect of C_4 is to slightly displace resonance peaks to the left as it grows. On the other hand, the effect of C_3 is to displace the resonances peaks to the left as it grows.

Voltage localization in the circuit is depicted in Fig. 3.13(bottom). We observe on the one hand the same behavior regarding the impurity position as in the TB approach, that is, a staggered localization around the impurity with jumps every supercell, and a reinforcing localization at the edge as the impurity is located more to the left. Also, keeping fixed the impurity position ($i = 2$), localization becomes more pronounced as C_3 and C_4 decrease (c.f. Fig. 3.8).

3.5.3 Case C

For this Case, which adopts the conventions of Case III of the TB calculation with $C_2 = C_4 = 1.0\mu$F, we focus our attention into the non-intuitive region in which even for $C_1 > C_2$ (notice that $C_1 = 2.0\mu$F is taken in Fig. 3.14(top)), a non-trivial topological phase develops. Thus, the only free parameter is actually C_3. The resonance peak of the impedance for the corresponding topolectrical circuit is plotted in Fig. 3.14(top) for different values of C_3.

Finally, in Fig. 3.14(bottom) we show the voltage drops in the different nodes of the topolectrical circuit for different values of $C_1 > 1\mu$F, C_3 and the impurity position, i. We observe the same behavior as with the TB approach: A staggered

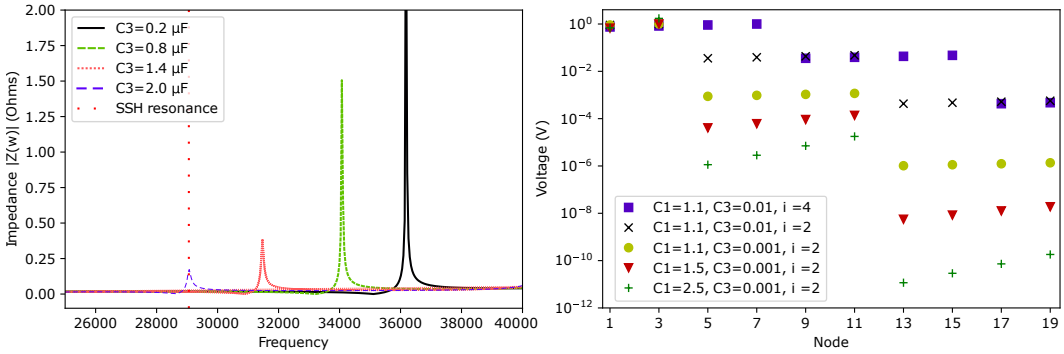

Figure 3.14: (Top) Impedance resonances $Z_r(\omega)$ for the values $C_2 = C_4 1.0\mu$F and $C_1 = 2.0\mu$F, for different values of C_3. (Bottom) Edge state localization of the N, i-super-SSH topolectrical circuit for the case $C_2 = C_4 = 1.0\mu$F varying the position of the "impurity" (capacitors) for $N = 4$. Figure reproduced from Ref. [156].

localization around the impurity with jumps every supercell, a reinforcing localization at the edge as the impurity places more to the left, and the greater C_1 and the smaller C_3 the more pronounced the localization becomes (compare with Fig. 3.10).

3.6 Discussion and Conclusions

In this Chapter we have performed an study of the effects of embedded impurity superlattices in the SSH model over electronic and topological properties of the system. We considered impurity effects through the modification of the hopping amplitudes between these impurities and their nearest neighbours in the array. Three different cases of these modified hoppings were considered: the Case I in which $w = 1.0$, $v' = w'$; Case II, where v, w where fixed (=1.0, 0.5, respectively, and vice versa); and Case III, in which $w = 1.0$, $w' = w$. We used two frameworks to explore the proteries of the system: the TB approach and a topolectrical circuit analogy.

Using the TB approach, for the Case I, we obtain no modification of the topological boundaries of the different phases of the model as compared to the original SSH model, indicating that this kind of impurities do not impact the topological condition for finding the topological phase of the model. Moreover, the position of the impurity within the supercell plays an important role in strengthening the localization of the edge-states, specially as the impurity location is more to the right edge of the supercell. For Cases II and III, non-intuitive, interesting boundaries of the topologically different phases were obtained: a linear boundary that separates topologically non-trivial and trivial phases, although the ordinary condition $v < w$ or $v > w$ is no longer required, and a non-linear-boundary between these phases. Effects are more notorious for small N, recovering the usual SSH model behavior for large N, as the impurity effects get diluted. In these cases, the position of the impurity within the supercell is important in the localization of the edge-states just as in the first case, but now reinforcing localization as the impurity is placed more to the left.

Using the topolectrical circuit analogue of the system, the expected resonances in the impedance of the circuit with a sinusoidal signal probe where found in each case, deviating from the resonant frequency ω_r of the original SSH model because of the presence of the impurity. The free parameters in each case are relevant in the position of the resonance peaks, while the same behavior in the voltage localization was realized as in the TB approach calculation. In all cases, the effect of the system length, n, is irrelevant for sufficiently long systems, with $n \leq 10$, while the supercell length, N, reduces the effect of the impurities in the systems as N gets larger, because of the impurity *dilution* in the system. The topolectrical circuit analogue of these models confirmed the results obtained in the TB approach. Additionally, within the numerical simulation of the circuit, the existence of other resonances was shown, related to Fano resonance in the system, and perhaps these are responsible of small differences between models. Even though, we conclude that topological circuits are as useful for studying electric and topological features of materials as TB calculations.

A general remark is that the results of this investigation provide evidence for the possibility of relaxing the conditions for the hopping amplitudes to distinguish between topologically trivial and non-trivial phases in the model and to provide a more tight localization of the edge-states by means of embedded impurity superlattices. Impurities in non-topological materials could be an important tool to provide them with topological features. Furthermore, impurities could be of interest for technological applications by tightening the localization of the wave vectors, that is, improving the surface conduction in these materials.

Supplements

3.A Topolectrical Circuits

Electrical circuits are described by Kirchoff's laws. Following [202], we start from Kirchoff's current law

$$I_a = \sum_i c_{ai}(V_a - V_i) + w_a V_A, \tag{3.6}$$

which establishes that the input current in a node, I_a, is equal to the current flowing out this node to other node i linked by a conductance c_{ai} plus the the current flowing to ground with impedance w_a^{-1}. Eq. (3.6) can be expressed in matrix form as

$$\vec{I} = (N + W)\vec{V} = J\vec{V}, \tag{3.7}$$

where N is the circuit *Laplacian* depending on the conductances, W is a diagonal matrix depending on the circuit's grounding, and $J = N + W$ is the grounded Laplacian, also called admittance matrix. Additionally, the Laplacian can be decomposed as $N = D - C$, with C the adjacency or conductances matrix and D a diagonal matrix representing the list of total currents out of each node. For LC circuits, the driving voltage frequency ω is the cornerstone. In this sense, it is convenient to Fourier transform Eq. (3.7), obtaining [202]

$$I_a(\omega) = \sum_b J_{ab}(\omega)V_b(\omega). \tag{3.8}$$

The admittance matrix now reads

$$J_{ab}(\omega) = i\omega[N_{ab}(\omega) + \delta_{ab}W_a(\omega)], \tag{3.9}$$

where

$$N_{ab}(\omega) = -C_{ab} + \frac{1}{\omega^2 L_{ab}}, \tag{3.10}$$

and

$$W_a(\omega) = C_a - \frac{1}{\omega^2 L_a} - \sum_c N_{ac}, \tag{3.11}$$

where C_{ab} and L_{ab} are the capacitance and inductance between nodes a and b, respectively, and C_a and L_a are the capacitance and inductance between nodes a and the ground. Most commonly, circuits are often studied by its voltage response to an applied current. This can be done through the corresponding impedance, Z. The two-point impedance is calculated as [212]

$$Z_{ab} = \frac{(V_a - V_b)}{I}, \tag{3.12}$$

where $I = |I_{ab}|$. Expression in Eq. (3.12) is used to calculate the impedance of different circuits throughout this Chapter. Expressing the potentials in terms of

the input current, that is inverting Eq. (3.7), we use the regularized circuit Green's function,

$$G = \sum_{j_n \neq 0} \frac{1}{j_n} \psi_n \psi_n^\dagger, \tag{3.13}$$

where j_n denotes the admittance eigenvalues of $\vec{J}$ and ψ_n is the corresponding $n-$dimensional eigenvector matrix. Notice that the admittance is defines as $Y = Z^{-1}$. Thus, it is possible to express the impedance as

$$Z_{ab} = \sum_{j_n \neq 0} \frac{|\psi_{na} - \psi_{nb}|^2}{j_n}, \tag{3.14}$$

that is, the sum of the squared modulus of the difference between of the $n-$th admittance eigenmode divided by the admittance eigenvalue. As can be seen from Eq. (3.14), the impedance becomes larger, namely, exhibits a resonance, if the admittance eigenmodes are well-localized at one region with small admittance eigenvalue j_n. This is the case of topological boundary resonances in topolectrical circuits, where there exists a large density of protected boundary modes with $j_n \approx 0$.

To make the correspondence between topolectrical circuits and Tight-Binding approaches, we should note that we are dealing with two eigenvalue equations:

$$\text{Circuits:} \qquad J\vec{V} \equiv j\vec{V} = \vec{I}, \tag{3.15}$$

$$\text{QM:} \qquad H\vec{\psi} = E\vec{\psi}. \tag{3.16}$$

If we relate the nodes in the topolectrical circuit to lattice sites, it is possible to establish the relation $J_{ab}(\omega) = i\omega H_{ab}(\omega)$, with $H(\omega)$ the Hamiltonian of the TB approach [202].

3.A.1 Topolectrical circuit of the (N, i)-super-SSH model.

The topolectrical analogue of the $(AB)^{N-1} - AC - SSH$ TB model in accomplished by considering the lattice sites as the nodes $1, 2, ...$ of the circuit in Fig. 3.11. The hopping amlitudes between sites A and B and vice versa are set as capacitance values C_1 and C_2, respectively. An impurity is represented by a change in the capacitance linking its site with its nearest neighbours sites by the values of C_3 and C_4 (Fig. 3.11).

The two-point impedance is calculated using Eq. (3.12) by measuring the voltage in node 1. Additionally, the voltage localization is computed by measuring the voltage in each node.

For comparative reasons, it is be useful to establish some characteristics of the original topolectrical SSH circuit ($C_3 = C_1$ and $C_4 = C_2$) [202]. First, when the condition $C_1 < C_2$ fulfills, a topological boundary mode exists, leading to a drastic increase in impedance (resonance) which presents in the resonant frequency (3.5).

Also, applying an alternate current probe generates potential differences between the plates of each capacitor, V_1 and V_2 for capacitors C_1 and C_2, respectively, which indeed oscillate in anti-phase. When $C_1 < C_2$, the potential configuration on the nodes (mid-gap mode) is given by $\psi_0(n)\alpha(1, 0, -t, 0, t^2, 0 - t^3, 0, ..., ((-t]^n, 0))$, with $t = C_1/C_2$. In the opposite case in which $C_1 > C_2$ ($t > 1$), there exists no topological boundary mode and no mid-gap node is found. Finally, In terms of the grounded Laplacian, the system with periodic boundary conditions is described by

$$J_{SSH}(k_x) = i\omega \left(C_1 + C_2 - \frac{1}{\omega^2 L} \right) I - i\omega \left[(C_1 + C_2 \cos k_x)\sigma_x + C_2 \sin k_x \sigma_y \right]. \quad (3.17)$$

Chapter 4

Non-Relativistic JR Soliton

We consider the Foldy-Whouthuysen (FW) transformation [213] of the Dirac equation coupled to a background soliton field which is equivalent to a position-dependent mass $m(x)$ such that at each limit $x \to \pm\infty$, the mass to the left and to the right tends to a (possibly different) constant, with a sign difference at each side. We then build-up a third order unitarily transformed Schrödinger-like Hamiltonian as a counterpart of the corresponding to the well known Jackiw-Rebbi model [214]. By further FW-transforming the Dirac spinor, we establish the relation between the non-relativistic and relativistic wave functions up to this order of approximation for generic position dependent mass profiles. For the economic choice $m(x) = m_0 x/|x|$, we find that these spinors are the same up to an overall constant. The discussion in this Chapter is based in our paper, Ref. [215].

4.1 Foldy-Wouthuysen transformation

We focus our attention in the non-relativistic representation of the JR kink as derived from the FW transformation [213] of the Dirac equation with a position dependent mass term [216, 217]. We commence by diagonalizing the Hamiltonian in Eq. (2.22) with the corresponding unitary transformation for the FW representation,

$$U(x) \equiv e^{iS}, \tag{4.1}$$

with

$$S \equiv -\frac{i}{2}\frac{1}{\sqrt{m}}\beta\alpha p_x \frac{1}{\sqrt{m}}. \tag{4.2}$$

By explicitly representing the Dirac matrices as

$$\alpha \equiv \sigma_x, \qquad \beta \equiv \sigma_z, \tag{4.3}$$

we write the Dirac Hamiltonian

$$H_0 \equiv \sigma_x p_x + \sigma_z m\left(x\right), \tag{4.4}$$

and the transformation in eq. (4.2) as

$$S \equiv \frac{1}{2}\frac{1}{\sqrt{m}}\sigma_y p_x \frac{1}{\sqrt{m}}. \tag{4.5}$$

In the spirit of the FW transformation, we seek to write the stationary eq. (2.22) in the form

$$H\Psi = E\Psi, \tag{4.6}$$

with the transformed Hamiltonian and wavefuction given by

$$\begin{aligned} H &\equiv U\left(x\right) H_0 U^{\dagger}\left(x\right) = e^{iS} H_0 e^{-iS}, \\ \Psi &\equiv U\left(x\right)\psi = e^{iS}\psi. \end{aligned} \tag{4.7}$$

Then, by exploiting the Baker–Campbell–Hausdorff formula, we approximate upto third order

$$H \approx H_0 + i\left[S, H_0\right] - \frac{1}{2}\left[S,\left[S, H_0\right]\right] + \ldots \tag{4.8}$$

Working out explicitly the first commutator, we find

$$\begin{aligned} \left[S, H_0\right] &= i\left(H_0 - m\sigma_z - \frac{1}{2}\sigma_z\left\{\frac{1}{\sqrt{m}}p_x\frac{1}{\sqrt{m}}, p_x\right\}\right) \\ &= \left[\frac{1}{2}\frac{1}{\sqrt{m}}p_x\frac{1}{\sqrt{m}}\sigma_y, p_x\sigma_x + m\sigma_z\right] \\ &= \left[S, p_x\sigma_x\right] + \left[S, m\sigma_z\right], \end{aligned} \tag{4.9}$$

from where we derive the following useful relations,

$$\begin{aligned} \left[S, p_x\sigma_x\right] &= -\frac{i}{2}\sigma_z\left\{\frac{1}{\sqrt{m}}p_x\frac{1}{\sqrt{m}}, p_x\right\} \\ \left[S, m\sigma_z\right] &= i\sigma_x p_x. \end{aligned} \tag{4.10}$$

Next, the commutator

$$\begin{aligned} \left[S,\left[S, H_0\right]\right] &= \left[S, i\left(\sigma_x p_x - \frac{1}{2}\sigma_z\left\{\frac{1}{\sqrt{m}}p_x\frac{1}{\sqrt{m}}, p_x\right\}\right)\right] \\ &\approx i\left[S, \sigma_x p_x\right] + \ldots \\ &= \frac{1}{2}\sigma_z\left\{\frac{1}{\sqrt{m}}p_x\frac{1}{\sqrt{m}}, p_x\right\}, \end{aligned} \tag{4.11}$$

from which we directly find that at the third order,

$$H \approx \left(\frac{1}{4}\left\{\frac{1}{\sqrt{m}}p_x\frac{1}{\sqrt{m}}, p_x\right\} + m\right)\sigma_z. \tag{4.12}$$

Notice that this Schrödinger-like Hamiltonian is quadratic in the momentum with a non-trivial dependence of the position dependent mass, as demanded by hermiticity of H. A similar form of the hamiltonian was proposed in Ref. [217] precisely as the effective Schrödinger equation for position dependent mass of charge carriers.

For the wave function, we have

$$\begin{aligned}\Psi_0 &= e^{\frac{i}{2}\frac{1}{\sqrt{m}}p_x\frac{1}{\sqrt{m}}\sigma_y}e^{-\int_{x_0}^{x} dy\ m(y)}\chi \\ &= \left(\cos\left(\frac{1}{2}\frac{1}{\sqrt{m}}p_x\frac{1}{\sqrt{m}}\right) + i\sin\left(\frac{1}{2}\frac{1}{\sqrt{m}}p_x\frac{1}{\sqrt{m}}\right)\sigma_y\right) \\ &\times\ e^{-\int_{x_0}^{x} dy\ m(y)}\chi,\end{aligned} \tag{4.13}$$

but since χ is an eigenvector of σ_y with eigenvalue $+1$,

$$\begin{aligned}\Psi_0 &= \left(\cos\left(\frac{1}{2}\frac{1}{\sqrt{m}}p_x\frac{1}{\sqrt{m}}\right) + i\sin\left(\frac{1}{2}\frac{1}{\sqrt{m}}p_x\frac{1}{\sqrt{m}}\right)\right) \\ &\times\ e^{-\int_{x_0}^{x} dy\ m(y)}\chi \\ &= e^{\frac{i}{2}\frac{1}{\sqrt{m}}p_x\frac{1}{\sqrt{m}}}e^{-\int_{x_0}^{x} dy\ m(y)}\chi.\end{aligned} \tag{4.14}$$

Writting formally that

$$e^{\frac{i}{2}\frac{1}{\sqrt{m}}p_x\frac{1}{\sqrt{m}}} = \sum_{n=0}^{\infty}\frac{1}{2^n n!}\left(\frac{1}{\sqrt{m}}\frac{d}{dx}\frac{1}{\sqrt{m}}\right)^n, \tag{4.15}$$

we cast the wavefunction in the form

$$\Psi_0 = \sum_{n=0}^{\infty}\frac{1}{2^n n!}\left(\frac{1}{\sqrt{m}}\frac{d}{dx}\frac{1}{\sqrt{m}}\right)^n e^{-\int_{x_0}^{x} dy\ m(y)}\chi. \tag{4.16}$$

Let us observe that

$$\begin{aligned}&\left(\frac{1}{\sqrt{m}}\frac{d}{dx}\frac{1}{\sqrt{m}}\right)e^{-\int_{x_0}^{x} dy\ m(y)} \\ &\qquad = \left(\frac{1}{2}\frac{d}{dx}\left(\frac{1}{m}\right) - 1\right)e^{-\int_{x_0}^{x} dy m(y)} \\ &\qquad \equiv f_1(m)\, e^{-\int_{x_0}^{x} dy\ m(y)}.\end{aligned} \tag{4.17}$$

Similarly,

$$\begin{aligned}\left(\frac{1}{\sqrt{m}}\frac{d}{dx}\frac{1}{\sqrt{m}}\right)^2 & e^{-\int_{x_0}^{x} dy\ m(y)} \\ &= \left[\frac{1}{m}\frac{d}{dx}f_1(m) + (f_1(m))^2\right] e^{-\int_{x_0}^{x} dy\ m(y)} \\ &\equiv f_2(m)\, e^{-\int_{x_0}^{x} dy\ m(y)}. \end{aligned} \tag{4.18}$$

From here, we define the recurrence relation

$$\begin{aligned}\left(\frac{1}{\sqrt{m}}\frac{d}{dx}\frac{1}{\sqrt{m}}\right)^{n+1} & e^{-\int_{x_0}^{x} dy\ m(y)} \\ &= \left[\frac{1}{m}\frac{d}{dx}f_n(m) + f_1(m)\, f_n(m)\right] e^{-\int_{x_0}^{x} dy\ m(y)} \\ &= f_{n+1}(m)\, e^{-\int_{x_0}^{x} dy\ m(y)}. \end{aligned} \tag{4.19}$$

Let us further notice that

$$\begin{aligned} f_{n+1}(m) &= \left[\frac{1}{m}\frac{d}{dx} + f_1(m)\right] f_n(m) \\ &\equiv Df_n(m), \end{aligned} \tag{4.20}$$

from which we can write

$$f_{n+1}(m) = D^n f_1(m). \tag{4.21}$$

Then

$$\begin{aligned}\Psi_0 &= \sum_{n=0}^{\infty}\frac{1}{2^n n!}\left(\frac{1}{\sqrt{m}}\frac{d}{dx}\frac{1}{\sqrt{m}}\right)^n e^{-\int_{x_0}^{x} dy\ m(y)}\chi \\ &= \psi_0 + \sum_{n=1}^{\infty}\frac{1}{2^n n!}\left(\frac{1}{\sqrt{m}}\frac{d}{dx}\frac{1}{\sqrt{m}}\right)^n e^{-\int_{x_0}^{x} dy\ m(y)}\chi \\ &= \left(1 + \sum_{n=1}^{\infty}\frac{D^n}{2^n n!}f_1(m)\right)\psi_0 \\ &\equiv \left(1 + \left(e^{\frac{D}{2}} - 1\right)[f_1(m)]\right)\psi_0. \end{aligned} \tag{4.22}$$

This expression determines the FW representation of the JR kink in terms of the original zero mode for arbitrary shape of the mass profile.

4.2 Step function

For illustration, let us consider the profile [218, 87, 92]

$$m(x) = m_0 \frac{x}{|x|}. \tag{4.23}$$

It is straightforward to check that in this case,

$$D^n f_1(m) = (-1)^n, \tag{4.24}$$

such that, from (4.22), we directly obtain

$$\Psi_0 = \frac{1}{\sqrt{e}} \psi_0, \tag{4.25}$$

namely, both the spinors differ by an overall constant (Fig. 1).

4.3 Tanh function

Another example is a mass profile given by

$$m(x) = m_0 \tanh(x). \tag{4.26}$$

In this case, the 3^{rd}-order FW zero mode wave function is given by

$$\Psi_0 = \frac{1}{\sqrt{e}} e^{\frac{m_0}{4} \mathrm{csch}^2(\mathrm{x})} \psi_0. \tag{4.27}$$

Both, the relativistic and the FW non-relativistic approximation wave functions are plotted in Fig. 2, where it can be noted that the functions differ not only in magnitude but in shape as well.

4.4 Discussion and Conclusions

In this Chapter we have carried out the FW transformation of the Dirac Hamiltonian (4.4) with a position dependent mass term. We have focused out attention to the zero mode, which exhibits a kink behavior for different mass profiles. This zero mode transforms according to (4.22) for a general $m(x)$. Explicit examples are depicted in Figs. 4.1 and 4.2. Although the form of the zero mode depends upon the explicit representation of the Dirac matrices α and β, it is well-known that the Pauli matrices form a basis for 2D Dirac Hamiltonians, and it is possible to use different selections of these basis elements (similarity transformation of basis) in the Hamiltonian, *e. g.*

$$H = \sigma_y p + \sigma_x m(x), \tag{4.28}$$

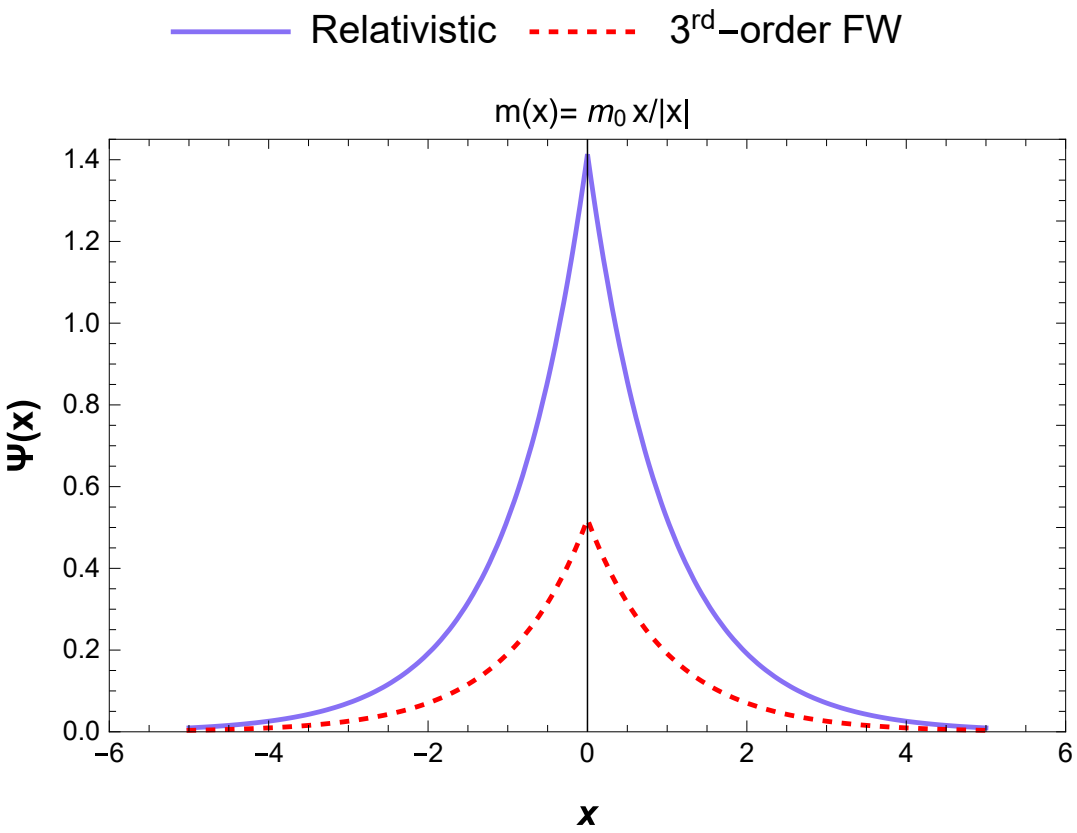

Figure 4.1: Zero mode wave functions for the relativistic case and the 3^{rd}-order FW non-relativistic approximation for the mass profile $m(x) = m_0 \frac{x}{|x|}$. Figure reproduced from Ref. [215].

so that the systems describes the same physics.

A final word of caution is required. It should be clear that ψ_0 is not a solution of

$$U^{\dagger}(x) H U(x)\ \psi_0 = 0. \tag{4.29}$$

This is because the transformation (4.22) is valid up to third order and thus is not exact. Nevertheless, we observe that up to this approximation, the kink character of the relativistic and non-relativistic spinors holds.

Further non-relativistic FW-like representations of Dirac Hamiltonians of this type are being considered, like the non-minimally coupled electric-Moshinsky oscillator [92]. These ideas are currently under consideration and results shall be presented elsewhere.

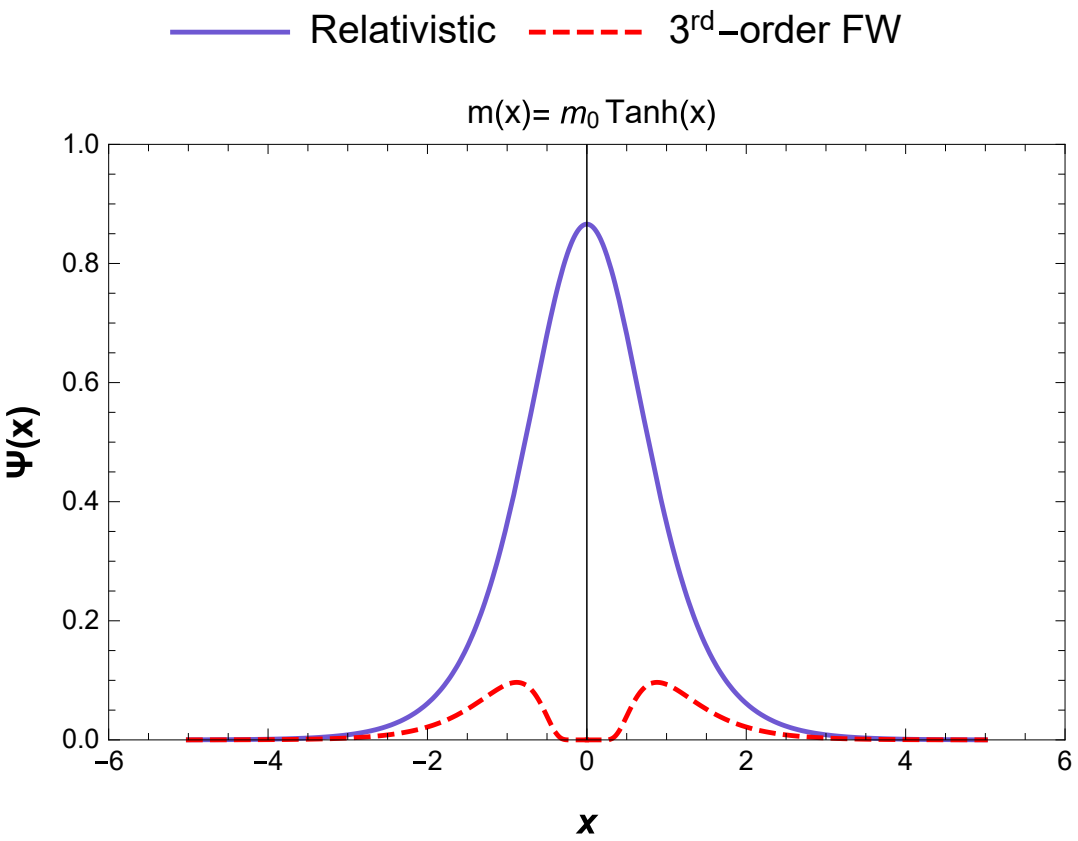

Figure 4.2: Zero mode wave functions for the relativistic case and the 3^{rd}-order FW non-relativistic approximation for the mass profile $m(x) = m_0 \tanh(x)$. Figure reproduced from Ref. [215].

Chapter 5

Weyl Semimetals in External EM Fields

Within a Supersymmetric Quantum Mechanics (SUSY-QM) framework [219], the (3+1) Dirac equation describing a Dirac material in the presence of external parallel electric and magnetic fields is solved. Considering static but non-uniform electric and magnetic profiles with translational symmetry along the y-direction, the Dirac equation is transformed into two decoupled pairs of Schrödinger equations, one for each chirality of the fermion fields. Taking trigonometric and hyperbolic profiles for the vector and scalar potentials, respectively, we arrive at SUSY partner Pöschl-Teller-like quantum potentials. Restricting to the conditions of the potentials that support an analytic zero-mode solution, we obtain a nontrivial current density perpendicular to the electric and magnetic fields, thus, defining a plane where these three vectors become coplanar, indicating the possibility of realizing the Planar Hall Effect [153]. Furthermore, this non-vanishing current density is the sum of current densities for the left- and right-chiralities, suggesting that the net current is a consequence of chiral symmetry. Possible application in current steering of solitonic nature through a Type-I Weyl semimetal is discussed. This Chapter bases its discussion in Ref. [220, 221].

5.1 Introduction

Understanding the dynamics of electrons under the influence of external electromagnetic fields lies at the very heart of quantum mechanics [222, 223, 224]. Not surprisingly, the influence of external fields results in a plethora of quantum phenomena. Addressing the problem under the most general assumptions regarding field configurations is indeed a hard nut to crack. A number of simplifications have been considered since the early days of the establishment of quantum physics. For

example, for static fields, the quantization of electron orbitals in the plane perpendicular to the field lines of a uniform magnetic field, the Landau levels [225], are the cornerstone in the description of several quantum phenomena [226]. Adding an electric field parallel to the Landau levels plane generates an electric current perpendicular to both fields. For finite size samples, the quantization of the electric resistance is observed in the Quantum Hall effect (QHE) [227, 228] whose smoking gun is the development of plateaus in the transverse conductivity of a bi-dimensional sample of a two-dimensional electron gas at integer numbers of the so-called filling factor, which counts the number of Landau levels filled in the sample. The quantization rule for the conductivity has also been found for non-integer values of the filling factor [229] as a result of electron-electron interactions which become relevant [230]. Even more, in the anomalous quantum Hall effect [231, 232, 233] which emerges for relativistic-like excitations in graphene and related materials, it is precisely the relativistic nature of the excitations which describes a sort of integer QHE, with a shifted plateaus. This particular example establishes a natural connection of condensed matter and high-energy physics [234]. The importance of the QHE can be further established by the close relation of this effect and the superconducting properties of spin liquid systems [235]. Thus, it is natural to expect the response of charged particles to external fields in variants of this effect.

For time varying fields, like those generated during relativistic heavy-ion collisions in RHIC and LHC [236], it was conjectured that the non-trivial nature of the quantum chromodynamics vacuum could be probed through the generation of a non-dissipative electric current generated by the chiral imbalance of quarks interacting with topological sectors of the gauge field [237, 238, 239]. Chiral anomaly is responsible for the imbalance in this effect. Nevertheless, a number of thorough measurements in isobaric collisions showed no evidence of the chiral magnetic effect (CME) [240, 241]. An (Abelian) analogue of the CME was found in $ZrTe_5$ [242, 243, 244, 245]. For that case, rather than topological configurations of the gauge fields, it is a setup where electric and magnetic fields are parallel which is responsible for the effect. Remarkably, the chiral anomaly generated by the effect of parallel electric and magnetic fields has also been related to the emergence of a positive longitudinal magnetoconductance [246] in Dirac materials. Along with non-trivial effects of Berry curvature, the chiral anomaly also gives rise to the so-called Planar Hall Effect (PHE) [247] that contrary to the standard QHE setup, in this case the applied current, magnetic field, and the transverse voltage lie coplanarly.

In this Chapter we explore the possibility of realizing the PHE by static but non-uniform electric and magnetic fields, as can be naturally addressed in the context of θ-electrodynamics (see, for instance, Ref. [248]). For this purpose, we factorize the four-component Dirac equation under the influence of parallel electric and magnetic fields along the third spatial dimension in terms of two decoupled two-component Weyl-type equation corresponding to each chirality. Each bi-spinor equation can be

further factorized in the standard procedure of supersymmetric quantum mechanics. Considering Pöschl-Teller-like quantum potentials, we look for the conditions of these potentials to support a zero-mode analytic solution. Interestingly, this mode leads to a non-trivial electric current in the same plane of the electric and magnetic field, but perpendicular to both. To present the details of our findings, we have organized the remaining of this Chapter as follows: In Sec. 5.2 we recall the covariant form of the (3+1) Dirac equation in the presence of external electromagnetic fields. Later, in Sec. 5.4, we consider a confining example of scalar and vector potentials which leads to a novel chiral Planar Hall Effect. Finally, in Sec. 5.5 we discuss some aspects and consequences of the aforementioned effect and draw some conclusions. Additionally we have included a Supplement tackling the SUSY-QM technique.

5.2 Dirac equation in electromagnetic fields

The Dirac equation describing the motion of free electrons is given by

$$(i\gamma^{\mu}\partial_{\mu} - m)\Psi_D(\mathbf{x}) = 0, \tag{5.1}$$

where $\Psi_D(\mathbf{x})$ is a four-component spinor, and the Dirac γ^{μ}-matrices fulfill the *Clifford* algebra $\{\gamma^{\mu}, \gamma^{\nu}\} = 2g^{\mu\nu}$, with $g^{\mu\nu} = \mathrm{diag}(1, -1, -1, -1)$ being the (3+1)-dimensional Minkowsky space-time metric. We choose to work in the Dirac representation of these matrices [1],

$$\gamma^0 = \beta = \begin{pmatrix} 1 & 0 \\ 0 & -1 \end{pmatrix}, \ \gamma^i = \beta\alpha_i = \begin{pmatrix} 0 & \sigma_i \\ -\sigma_i & 0 \end{pmatrix},$$

$$\alpha_i = \begin{pmatrix} 0 & \sigma_i \\ \sigma_i & 0 \end{pmatrix}, \ \gamma^5 = i\gamma^0\gamma^1\gamma^2\gamma^3 = \begin{pmatrix} 0 & 1 \\ 1 & 0 \end{pmatrix}. \tag{5.2}$$

It is worth noticing that we are working in natural units $\hbar = c = e = 1$, where c is the speed of light and e is the electron charge. However, in Dirac materials, the Dirac-like equation describing them has a factor directly proportional to the Fermi velocity v_F instead of c (see, for example, Ref. [249]), thus, the system addressed here is not relativistic[2]. In order to formulate the Dirac equation in the presence of electromagnetic fields, we start by taking the minimal coupling rule $\pi_{\mu} = i\partial_{\mu} - A_{\mu}$ which incorporates the electromagnetic potentials $A_{\mu} = (\Phi, \mathbf{A})$ in the Dirac equation. Thus, Eq. (5.1) becomes

$$(\gamma^{\mu}\pi_{\mu} - m)\Psi_D(\mathbf{x}) = 0. \tag{5.3}$$

[1] One might have started with a chiral representation of the γ-matrices, *i.e.* the Weyl equation, arriving at the same physics.

[2] Even though the system is not relativistic, inside these materials v_F plays the role of c, and a "Lorentz invariance" inside the material is conserved [250]. In this sense, this theory only applies to type-I Weyl semimetals.

Since in Dirac materials the charge carriers behave as massless electrons, the quasiparticle excitations are described by an effective massless Dirac equation. Thus, it is easy to show that the squared operator[3] $(\gamma \cdot \pi)^2$ can be written as follows

$$(\boldsymbol{\gamma} \cdot \boldsymbol{\pi})^2 = \pi^2 + \frac{\sigma^{\mu\nu}}{2} F_{\mu\nu}, \tag{5.4}$$

where $\sigma^{\mu\nu} = \frac{i}{2}[\gamma^\mu, \gamma^\nu]$, and

$$F_{\mu\nu} = [\pi_\mu, \pi_\nu] = \begin{pmatrix} 0 & E_x & E_y & E_z \\ -E_x & 0 & -B_z & B_y \\ -E_y & B_z & 0 & -B_x \\ -E_z & -B_y & B_x & 0 \end{pmatrix}, \tag{5.5}$$

is the electromagnetic field tensor [251]. Let us analyse each term in Eq. (5.4) separately. First,

$$\pi^2 = -\partial_t^2 - i\frac{\partial A_0}{\partial t} - 2iA_0\partial_t + A_0^2 + \partial_j^2 + i\frac{\partial A_j}{\partial x^j} + 2iA_j\partial_j - A_j^2. \tag{5.6}$$

On the other hand, noticing that

$$\frac{\sigma^{0\nu}}{2} F_{0\nu} = \frac{i}{2}\alpha_i F_{0i} = \frac{i}{2}(\alpha_1 F_{01} + \alpha_2 F_{02} + \alpha_3 F_{03}), \tag{5.7}$$

$$\frac{\sigma^{ij}}{2} F_{ij} = -\frac{1}{2}\epsilon_{ijk} F_{ij} I \otimes \sigma_k = -I \otimes (\sigma_3 F_{12} - \sigma_2 F_{13} + \sigma_1 F_{23}), \tag{5.8}$$

where $I = I_{2\times 2}$ is the identity matrix, the second term can be written as

$$\frac{\sigma^{\mu\nu}}{2} F_{\mu\nu} = \frac{i}{2}(\alpha_1 F_{01} + \alpha_2 F_{02} + \alpha_3 F_{03}) - I \otimes (\sigma_3 F_{12} - \sigma_2 F_{13} + \sigma_1 F_{23}), \tag{5.9}$$

where we have used the relations $[\gamma^0, \gamma^i] = 2\alpha_i$, $[\gamma^i, \gamma^j] = i2\epsilon_{ijk}\sigma_k \otimes I_{2\times 2}$, $F_{\mu\nu} = -F_{\nu\mu}$ and $\sigma^{\mu\nu} = -\sigma^{\nu\mu}$. Equation (5.4) together with the expressions in Eqs. (5.6) and (5.9) represent all the possible configurations of electromagnetic fields coupled to the Dirac equation describing the dynamics of fermions under its influence. In particular, we are interested in configurations allowing the use of the Supersymetric Quantum Mechanics (SUSY-QM) to solve the eigenvalue problem of the Dirac Hamiltonian. It has been demonstrated that when we only consider a magnetic field perpendicular to the $x-y$ plane, where fermions are constrained to move, the system can be solved within a SUSY framework (see, for example, Ref. [252]). Analogously, in the case of an electric field pointing along the x-direction, SUSY-QM is also a framework useful

[3]Note that, as the Dirac equation is homogeneous, the solutions of the squared problem are solutions of the original problem as well. In fact, when decoupling the original system of equations it results in the squared Hamiltonian operator applied to the solutions.

to find the respective solutions [253]. On the other hand, from Eq. (5.9) we observe that a configuration of magnetic and electric fields does not lead to a system of equations which can be solved by a suitable SUSY-QM. Below we study a particular setup in which the system exhibits supersymmetry.

5.3 Parallel EM fields configuration

Let us consider a static parallel fields configuration, namely, a magnetic field $\mathbf{B} = B(x)\,\hat{\mathbf{z}}$ and an electric field $\mathbf{E} = E(z)\,\hat{\mathbf{z}}$. Working in the Landau gauge, the vector potential generating $\mathbf{B}$ can be chosen as $\mathbf{A} = A(x)\,\hat{\mathbf{y}}$. Moreover, since the rotational of the electric field is equal to zero, this field is generated by a electric scalar potential $\phi(z)$. Thus, the field strengths turn out to be

$$B(x) = \frac{dA(x)}{dx}, \quad E(z) = -\frac{d\phi(z)}{dz}. \tag{5.10}$$

In this physical situation, the operator π^2 is simplified to the following form

$$\pi^2 = -\partial_t^2 - i2\phi(z)\partial_t + \phi^2(z) + \partial_x^2 + \partial_y^2 + \partial_z^2 + i2A(x)\partial_y - A^2(x), \tag{5.11}$$

while the term $\sigma^{\mu\nu}F^{\mu\nu}/2$ is explicitly written as

$$\frac{\sigma^{\mu\nu}}{2}F^{\mu\nu} = \begin{pmatrix} B(x) & 0 & iE(z) & 0 \\ 0 & -B(x) & 0 & -iE(z) \\ iE(z) & 0 & B(x) & 0 \\ 0 & -iE(z) & 0 & -B(x) \end{pmatrix}. \tag{5.12}$$

On the other hand, we assume the *spinor* $\Psi_D(t,x,y,z)$, such that

$$(\gamma\cdot\pi)^2\Psi_D(t,x,y,z) = 0,$$

has a standard stationary temporal behavior and since the system exhibits translational symmetry along the y-direction, we propose $\Psi_D(t,x,y,z)$ as follows,

$$\Psi_D(t,x,y,z) = e^{i(\varepsilon t+ky)}\Psi(x,z) = e^{i(\varepsilon t+ky)}\begin{pmatrix} \psi_{\uparrow}^{\alpha} \\ \psi_{\downarrow}^{\beta} \\ \psi_{\uparrow}^{\beta} \\ \psi_{\downarrow}^{\alpha} \end{pmatrix}, \tag{5.13}$$

with ε being the energy of the Dirac electron and k its wavenumber in the y-direction. Then, the time-independent *spinor* $\Psi(x,z)$ fulfills an eigenvalue problem that is equivalent to the following coupled system of equations

$$\left\{\left[\partial_x^2 - (k+A(x))^2 \pm \frac{dA(x)}{dx}\right] + \left[\partial_z^2 + (\phi(z)+\varepsilon)^2\right]\right\}\psi_{\uparrow\downarrow}^{\alpha,\beta} \mp i\frac{d\phi(z)}{dz}\psi_{\uparrow\downarrow}^{\beta,\alpha} = 0, \tag{5.14}$$

where the arrows $\uparrow\downarrow$ specify the spin orientation. The above system can be decoupled defining

$$\varphi^{\pm}_{\uparrow\downarrow} \equiv \psi^{\alpha}_{\uparrow\downarrow} \pm \psi^{\beta}_{\uparrow\downarrow}, \tag{5.15}$$

such that we are lead to the following system of equations

$$\left[\left(-\partial_x^2 + (k + A(x))^2 - \frac{dA(x)}{dx}\right) + \left(-\partial_z^2 - (\phi(z) + \varepsilon)^2 \pm i\frac{d\phi(z)}{dz}\right)\right]\varphi^{\pm}_{\uparrow} = 0, \tag{5.16a}$$

$$\left[\left(-\partial_x^2 + (k + A(x))^2 + \frac{dA(x)}{dx}\right) + \left(-\partial_z^2 - (\phi(z) + \varepsilon)^2 \mp i\frac{d\phi(z)}{dz}\right)\right]\varphi^{\pm}_{\downarrow} = 0. \tag{5.16b}$$

Before proceeding, let us briefly review the SUSY-QM framework, in which two

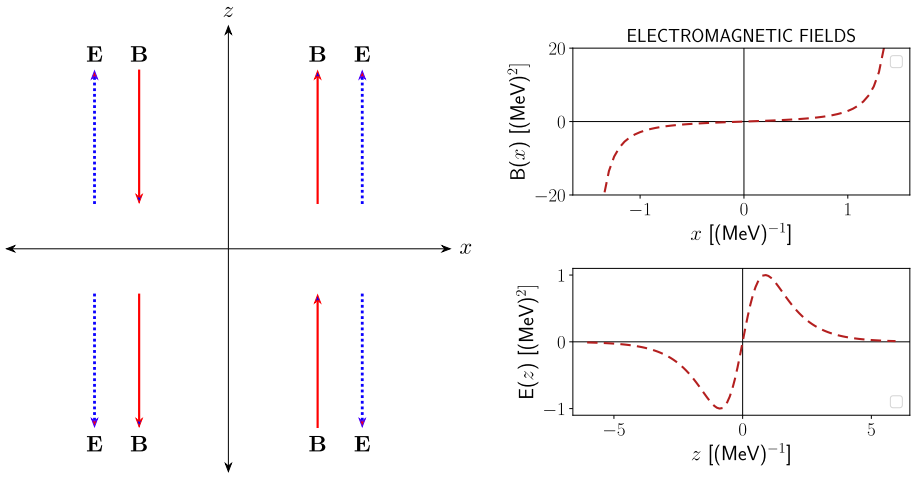

Figure 5.1: Sketch of the alignment of the fields in the plane $x - z$ (left). The electromagnetic fields generated by the potentials in Eq. (5.26) (right). The scale of the graphs is set by parameters $E_0 = 2.0$, $B_0 = 1.0$, $\mu = 1.0$ and $\nu = 1.0$. Note that we are using natural units, $\hbar = c = e = 1$. Figure reproduced from Ref. [220].

Schrödinger-like Hamiltonians $H^{\pm}$ are intertwined by means of the operational relation

$$H^{+}L^{-} = L^{-}H^{-}, \tag{5.17}$$

with L^- being the intertwining operator given by

$$L^- = \frac{d}{dx} + w(x), \tag{5.18}$$

where $w(x)$ is a real function referred to as the superpotential. Within, the SUSY-QM framework, the partner potentials $V^\pm$ associated to the intertwined Hamiltonians $H^\pm$ can be written in terms of the superpotential function as follows

$$V^\pm = w^2(x) \pm w'(x). \tag{5.19}$$

Consequently, both Hamiltonians have an isospectral part and their eigenfunctions are linked through the supersymmetric transformation defined by the intertwining operator [254, 255, 256]. The SUSY algorithm has been successfully applied to solve the Dirac equation [257, 258], in particular, when this equation describes Dirac materials such as graphene [252, 259, 260, 261, 262, 263].

Defining the Schrödinger-like Hamiltonians

$$H_A^\pm = -\partial_x^2 + (k + A(x))^2 \pm \frac{dA(x)}{dx}, \tag{5.20a}$$

$$H_\phi^\pm = -\partial_z^2 + [i(\phi(z) + \varepsilon)]^2 \pm i\frac{d\phi(z)}{dz}, \tag{5.20b}$$

which are first-order supersymmetric partners, respectively, the corresponding SUSY transformations can be defined by the superpotentials

$$\mathrm{w}_A = k + A(x), \quad \mathrm{w}_\phi = i(\varepsilon + \phi(z)). \tag{5.21}$$

Thus, with the aid of the SUSY algorithm, the system of equations (5.16) can be written as

$$\left[H_A^- + H_\phi^\pm\right] \varphi_\uparrow^\pm = 0, \tag{5.22a}$$

$$\left[H_A^+ + H_\phi^\mp\right] \varphi_\downarrow^\pm = 0. \tag{5.22b}$$

Expressions above imply that we can construct solutions of the form

$$\varphi_\uparrow^\pm = \chi_\uparrow^-(x)\zeta_\uparrow^\pm(z), \quad \varphi_\downarrow^\pm = \chi_\downarrow^+(x)\zeta_\downarrow^\mp(z), \tag{5.23}$$

satisfying each one an eigenvalue equation of the form

$$H_A^\pm \chi_{\uparrow\downarrow}^\pm = \varepsilon_A \chi_{\uparrow\downarrow}^\pm, \quad H_\phi^\pm \zeta_{\uparrow\downarrow}^\pm = \varepsilon_\phi \zeta_{\uparrow\downarrow}^\pm. \tag{5.24}$$

Hence, we obtain a relation between the energies ε_A and ε_ϕ, given by

$$\varepsilon_A = -\varepsilon_\phi. \tag{5.25}$$

By solving the time-independent Schrödinger-like equations (5.24) such that the constraint in Eq. (5.25) is fulfilled, it is possible to determine the *spinor* Ψ_D satisfying the massless Dirac equation. It is worth mentioning the potentials $V_\phi^\pm(z)$ corresponding to the Hamiltonians in Eq. (5.20b) are complex. Since we are looking for real energy eigenvalues, care must be paid in the choice of the electromagnetic profiles. In the following section we discuss an example of electromagnetic fields which lead to solvable Schrödinger-like potentials. We explicitly explore their analytic solutions.

5.4 Confining case: Pöschl–Teller-like potentials

In order to determine the bound states of the Hamiltonians in Eq. (5.24), let us take electromagnetic potentials of the form

$$A(x) = \frac{B_0}{\nu}\sec(\nu x),\ -\frac{\pi}{2} < \nu x < \frac{\pi}{2};\ \phi(z) = \frac{E_0}{\mu}\text{sech}(\mu z). \tag{5.26}$$

In Fig. 5.1 we show the corresponding electric and magnetic fields produced by these potentials.

With the definitions above, from Eqs. (5.19) and (5.21), the SUSY partner potentials are

$$\begin{aligned} V_A^\pm(x) =& k^2 + 2kD_A\sec(\nu x) + D_A^2\sec^2(\nu x) \\ & \pm \nu D_A\sec(\nu x)\tan(\nu x), \end{aligned} \tag{5.27a}$$

$$\begin{aligned} V_\phi^\pm(z) =& -\varepsilon^2 - 2\varepsilon D_\phi\text{sech}(\mu z) - D_\phi^2\text{sech}^2(\mu z) \\ & \mp i\mu D_\phi\text{sech}(\mu z)\tanh(\mu z), \end{aligned} \tag{5.27b}$$

where $D_A = B_0/\nu$, $D_\phi = E_0/\mu$. Notice that the complex potentials in Eq. (5.27b), taking $\varepsilon = 0$, are particular cases of the so-called pseudo-Hermitian operators with real energy eigenvalues [264, 265]. It can be seen that both potentials have a similar form. Thus, we focus on getting the solutions of $V_\phi^\pm$; the potentials $V_A^\pm$ can be solved analogously. In Fig. 5.2, we plot the SUSY partner potentials in Eq. (5.27). In order to solve the eigenvalue equation of the Hamiltonians $H_\phi^\pm$, we perform the change of variable $u = i\sinh(\mu z)$, from which we obtain that

$$\begin{aligned} &\left[\mu^2(1-u^2)\frac{d^2}{du^2} - \mu^2 u\frac{d}{du} - \varepsilon^2 - 2\frac{\varepsilon D_\phi}{\sqrt{1-u^2}}\right. \\ &\left. -\frac{D_\phi^2}{1-u^2} \mp \mu D_\phi\frac{u}{1-u^2} - \varepsilon_\phi\right]\zeta^\pm(u) = 0. \end{aligned} \tag{5.28}$$

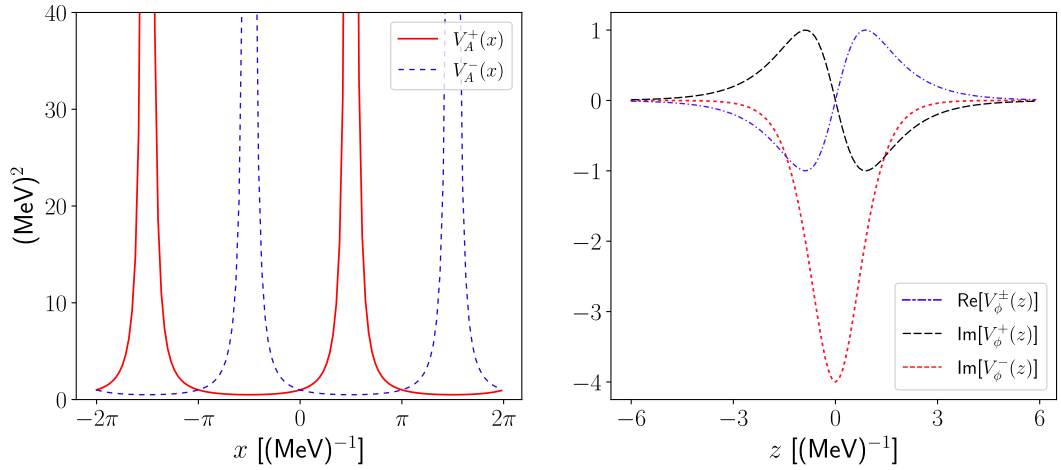

Figure 5.2: Plot of the Pösch–Teller-like SUSY partner potentials $V_A^\pm(x)$ (left). Real and imaginary parts of the potentials $V_\phi^\pm(z)$ (right). The scale of the graphs is set by parameters $E_0 = 2.0$, $B_0 = 1.0$, $\mu = 1.0$, $\nu = 1.0$ and $\varepsilon = k = 0$. Note that we are using natural units, $\hbar = c = e = 1$. Figure reproduced from Ref. [220].

Considering $\varepsilon = 0$, these differential equations lead to the Jacobi equation. We then propose the following ansatz for the functions $\zeta^\pm(u) = (1-u)^a(1+u)^b f^\pm(u)$. Thus, the differential equations (5.28) can be written as

$$\begin{aligned}\Bigg\{&(1-u^2)\frac{d^2}{du^2} + 2[b-a-(b+a+1/2)u]\frac{d}{du} - b(b-1) - a(a-1)\\ &- b - a - 2ab - \frac{\varepsilon_\phi}{\mu^2} + \left[2a(a-1) - 2b(b-1) - b + a \mp \frac{D_\phi}{\mu}\right]\frac{u}{1-u^2}\\ &+ \left[2b(b-1) + 2a(a-1) + b + a - \frac{D_\phi^2}{\mu^2}\right]\frac{1}{1-u^2}\Bigg\} f^\pm(u) = 0.\end{aligned} \tag{5.29}$$

Equation (5.29) accepts as solutions the Jacobi polynomials with complex argument $P_n^{(\alpha,\beta)}(u)$ as long as the following conditions are accomplished:

$$\begin{aligned} 2(b-a) &= \beta - \alpha,\\ 2(a+b+1/2) &= \alpha + \beta + 2,\\ -(b+a)^2 - \frac{\varepsilon_\phi}{\mu^2} &= n(n+\alpha+\beta+1),\\ (a-b)[2(a+b)-1] &= \pm S_\phi,\\ 2(a^2+b^2) - (a+b) &= S_\phi^2, \end{aligned} \tag{5.30}$$

with $S_\phi = D_\phi/\mu$. Once the above requirements fulfilled, the eigenfunctions of the Hamiltonians $H_\phi^\pm$ are given by

$$\begin{aligned}\zeta_n^\pm(u) =&(1-u)^{\frac{1}{4}\left(1-\sqrt{1+4S_\phi(S_\phi\pm1)}\right)}\times(1+u)^{\frac{1}{4}\left(1-\sqrt{1+4S_\phi(S_\phi\mp1)}\right)}\\ &\times P_n^{\left(-\frac{1}{2}\sqrt{1+4S_\phi(S_\phi\pm1)},-\frac{1}{2}\sqrt{1+4S_\phi(S_\phi\mp1)}\right)}(u).\end{aligned} \tag{5.31}$$

Boundary conditions imply that $|S_\phi| > 1$ and a finite discrete spectrum since the number of square-integrable functions is bounded by $Q_\phi - 1 \geq n$, where

$$Q_\phi = \frac{\sqrt{1+4S_\phi(S_\phi+1)}+\sqrt{1+4S_\phi(S_\phi-1)}}{2}.$$

It is worth-noticing that if S_ϕ is not an integer, the inequality is strict. Thus, $Q_\phi - 1$ is a upper value of the number of levels and it is necessary check the square-integrablility of each one of the eigenfunctions. Furthermore, the corresponding eigenvalues are

$$\varepsilon_\phi = -\mu^2\left[n(n-Q_\phi+1)+\frac{(1-Q_\phi)^2}{4}\right]. \tag{5.32}$$

On the other hand, as we mentioned earlier, when $k = 0$, the solutions of the Hamiltonians $H_A^\pm$ can be found by a similar process. Their corresponding eigenfunctions can be written as

$$\begin{aligned}\chi_m^\pm(u) =&(1-u)^{\frac{1}{4}\left(1+\sqrt{1+4S_A(S_A\pm1)}\right)}\times(1+u)^{\frac{1}{4}\left(1+\sqrt{1+4S_A(S_A\mp1)}\right)}\\ &\times P_m^{\left(\frac{1}{2}\sqrt{1+4S_A(S_A\pm1)},\frac{1}{2}\sqrt{1+4S_A(S_A\mp1)}\right)}(u),\end{aligned} \tag{5.33}$$

with $u = \sin(\nu x)$ and $S_A = D_A/\nu$, $m = 0, 1, 2, ...$ Boundary conditions are satisfied if $S_A(S_A \pm 1) > -1/4$. Moreover, the spectrum is infinite discrete, whilst the energy eigenvalues are given by

$$\varepsilon_A = \nu^2\left[m(m+Q_A+1)+\frac{(1+Q_A)^2}{4}\right], \tag{5.34}$$

where

$$Q_A = \frac{\sqrt{1+4S_A(S_A+1)}+\sqrt{1+4S_A(S_A-1)}}{2}.$$

The complete system, composed by both Hamiltonians including the magnetic and electric potentials (Eq.(5.22)), fulfills the relation for the energies $\epsilon_A = -\epsilon_\phi$ only when $n = m = 0$, resulting in the condition $\left|\frac{\nu}{\mu}\right| = \left|\frac{Q_\phi-(1+2n)}{Q_A+(1+2m)}\right|$, which relates both field strengths (B_0, E_0) and concentrations (μ, ν). Hence, we have a *spinor* $\Psi_{0,0}(x, z)$ with energy eigenvalue $\varepsilon = 0$ and wavenumber $k = 0$. To find solutions involving

non-zero energies and wavenumbers, the potentials in Eq. (5.27) should be solved in general, which is a highly nontrivial task. Finally, in terms of the functions $\chi_0^{\pm}(x)$ and $\zeta_0^{\pm}(z)$, the zero-mode *spinor* $\Psi_{0,0}(x,z)$ turns out to be

$$\Psi_{0,0}(x,z) = \frac{1}{2}\begin{pmatrix} \chi_0^-(x)\left[\zeta_0^+(z)+\zeta_0^-(z)\right] \\ \chi_0^+(x)\left[\zeta_0^-(z)-\zeta_0^+(z)\right] \\ \chi_0^-(x)\left[\zeta_0^+(z)-\zeta_0^-(z)\right] \\ \chi_0^+(x)\left[\zeta_0^+(z)+\zeta_0^-(z)\right] \end{pmatrix}. \tag{5.35}$$

In order to realize the fermion behavior of this zero-mode, we are interested in exploring the corresponding probability and current densities. Furthermore, the chiral-decomposition of the spinor above offers a natural form to understand its dynamics in this field configuration.

5.4.1 Probability and current densities

To obtain a visualization of the behavior of the particles in the system, we calculate the total probability density

$$\rho = |\Psi_D(t,x,y,z)|^2 = \Psi^\dagger(x,z)\Psi(x,z), \tag{5.36}$$

and the probability current densities given by

$$j_i = \Psi_D^\dagger(t,x,y,z)\alpha_i\Psi_D(t,x,y,z) = \Psi^\dagger(x,z)\alpha_i\Psi(x,z), \tag{5.37}$$

where $\alpha_i = 1,2,3$ are defined in Eq. (5.2). For the *spinor* in Eq. (5.13) these quantities have the following forms

$$\begin{aligned} \rho &= \frac{1}{2}\left[|\psi_\uparrow^\alpha|^2 + |\psi_\downarrow^\alpha|^2 + |\psi_\uparrow^\beta|^2 + |\psi_\downarrow^\beta|^2\right], \\ j_x &= \mathrm{Re}\left[\bar\psi_\uparrow^\alpha\psi_\downarrow^\alpha + \bar\psi_\uparrow^\beta\psi_\downarrow^\beta\right], \\ j_y &= \mathrm{Im}\left[\bar\psi_\uparrow^\alpha\psi_\downarrow^\alpha + \bar\psi_\uparrow^\beta\psi_\downarrow^\beta\right], \\ j_z &= \mathrm{Re}\left[\bar\psi_\uparrow^\alpha\psi_\uparrow^\beta - \bar\psi_\downarrow^\alpha\psi_\downarrow^\beta\right]. \end{aligned} \tag{5.38}$$

In order to have a better insight of the dynamics, let us look at the chiral decomposition of the *spinor*. For this purpose, we use the chiral projectors $P_{R,L} = \frac{1}{2}(I \pm \gamma_5)$, which allow us to obtain the left- (L) and right-handed (R) *spinors*

$$\Psi_{D;R,L}(t,x,y,z) = e^{i(\varepsilon t+ky)}\Psi_{R,L}(x,z) = \frac{1}{2}e^{i(\varepsilon t+ky)}\begin{pmatrix} \psi_\uparrow^\alpha \pm \psi_\uparrow^\beta \\ \psi_\downarrow^\beta \pm \psi_\downarrow^\alpha \\ \psi_\uparrow^\beta \pm \psi_\uparrow^\alpha \\ \psi_\downarrow^\alpha \pm \psi_\downarrow^\beta \end{pmatrix}, \tag{5.39}$$

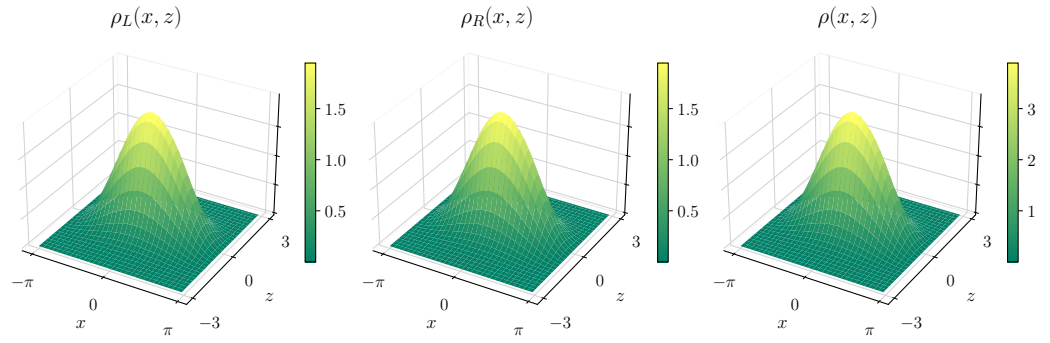

Figure 5.3: Probability densities for the L- and R-handed *spinors* in Eq. (5.39) (first and second column, respectively) and total probability density (third column), corresponding to the zero-mode *spinor* in Eq. (5.35). The scale of the plot is set by the parameters $E_0 = 2.0$, $B_0 = 1.0$, $\mu = 1.0$ and $\nu = 1.0$. Note that we are using natural units, $\hbar = c = e = 1$, where x, y, z variables possess units of $(\text{MeV})^{-1}$, whereas the probability density has units of $(\text{MeV})^3$. Figure reproduced from Ref. [220].

where the down-sign (up-sign) is chosen for the L(R)-handed *spinor*. Note that in Eq. (5.39) we are suppressing the x- and z-dependence of the *spinor* components to simplify the notation. Chiral projections of the probability density (shown in Fig. 5.3) are

$$\rho_{R,L} = \frac{1}{2}\left[|\psi_{\uparrow}^{\alpha}|^2 + |\psi_{\downarrow}^{\alpha}|^2 + |\psi_{\uparrow}^{\beta}|^2 + |\psi_{\downarrow}^{\beta}|^2\right] \pm \text{Re}\left[\psi^{*\alpha}_{\uparrow}\psi^{\beta}_{\uparrow} + \psi^{*\alpha}_{\downarrow}\psi^{\beta}_{\downarrow}\right]. \tag{5.40}$$

On the other hand, the current densities (see Fig. 5.4)

$$j_{x;R,L} = \text{Re}\left[\psi^{*\alpha}_{\uparrow}\left(\psi^{\alpha}_{\downarrow} \pm \psi^{\beta}_{\downarrow}\right) + \psi^{*\beta}_{\uparrow}\left(\psi^{\beta}_{\downarrow} \pm \psi^{\alpha}_{\downarrow}\right)\right], \tag{5.41}$$

$$j_{y;R,L} = \text{Im}\left[\psi^{*\alpha}_{\uparrow}\left(\psi^{\alpha}_{\downarrow} \pm \psi^{\beta}_{\downarrow}\right) + \psi^{*\beta}_{\uparrow}\left(\psi^{\beta}_{\downarrow} \pm \psi^{\alpha}_{\downarrow}\right)\right], \tag{5.42}$$

$$j_{z;R,L} = \text{Re}\left[\psi^{*\alpha}_{\uparrow}\psi^{\beta}_{\uparrow} - \psi^{*\alpha}_{\downarrow}\psi^{\beta}_{\downarrow}\right] \pm \frac{1}{2}\left[|\psi^{\alpha}_{\uparrow}|^2 + |\psi^{\beta}_{\uparrow}|^2 - |\psi^{\alpha}_{\downarrow}|^2 - |\psi^{\beta}_{\downarrow}|^2\right]. \tag{5.43}$$

As can be seen from Fig. 5.3, for the zero-mode *spinor* in Eq. (5.35), the probability density is almost entirely localized around the origin, and both L- and R-handed components of the spinor contribute to the total probability density, which is the sum of both handed components, in the same quantity, *i.e.*, there is no chiral charge imbalance. We must mention, a chiral (axial) current density $\mathbf{J}_5$ could be defined [266, 267]. However, for such current density, the standard continuity equation becomes tremendously more involved due to the non-uniformity of the electromagnetic fields proposed in this work. Moreover, a straightforward calculation verifies that

the total current densities in Eq. (5.38) are the sum of the respective L- and R-handed currents, i.e., $j_i = j_{i;R} + j_{i;L}$. From Fig. 5.4, we can observe that the L- and R-handed components of the $x-$ and $z-$current densities cancel out (they are opposite), whereas in the $y-$direction, they are exactly the same so that the sum is non-vanishing.

It is standard to represent the R-handed chirality (η^+) as a counter-clockwise motion, while L-handed chirality (η^-) is sketched as a clockwise motion. This picture is very useful to gain insight into the behavior of the particles, see Fig. 5.5, where we can possible observe that the L- and R-handed currents sum up in the $y-$direction and cancel out in other directions. This observation that the non-vanishing current density along the y-axis is perpendicular to the magnetic and electric fields, which point out in z-direction, is not due to the straight action of the electric field, but rather a consequence of the presence of both fields. Hence, we can observe an Hall-like Effect. However, the current density along the y-direction and the electromagnetic fields define a the plane where they all lie. Then, through our set up we describe a particular case of the Planar Hall Effect (PHE). Furthermore, in our case the electromagnetic fields are non-uniform (see Fig. 5.2), which causes slight differences respect to the standard case where uniform fields are considered [247]. Actually, the inhomogeneous feature of the electromagnetic fields is responsible of the behavior of the particles in the system. Therefore, the current density defining the PHE is a consequence of the chiral symmetry, which is preserved due to the supersymmetry thereof. We must mention, in the context of Dirac materials, chiral symmetry is translated as the valley symmetry, thus, it is also valid to discuss the dynamics in terms of a valley PHE for the system addressed here. It is important to note that these results are not general but exclusive to this example, since the particular profiles and directions of the external fields coupled with the particle's chirality are the responsible of cancellation or addition of currents in particular directions. Even thought, a prospect application could be the current steering through a Type-I Weyl semimetal, which, as discussed briefly in the conclusions, is of solitonic nature. In other words, a non-dissipating wave guide can be accomplished by means of external nonhomogeneous parallel electromagnetic fields.

5.5 Discussion and Conclusions

In this Chapter, the (3+1) Dirac equation describing a Dirac material in the presence of static non-uniform parallel electromagnetic fields is solved within a SUSY-QM framework. In order to determine an exact analytic solution, we address the example of electromagnetic profiles leading to Pöschl–Teller-like quantum potentials. The corresponding zero-mode *spinor* is found and its associated probability and current densities obtained. We notice that the current densities vanish in all spatial direc-

tions, except for the current along the y-direction, which defines a plane in which it lies perpendicularly to the electromagnetic fields. Hence, it is appropriate to assume that a PHE develops in the system dealt here. Furthermore, since the current densities turn out to be written in terms of the left- and right-handed current densities, the effect can be regarded as driven by the chiral symmetry of the system. A chiral-dependent PHE has been shown in inhomogeneous type-I Weyl semimetals [266]. However, the Dirac material addressed in this Chapter is pristine but under non-uniform external electromagnetic fields. Therefore, this material shows a new class of chiral PHE. We must mention that the electromagnetic profiles in Eq. (5.26) are tough to realize in the laboratory. Nevertheless, a configuration of pseudo-electromagnetic fields, associated to strains in the material, could become analogous to the system worked here. Such configuration could be feasible in the laboratory through modern strain techniques in Dirac materials, such as scanning tuneling spectroscopy [268, 269]. It is worth noticing that the considered electromagnetic profiles are setting up two uncoupled Jackiw-Rebbi (J-R) models for the dynamics along in each direction [214, 270, 271]. This observation can be seen precisely in Fig. 5.1. Hence, the system naturally is divided into two regions, for $z > 0$, the current density along the y-direction points out in the positive direction; while, for $z < 0$, it points out in the negative direction. Then, it is sufficient to observe only one of these regions. Focusing on the upper region, the localization of the current density at hand (see Fig. 5.4) allows us to draw an imaginary cylinder containing the current in its upper half, as depicted in Fig. 5.5. We further remark the localization of the probability density as shown in Fig. 5.3. Thus, the wave packet we are considering in this work should be regarded as a two-dimensional soliton of the J-R type. Therefore, our system could be a promising artificial set up of a wave guide with no energy losses, which could be technologically superb.

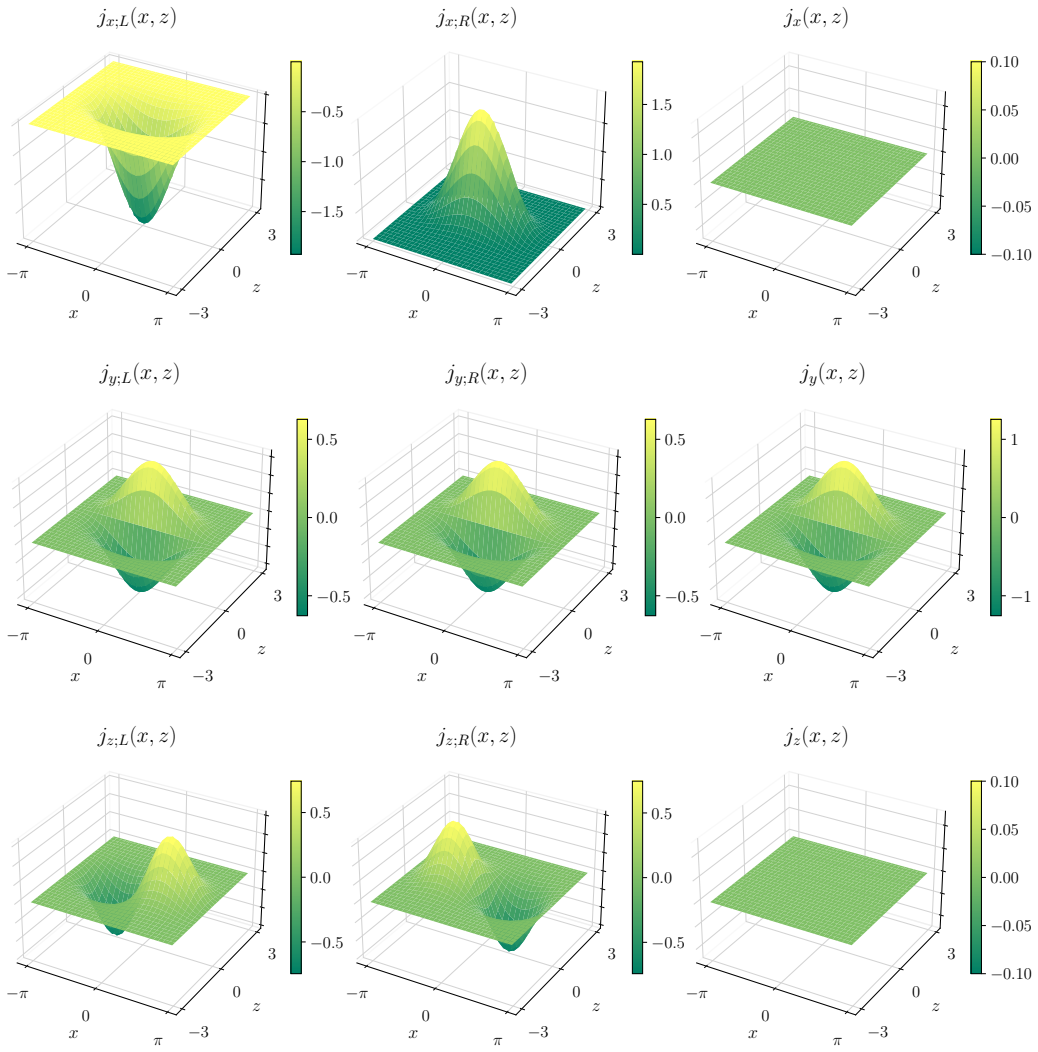

Figure 5.4: R- and L-handed probability current densities (first and second column, respectively) and total probability current densities (third column) for the *spinors* in Eq. (5.39) corresponding to the zero-mode of the system. In x- and z-directions the R- and L-handed components are exactly equal but with opposite sign, resulting in null-total current densities. While, in y-direction both components contribute to the non-zero current density. The parameter values taken are $E_0 = 2.0$, $B_0 = 1.0$, $\mu = 1.0$ and $\nu = 1.0$. Note that we are using natural units, $\hbar = c = e = 1$, where x, y, z variables possess units of $(\text{MeV})^{-1}$, whereas the probability current densities has units of $(\text{MeV})^3$. Figure reproduced from Ref. [220].

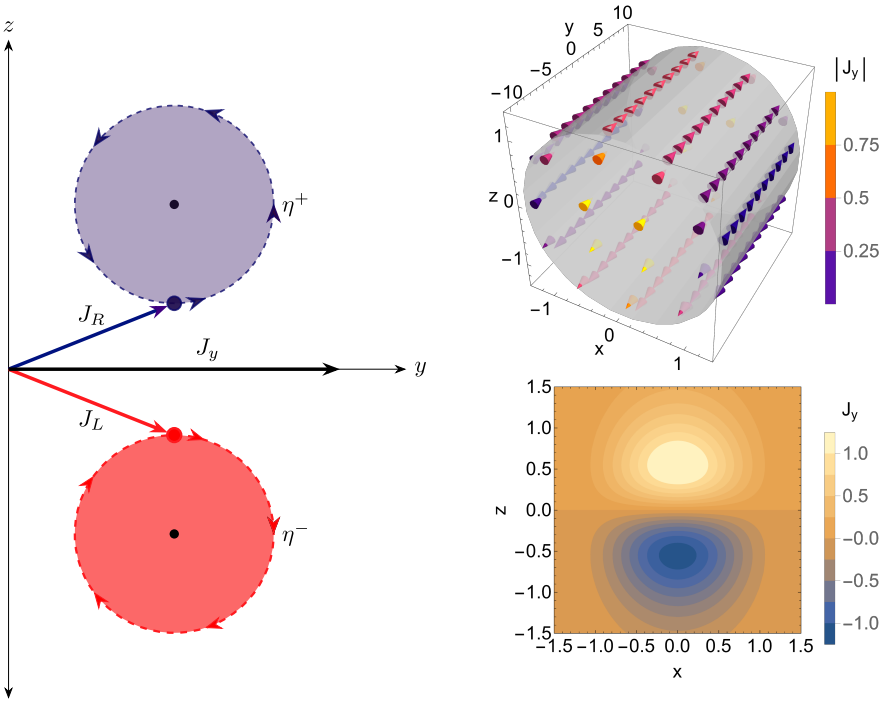

Figure 5.5: (Left) A representation of the Right and Left chiralities. The sum of the corresponding L- and R-handed currents is non-zero in y-direction. (Right-top) j_y current on the surface of a cylinder and (Right-bottom) its projection to the $x-z$ plane. It can be seen the direction switching through passing the $z=0$ plane. Note that we are using natural units, $\hbar = c = e = 1$, where x, y, z variables possess units of $(\text{MeV})^{-1}$, whereas the probability current densities has units of $(\text{MeV})^3$. Figure reproduced from Ref. [220].

Supplements

5.A SUSY QM

In non-relativistic quantum mechanics (NR-QM), the number of analytically solvable problems is minor. In order to be able to raise that statistics, a number of mathematical techniques have been developed, some of them based in factorization methods [272]. In 1981, Witten established the possibility to present the Schrödinger Hamiltonian in a form of supersymmetric partners [219]. This technique developed by Witten had a great impact in the study of exactly solvable Hamiltonians, and was named *supersymmetric quantum mechanics* (SUSY-QM). Actually, nowadays the SUSY-QM technique has also been used to solve relativistic QM problems and related problems, such as the graphene spectrum.

In general, the SUSY-QM technique consists in the definition of a superalgebra followed by a pair of supercharges and a Hamiltonian [219]. In this sense, it is possible to find different differential operators which intertwines two Hamiltonians and at the same time factorize them [273, 274]. Of notable importance is the problem of the quantum Harmonic Oscillator, which can be exactly solved by means of this technique, and is relevant in almost all (if not in all) fields physics, and even in mathematics. Next we present the general mathematical formulation of the first-order SUSY-QM method, including the Witten definition based on supercharges.

5.A.1 Witten definition

In the Witten definition, the called $N = 2$ SUSY-QM consists of two supercharges Q_1 and Q_2, and a Hamiltonian obeying the relations

$$\{Q_1, Q_2\} = 0,\ H = 2Q_1^2 = 2Q_2^2 = Q_1^2 + Q_1^2.$$

Let us introduce the complex supercharges

$$Q = \frac{1}{\sqrt{2}}\left(Q_1 + iQ_2\right),\ Q^\dagger = \frac{1}{\sqrt{2}}\left(Q_1 - iQ_2\right).$$

These operator together with H close the superalgebra

$$Q^2 = 0 = \left(Q^\dagger\right)^2,\ \left\{Q, Q^\dagger\right\} = H. \tag{5.44}$$

This superalgebra completely defines SUSY-QM in an abstract form, and implies

$$[H, Q] = 0 = \left[H, Q^\dagger\right]. \tag{5.45}$$

In Fig. 5.6 we present typical energy spectra of two intertwined Hamiltonians. As it can be seen, in some cases (unbroken SUSY) both spectra are equal, whereas in other cases (broken) the spectrum generated by the intertwined Hamiltonian losses its ground state.

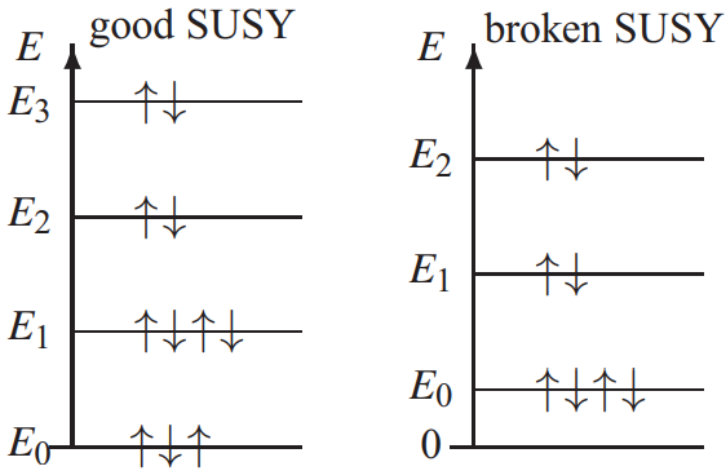

Figure 5.6: Typical spectra for unbroken ($E_0 = 0$) and broken ($E_0 > 0$) SUSY. Adapted from [275].

5.A.2 Mathematical formulation

Let us consider two Schrödinger Hamiltonians

$$H_i = -\frac{1}{2}\frac{d^2}{dx^2} + V_i(x),\ i = 0, 1, ..., \tag{5.46}$$

and let suppose the existence of a first order differential operator

$$a^\dagger = \frac{1}{\sqrt{2}}\left(-\frac{d}{dx} + W(x)\right), \tag{5.47}$$

with $W(x)$ a real function to be determined, called superpotential. Suppose that this differential operator intertwines both Hamiltonians

$$H_1 a^\dagger = a^\dagger H_0. \tag{5.48}$$

Let us compute each side of the last equation:

$$\begin{aligned} H_1 a^\dagger =& \left[-\frac{1}{2}\frac{d^2}{dx^2} + V_1(x)\right]\left[\frac{1}{\sqrt{2}}\left(-\frac{d}{dx} + W(x)\right)\right] \\ =& \frac{1}{\sqrt{2}}\left[\frac{1}{2}\frac{d^3}{dx^3} - \frac{W}{2}\frac{d^2}{dx^2} - \left(V_1 + W'\right)\frac{d}{dx} + WV_1 - \frac{W''}{2}\right], \end{aligned} \tag{5.49}$$

$$a^\dagger H_0 = \left[\frac{1}{\sqrt{2}}\left(-\frac{d}{dx}+W(x)\right)\right]\left[-\frac{1}{2}\frac{d^2}{dx^2}+V_0(x)\right]$$
$$=\frac{1}{\sqrt{2}}\left[\frac{1}{2}\frac{d^3}{dx^3}-\frac{W}{2}\frac{d^2}{dx^2}-V_0\frac{d}{dx}+WV_0-V_0'\right]. \quad (5.50)$$

Since all the coefficients of the same powers of $\frac{d}{dx}$ must be equal, we have

$$V_1 = V_0 - W', \quad (5.51)$$

$$WV_1 - \frac{W''}{2} = WV_0 - V_0'. \quad (5.52)$$

Substituting (5.51) in (5.52), and integrating

$$W^2 + W' = 2(V_0 - \epsilon), \quad (5.53)$$

where ϵ is a constant called *factorization energy*. Equations (5.51)-(5.53) guarantee the factorization of the Hamiltonians in the form

$$H_0 = aa^\dagger + \epsilon,\ H_1 = a^\dagger a + \epsilon, \quad (5.54)$$

where

$$a = \left(a^\dagger\right)^\dagger = \frac{1}{\sqrt{2}}\left(\frac{d}{dx}+W(x)\right). \quad (5.55)$$

If V_0 is a solvable potential with eigenfunctions $\psi_n^{(0)}(x)$ and eigenvalues E_n, $n = 0, 1, ...$, and also we know the solution $u_1^{(0)}(x)$ to the Ricatti equation (Eq.(5.53)), for a given value of the factorization energy $\epsilon = \epsilon_1 \leq E_0$, thus the $V_1(x)$ potential is also solvable with eigenfunctions

$$\psi_{\epsilon_1}^{(1)}(x)\ \alpha\ e^{-\int_0^x W(y,\epsilon)dy} = \frac{1}{u_1^{(0)}(x)}, \quad (5.56)$$

$$\psi_{\epsilon_1}^{(1)}(x) = \frac{a^\dagger \psi_n^{(0)}(x)}{\sqrt{E_n - \epsilon_1}}, \quad (5.57)$$

and with eigenvalues $\{\epsilon_1, E_n,\ n = 0, 1, ...\}$. Here, we have selected to work with factorization energies lower than the base state of H_0 to avoid singularities in $W(x)$, $V_1(x)$ and also in the eigenfunctions.

Chapter 6

General Discussion and Conclusions

The need of classifying materials according to particular properties is of great importance in Condensed Matter Physics. In this sense, different classifications have been proposed, ranging from the well-known band theory in which the electronic properties are result of the characteristics of the valence and conduction bands, to even more paradigmatic classifications such as the one proposed by Landau based on the principle of spontaneous symmetry breaking and local order parameters. The former, *i.e.* has been widely studied in conventional (Schrödinger) materials, being able to precisely explain the properties of metals, insulators and semiconductors. In these conventional systems governed by a Schrödinger Hamiltonian, the energy-momentum spectra present parabolic behaviour. Another novel type of materials was discovered in 2005 (even though theoretically proposed much before), when a two-dimensional honeycomb lattice of carbon atoms with only one atom thick (graphene) was synthesized, presenting a linear low-energy spectrum near two nodes (Dirac points). These new kind of materials continued growing with the discovery of topological insulators and more recently with the discovery of three-dimensional Dirac and Weyl semimetals. The common denominators of all these materials are the linear low-energy spectrum and the appearance of nodes in the First Brillouin Zone protected by a symmetry. These materials were named as Dirac materials, as they can be effectively described by a Dirac equation through the replacement $c \to v_{\mathrm{F}}$.

Dirac materials have different microscopic origins, such as the presence of sublattice structure in graphene, spin-orbit angular momentum coupling in topological insulators, chiral energy bands in Dirac and Weyl semimetals, among others. However, regardless of the origin, all Dirac materials present universal properties, such as thermodynamic behaviour, fermion coupling with external magnetic fields, sup-

pression of backscattering, and even many-body collective effects such as plasmons, excitons and superconductivity. These universal properties in Dirac materials are again given by the Dirac spectrum and by the existence of protected nodes in the FBZ.

Effects of external and internal perturbations in Dirac systems are of great interest due to the possibility of tune electronic, mechanical, optical, etc., properties with the aim of possible technological applications or study of the robustness of some properties under perturbations (topological properties). In fact, extremely interesting phenomena have been pointed out for example while Dirac fermions interact with external magnetic fields (for example the Landau levels spectrum in graphene and the chiral magnetic effect in Weyl semimetals), and both electric and magnetic fields (various types of quantum Hall effects in graphene, or the anomalous Hall effect and planar Hall effect in Weyl semimetals). Also, effects of atom substitution or impurity placement have an important role in systems such as graphene (tuning electrical and conductivity, or the more dramatic atomic collapse effect), and topological insulators (tuning topological conditions and localization). In addition, some other interesting effects in Dirac materials can be accomplished by pseudomagnetic potentials, that is, strain on the lattice.

In this thesis we have treated three different problems of Dirac materials under perturbations: First, we have studied the problem of a 1D topological insulator, the SSH model, with the presence of impurity atoms present in different superlattice structures. In this case, studies were developed using both tight-binding and topolectrical circuits theories. The general result of this study was the evidence for the possibility of tuning the topological condition, that is the Berry phase, in order to present a topologically trivial/non-trivial behaviour of the material. Also, the existence of these impurity superlattices inhibit or promotes the edge state localization of the wave functions, depending on the way hopping amplitudes are defined. In conclusion, impurities in the SSH model are able to tune topological properties of the system. In second place, we have tackled the non-relativistic representation of the JR soliton through a Foldy-Wouthuysen (FW) unitary transformation. As a general conclusion of this work, we argue that the zero-mode energy of the JR model, which turns out to be non-dissipative with a *kink* profile, is preserved under the FW transformation presented, which represents the non-relativistic representation of the original one, disconnecting the particle and hole parts of the relativistic spinor. Finally, we have considered the case of Weyl semimetals under the effect of parallel non-uniform electromagnetic fields generated by SUSY-QM. In this work we have established that the effect of parallel non-uniform electromagnetic fields such as the ones we used plays the role of generating (chiral) inhomogeneity inside the material, resulting in a planar Hall effect whose origin comes from the chirality of

the particles (in this case the chirality is also related with SUSY). Also, the fields setting resembles a JR problem in two directions, promoting a solitonic solution in the other direction, being thus potentially used as a wave guide with no energy losses.

As a general conclusion, internal and external perturbations over Dirac systems (materials) result in a plethora of novel interesting phenomena, and the broad understanding of the mechanisms responsible of promoting these effects could lead us to an effective manipulation of these materials with potential application in new technologies and scientific development.

Chapter 7

Future Work

In addition to the work presented in this thesis, we have started the study of other effects of perturbations in Dirac systems. That is the case of the Dirac equation in curved spaces describing deformations in Dirac materials, thermodynamic properties of periodic Dirac systems and effects of impurities in Dirac transport properties of Dirac materials. In the future I would also like to study the effect of quantum anomalies in Dirac systems, as well as material junctions and amorphous systems.

Bibliography

[1] Kostya S Novoselov et al. "Electric field effect in atomically thin carbon films". In: *science* 306.5696 (2004), pp. 666–669.

[2] Grigory E Volovik. *Exotic properties of superfluid 3He*. Vol. 1. World Scientific, 1992.

[3] Dieter Vollhardt and Peter Wolfle. *The superfluid phases of helium 3*. Courier Corporation, 2013.

[4] Alexander V Balatsky, Ilya Vekhter, and Jian-Xin Zhu. "Impurity-induced states in conventional and unconventional superconductors". In: *Reviews of Modern Physics* 78.2 (2006), p. 373.

[5] M Zahid Hasan and Charles L Kane. "Colloquium: topological insulators". In: *Reviews of modern physics* 82.4 (2010), p. 3045.

[6] Xiao-Liang Qi and Shou-Cheng Zhang. "Topological insulators and superconductors". In: *Reviews of Modern Physics* 83.4 (2011), p. 1057.

[7] Xiangang Wan et al. "Topological semimetal and Fermi-arc surface states in the electronic structure of pyrochlore iridates". In: *Physical Review B* 83.20 (2011), p. 205101.

[8] Steve M Young et al. "Dirac semimetal in three dimensions". In: *Physical review letters* 108.14 (2012), p. 140405.

[9] S Das Sarma et al. "Electronic transport in two-dimensional graphene". In: *Reviews of modern physics* 83.2 (2011), p. 407.

[10] Andre Konstantin Geim. "Graphene: status and prospects". In: *science* 324.5934 (2009), pp. 1530–1534.

[11] Wei Han et al. "Graphene spintronics". In: *Nature nanotechnology* 9.10 (2014), pp. 794–807.

[12] John R Schaibley et al. "Valleytronics in 2D materials". In: *Nature Reviews Materials* 1.11 (2016), pp. 1–15.

[13] Ya-Ning Ren et al. "Twistronics in graphene-based van der Waals structures". In: *Chinese Physics B* 29.11 (2020), p. 117303.

[14] Mohammad A Rafiee et al. "Enhanced mechanical properties of nanocomposites at low graphene content". In: *ACS nano* 3.12 (2009), pp. 3884–3890.

[15] Xiaochang Miao et al. "High efficiency graphene solar cells by chemical doping". In: *Nano letters* 12.6 (2012), pp. 2745–2750.

[16] Xiaojun Cheng et al. "Robust reconfigurable electromagnetic pathways within a photonic topological insulator". In: *Nature materials* 15.5 (2016), pp. 542–548.

[17] Lei Wang, Matthias Troyer, and Xi Dai. "Topological charge pumping in a one-dimensional optical lattice". In: *Physical review letters* 111.2 (2013), p. 026802.

[18] Sandeep Pathak, Vijay B Shenoy, and G Baskaran. "Possible high-temperature superconducting state with a d+ i d pairing symmetry in doped graphene". In: *Physical Review B* 81.8 (2010), p. 085431.

[19] Mikhail Iosifovich Katsnelson, Konstantin Sergejevič Novoselov, and Andre Konstantin Geim. "Chiral tunnelling and the Klein paradox in graphene". In: *Nature physics* 2.9 (2006), pp. 620–625.

[20] MI Katsnelson. "Zitterbewegung, chirality, and minimal conductivity in graphene". In: *The European Physical Journal B-Condensed Matter and Complex Systems* 51 (2006), pp. 157–160.

[21] F Guinea, AH Castro Neto, and NMR Peres. "Electronic states and Landau levels in graphene stacks". In: *Physical Review B* 73.24 (2006), p. 245426.

[22] Julio César Pérez-Pedraza et al. "Critical behavior for point monopole and dipole electric impurities in uniformly and uniaxially strained graphene". In: *Physical Review B* 102.4 (2020), p. 045131.

[23] Gerardo G Naumis et al. "Electronic and optical properties of strained graphene and other strained 2D materials: a review". In: *Reports on Progress in Physics* 80.9 (2017), p. 096501.

[24] Alberto Cortijo et al. "Strain-induced chiral magnetic effect in Weyl semimetals". In: *Physical Review B* 94.24 (2016), p. 241405.

[25] FC Chen et al. "Planar Hall effect in the type-II Weyl semimetal T d- MoT e 2". In: *Physical Review B* 98.4 (2018), p. 041114.

[26] S Nandy et al. "Chiral anomaly as the origin of the planar Hall effect in Weyl semimetals". In: *Physical review letters* 119.17 (2017), p. 176804.

[27] AA Zyuzin and AA Burkov. "Topological response in Weyl semimetals and the chiral anomaly". In: *Physical Review B* 86.11 (2012), p. 115133.

[28] Castro Neto et al. "Rev. Mod. Phys. 81, 109–162 (2009)". In: *Rev. Mod. Phys* 81 (2009), pp. 109–162.

[29] Mikhail I Katsnelson. "Graphene: carbon in two dimensions". In: *Materials today* 10.1-2 (2007), pp. 20–27.

[30] Yuanbo Zhang et al. "Experimental observation of the quantum Hall effect and Berry's phase in graphene". In: *nature* 438.7065 (2005), pp. 201–204.

[31] Seymur Cahangirov et al. "Two-and one-dimensional honeycomb structures of silicon and germanium". In: *Physical review letters* 102.23 (2009), p. 236804.

[32] Kyozaburo Takeda and Kenji Shiraishi. "Theoretical possibility of stage corrugation in Si and Ge analogs of graphite". In: *Physical Review B* 50.20 (1994), p. 14916.

[33] Parvis Soltan-Panahi et al. "Multi-component quantum gases in spin-dependent hexagonal lattices". In: *Nature Physics* 7.5 (2011), pp. 434–440.

[34] Leticia Tarruell et al. "Creating, moving and merging Dirac points with a Fermi gas in a tunable honeycomb lattice". In: *Nature* 483.7389 (2012), pp. 302–305.

[35] Marco Gibertini et al. "Engineering artificial graphene in a two-dimensional electron gas". In: *Physical Review B* 79.24 (2009), p. 241406.

[36] Kenjiro K Gomes et al. "Designer Dirac fermions and topological phases in molecular graphene". In: *Nature* 483.7389 (2012), pp. 306–310.

[37] Marco Polini et al. "Artificial honeycomb lattices for electrons, atoms and photons". In: *Nature nanotechnology* 8.9 (2013), pp. 625–633.

[38] Cheol-Hwan Park et al. "New generation of massless Dirac fermions in graphene under external periodic potentials". In: *Physical review letters* 101.12 (2008), p. 126804.

[39] F Guinea and Tony Low. "Band structure and gaps of triangular graphene superlattices". In: *Philosophical Transactions of the Royal Society A: Mathematical, Physical and Engineering Sciences* 368.1932 (2010), pp. 5391–5402.

[40] Carmine Ortix, Liping Yang, and Jeroen van den Brink. "Graphene on incommensurate substrates: Trigonal warping and emerging Dirac cone replicas with halved group velocity". In: *Physical Review B* 86.8 (2012), p. 081405.

[41] LA Ponomarenko et al. "Cloning of Dirac fermions in graphene superlattices". In: *Nature* 497.7451 (2013), pp. 594–597.

[42] Boris A Volkov and Oleg A Pankratov. "Two-dimensional massless electrons in an inverted contact". In: *Soviet Journal of Experimental and Theoretical Physics Letters* 42 (1985), p. 178.

[43] Eduardo Fradkin, Elbio Dagotto, and Daniel Boyanovsky. "Physical realization of the parity anomaly in condensed matter physics". In: *Physical review letters* 57.23 (1986), p. 2967.

[44] OA Pankratov, SV Pakhomov, and BA Volkov. "Supersymmetry in heterojunctions: Band-inverting contact on the basis of $Pb_{1-x}Sn_xTe$ and $Hg_{1-x}Cd_xTe$". In: *Solid state communications* 61.2 (1987), pp. 93–96.

[45] B Andrei Bernevig, Taylor L Hughes, and Shou-Cheng Zhang. "Quantum spin Hall effect and topological phase transition in HgTe quantum wells". In: *science* 314.5806 (2006), pp. 1757–1761.

[46] Yoichi Ando. "Topological insulator materials". In: *Journal of the Physical Society of Japan* 82.10 (2013), p. 102001.

[47] Liang Fu, Charles L Kane, and Eugene J Mele. "Topological insulators in three dimensions". In: *Physical review letters* 98.10 (2007), p. 106803.

[48] Liang Fu. "Topological crystalline insulators". In: *Physical review letters* 106.10 (2011), p. 106802.

[49] Timothy H Hsieh et al. "Topological crystalline insulators in the SnTe material class". In: *Nature communications* 3.1 (2012), p. 982.

[50] CC Tsuei and JR Kirtley. "Pairing symmetry in cuprate superconductors". In: *Reviews of Modern Physics* 72.4 (2000), p. 969.

[51] Joe D. Thompson and Zachary Fisk. "Progress in heavy-fermion superconductivity: Ce115 and related materials". In: *Journal of the Physical Society of Japan* 81.1 (2011), p. 011002.

[52] ZK Liu et al. "Discovery of a three-dimensional topological Dirac semimetal, Na3Bi". In: *Science* 343.6173 (2014), pp. 864–867.

[53] Sergey Borisenko et al. "Experimental realization of a three-dimensional Dirac semimetal". In: *Physical review letters* 113.2 (2014), p. 027603.

[54] Madhab Neupane et al. "Observation of a topological 3D Dirac semimetal phase in high-mobility Cd3As2". In: *arXiv preprint arXiv:1309.7892* (2013).

[55] Tim O Wehling, Annica M Black-Schaffer, and Alexander V Balatsky. "Dirac materials". In: *Advances in Physics* 63.1 (2014), p. 1.

[56] Qin Liu et al. "Magnetic impurities on the surface of a topological insulator". In: *Physical review letters* 102.15 (2009), p. 156603.

[57] Philip Richard Wallace. "The band theory of graphite". In: *Physical review* 71.9 (1947), p. 622.

[58] P Ghosh and P Roy. "Collapse of Landau levels in graphene under uniaxial strain". In: *Materials Research Express* 6.12 (2019), p. 125603.

[59] Julio C. Pérez-Pedraza. *Induced bound states by monopole and point dipole electric impurities in strained graphene*. UMSNH, 2020.

[60] Gordon W Semenoff. "Condensed-matter simulation of a three-dimensional anomaly". In: *Physical Review Letters* 53.26 (1984), p. 2449.

[61] Matthew Mecklenburg and BC Regan. "Spin and the honeycomb lattice: lessons from graphene". In: *Physical review letters* 106.11 (2011), p. 116803.

[62] Juan L Mañes, Francisco Guinea, and María AH Vozmediano. "Existence and topological stability of Fermi points in multilayered graphene". In: *Physical Review B* 75.15 (2007), p. 155424.

[63] F Duncan M Haldane. "Model for a quantum Hall effect without Landau levels: Condensed-matter realization of the" parity anomaly"". In: *Physical review letters* 61.18 (1988), p. 2015.

[64] S Yi Zhou et al. "Substrate-induced bandgap opening in epitaxial graphene". In: *Nature materials* 6.10 (2007), pp. 770–775.

[65] G Dresselhaus and Mildred S Dresselhaus. "Spin-orbit interaction in graphite". In: *Physical Review* 140.1A (1965), A401.

[66] Charles L Kane and Eugene J Mele. "Quantum spin Hall effect in graphene". In: *Physical review letters* 95.22 (2005), p. 226801.

[67] Hongki Min et al. "Intrinsic and Rashba spin-orbit interactions in graphene sheets". In: *Physical Review B* 74.16 (2006), p. 165310.

[68] Valeri N Kotov et al. "Electron-electron interactions in graphene: Current status and perspectives". In: *Reviews of modern physics* 84.3 (2012), p. 1067.

[69] Chang-Yu Hou, Claudio Chamon, and Christopher Mudry. "Electron fractionalization in two-dimensional graphenelike structures". In: *Physical review letters* 98.18 (2007), p. 186809.

[70] Yasumasa Hasegawa et al. "Zero modes of tight-binding electrons on the honeycomb lattice". In: *Physical Review B* 74.3 (2006), p. 033413.

[71] Petra Dietl, Frédéric Piéchon, and Gilles Montambaux. "New magnetic field dependence of Landau levels in a graphenelike structure". In: *Physical review letters* 100.23 (2008), p. 236405.

[72] Shun-Qing Shen. *Topological insulators*. Vol. 174. Springer, 2012.

[73] David J Thouless et al. "Quantized Hall conductance in a two-dimensional periodic potential". In: *Physical review letters* 49.6 (1982), p. 405.

[74] Xiao-Gang Wen. "Topological orders and edge excitations in fractional quantum Hall states". In: *Advances in Physics* 44.5 (1995), pp. 405–473.

[75] Charles L Kane and Eugene J Mele. "Z 2 topological order and the quantum spin Hall effect". In: *Physical review letters* 95.14 (2005), p. 146802.

[76] Joel E Moore and Leon Balents. "Topological invariants of time-reversal-invariant band structures". In: *Physical Review B* 75.12 (2007), p. 121306.

[77] Xiao-Liang Qi, Taylor L Hughes, and Shou-Cheng Zhang. "Topological field theory of time-reversal invariant insulators". In: *Physical Review B* 78.19 (2008), p. 195424.

[78] David Hsieh et al. "A topological Dirac insulator in a quantum spin Hall phase". In: *Nature* 452.7190 (2008), pp. 970–974.

[79] Haijun Zhang et al. "Topological insulators in Bi2Se3, Bi2Te3 and Sb2Te3 with a single Dirac cone on the surface". In: *Nature physics* 5.6 (2009), pp. 438–442.

[80] Yuqi Xia et al. "Observation of a large-gap topological-insulator class with a single Dirac cone on the surface". In: *Nature physics* 5.6 (2009), pp. 398–402.

[81] YL Chen et al. "Experimental realization of a three-dimensional topological insulator, Bi2Te3". In: *science* 325.5937 (2009), pp. 178–181.

[82] Wu-Pei Su, John Robert Schrieffer, and Alan J Heeger. "Solitons in polyacetylene". In: *Physical review letters* 42.25 (1979), p. 1698.

[83] A.J. Niemi and G.W. Semenoff. "Fermion number fractionization in quantum field theory". In: *Physics Reports* 135.3 (1986), pp. 99–193. ISSN: 0370-1573. DOI: https://doi.org/10.1016/0370-1573(86)90167-5. URL: https://www.sciencedirect.com/science/article/pii/0370157386901675.

[84] D. C. Tsui, H. L. Stormer, and A. C. Gossard. "Two-Dimensional Magnetotransport in the Extreme Quantum Limit". In: *Phys. Rev. Lett.* 48 (22 May 1982), pp. 1559–1562. DOI: 10.1103/PhysRevLett.48.1559. URL: https://link.aps.org/doi/10.1103/PhysRevLett.48.1559.

[85] D. K. Campbell and A. R. Bishop. "Solitons in polyacetylene and relativistic-field-theory models". In: *Phys. Rev. B* 24 (8 Oct. 1981), pp. 4859–4862. DOI: 10.1103/PhysRevB.24.4859. URL: https://link.aps.org/doi/10.1103/PhysRevB.24.4859.

[86] M. Z. Hasan and C. L. Kane. "Colloquium: Topological insulators". In: *Rev. Mod. Phys.* 82 (4 Nov. 2010), pp. 3045–3067. DOI: 10.1103/RevModPhys.82.3045. URL: https://link.aps.org/doi/10.1103/RevModPhys.82.3045.

[87] Xiao Yuan, M. Bowen, and P. S. Riseborough. "The Dirac equation as a model of topological insulators". In: *Philosophical Magazine* 100.10 (2020), pp. 1324–1354. DOI: 10.1080/14786435.2020.1726523. eprint: https://doi.org/10.1080/14786435.2020.1726523. URL: https://doi.org/10.1080/14786435.2020.1726523.

[88] Dimitris G. Angelakis, P. Das, and C. Noh. "Probing the topological properties of the Jackiw-Rebbi model with light". In: *Scientific Reports* 4.1 (Aug. 2014), p. 6110. ISSN: 2045-2322. DOI: 10.1038/srep06110. URL: https://doi.org/10.1038/srep06110.

[89] Truong X. Tran and Fabio Biancalana. "Linear and nonlinear photonic Jackiw-Rebbi states in interfaced binary waveguide arrays". In: *Phys. Rev. A* 96 (1 July 2017), p. 013831. DOI: 10.1103/PhysRevA.96.013831. URL: https://link.aps.org/doi/10.1103/PhysRevA.96.013831.

[90] Gabriel González. "Dirac Equation and Optical Wave Propagation in One Dimension". In: *physica status solidi (RRL) – Rapid Research Letters* 12.2 (2018), p. 1700357. DOI: https://doi.org/10.1002/pssr.201700357. eprint: https://onlinelibrary.wiley.com/doi/pdf/10.1002/pssr.201700357. URL: https://onlinelibrary.wiley.com/doi/abs/10.1002/pssr.201700357.

[91] Gabriel Gonzalez. *Dirac equation in one dimensional transformation optics*. 2017. DOI: 10.48550/ARXIV.1707.06743. URL: https://arxiv.org/abs/1707.06743.

[92] G. Gonzalez et al. "Electrostatic simulation of the Jackiw-Rebbi zero energy state". In: *Rev. Mex. Fis. E* 65.1 (2019), pp. 30–33.

[93] Farhad Khosravi, Todd Van Mechelen, and Zubin Jacob. "Dirac wire: Fermionic waveguides with longitudinal spin". In: *Phys. Rev. B* 100 (15 Oct. 2019), p. 155105. DOI: 10.1103/PhysRevB.100.155105. URL: https://link.aps.org/doi/10.1103/PhysRevB.100.155105.

[94] Yusuke Nishida, Luiz Santos, and Claudio Chamon. "Topological superconductors as nonrelativistic limits of Jackiw-Rossi and Jackiw-Rebbi models". In: *Phys. Rev. B* 82 (14 Oct. 2010), p. 144513. DOI: 10.1103/PhysRevB.82.144513. URL: https://link.aps.org/doi/10.1103/PhysRevB.82.144513.

[95] Alexei Kitaev. "Periodic table for topological insulators and superconductors". In: *AIP conference proceedings*. Vol. 1134. 1. American Institute of Physics. 2009, pp. 22–30.

[96] Andreas P Schnyder et al. "Classification of topological insulators and superconductors in three spatial dimensions". In: *Physical Review B* 78.19 (2008), p. 195125.

[97] Pavan Hosur, SA Parameswaran, and Ashvin Vishwanath. "Charge transport in Weyl semimetals". In: *Physical review letters* 108.4 (2012), p. 046602.

[98] AA Burkov and Leon Balents. "Weyl semimetal in a topological insulator multilayer". In: *Physical review letters* 107.12 (2011), p. 127205.

[99] AA Burkov, MD Hook, and Leon Balents. "Topological nodal semimetals". In: *Physical Review B* 84.23 (2011), p. 235126.

[100] Gang Xu et al. "Chern semimetal and the quantized anomalous Hall effect in HgCr 2 Se 4". In: *Physical review letters* 107.18 (2011), p. 186806.

[101] AA Burkov. "Chiral anomaly and transport in Weyl metals". In: *Journal of Physics: Condensed Matter* 27.11 (2015), p. 113201.

[102] Binghai Yan and Claudia Felser. "Topological materials: Weyl semimetals". In: *Annual Review of Condensed Matter Physics* 8 (2017), pp. 337–354.

[103] Di Xiao, Ming-Che Chang, and Qian Niu. "Berry phase effects on electronic properties". In: *Reviews of modern physics* 82.3 (2010), p. 1959.

[104] Holger Bech Nielsen and Masao Ninomiya. *No-go theorum for regularizing chiral fermions*. Tech. rep. Science Research Council, 1981.

[105] M Zahid Hasan et al. "Discovery of Weyl fermion semimetals and topological Fermi arc states". In: *Annual Review of Condensed Matter Physics* 8 (2017), pp. 289–309.

[106] Yong Xu, Fan Zhang, and Chuanwei Zhang. "Structured Weyl points in spin-orbit coupled fermionic superfluids". In: *Physical review letters* 115.26 (2015), p. 265304.

[107] NP Armitage, EJ Mele, and Ashvin Vishwanath. "Weyl and Dirac semimetals in three-dimensional solids". In: *Reviews of Modern Physics* 90.1 (2018), p. 015001.

[108] Tobias Meng and Leon Balents. "Weyl superconductors". In: *Physical Review B* 86.5 (2012), p. 054504.

[109] Grigory Bednik, AA Zyuzin, and AA Burkov. "Superconductivity in Weyl metals". In: *Physical Review B* 92.3 (2015), p. 035153.

[110] Yi Li and FDM Haldane. "Topological nodal Cooper pairing in doped Weyl metals". In: *Physical review letters* 120.6 (2018), p. 067003.

[111] Walter Greiner. "Quantum electrodynamics of strong fields". In: *Hadrons and Heavy Ions: Proceedings of the Summer School Held at the University of Cape Town January 16–27, 1984*. Springer, 2005, pp. 95–226.

[112] Jean-Noel Fuchs and Mark Oliver Goerbig. "Introduction to the physical properties of graphene". In: *Lecture notes* 10 (2008), pp. 11–12.

[113] S Weinberg. "The Quantum Theory of Fields I, Cambridge UP (1995)". In: *Physical Consequences of the Dirac Equation* 65 ().

[114] Erwin Schrödinger. "SCHRÖDINGER 1926C". In: *Annalen der Physik* 79 (1926), p. 734.

[115] Oskar Klein. "Quantentheorie und fünfdimensionale Relativitätstheorie". In: *Zeitschrift für Physik* 37.12 (1926), pp. 895–906.

[116] Walter Gordon. "Der comptoneffekt nach der schrödingerschen theorie". In: *Zeitschrift für Physik* 40.1-2 (1926), pp. 117–133.

[117] Paul Adrien Maurice Dirac. "The quantum theory of the electron". In: *Proceedings of the Royal Society of London. Series A, Containing Papers of a Mathematical and Physical Character* 117.778 (1928), pp. 610–624.

[118] Paul Adrien Maurice Dirac. "Quantised singularities in the electromagnetic field". In: *Proceedings of the Royal Society of London. Series A, Containing Papers of a Mathematical and Physical Character* 133.821 (1931), pp. 60–72.

[119] J Robert Oppenheimer. "On the theory of electrons and protons". In: *Physical Review* 35.5 (1930), p. 562.

[120] Carl D Anderson. "The apparent existence of easily deflectable positives". In: *Science* 76.1967 (1932), pp. 238–239.

[121] Claude Itzykson and Jean-Bernard Zuber. "Quantum field theory, McGraw-Hill, 1985". In: *SISTAKE A* (1985).

[122] Kenneth W-K Shung. "Lifetime effects in low-stage intercalated graphite systems". In: *Physical Review B* 34.2 (1986), p. 1264.

[123] Igor F Herbut. "Interactions and phase transitions on graphene's honeycomb lattice". In: *Physical review letters* 97.14 (2006), p. 146401.

[124] Jinwu Ye and Subir Sachdev. "Coulomb interactions at quantum hall critical points of systems in a periodic potential". In: *Physical review letters* 80.24 (1998), p. 5409.

[125] Hiroki Isobe and Naoto Nagaosa. "Renormalization effects on quasi-two-dimensional organic conductor α-(BEDT-TTF) 2I3". In: *Journal of the Physical Society of Japan* 81.11 (2012), p. 113704.

[126] DC Elias et al. "Dirac cones reshaped by interaction effects in suspended graphene". In: *Nature Physics* 7.9 (2011), pp. 701–704.

[127] Joaquín E Drut and Timo A Lähde. "Critical exponents of the semimetal-insulator transition in graphene: A Monte Carlo study". In: *Physical Review B* 79.24 (2009), p. 241405.

[128] Joaquin E Drut and Timo A Lähde. "Lattice field theory simulations of graphene". In: *Physical Review B* 79.16 (2009), p. 165425.

[129] Richard Brower, Claudio Rebbi, and David Schaich. "Hybrid Monte Carlo simulation on the graphene hexagonal lattice". In: *arXiv preprint arXiv:1204.5424* (2012).

[130] AH Castro Neto. "Charge density wave, superconductivity, and anomalous metallic behavior in 2D transition metal dichalcogenides". In: *Physical review letters* 86.19 (2001), p. 4382.

[131] NB Kopnin and EB Sonin. "BCS superconductivity of Dirac electrons in graphene layers". In: *Physical review letters* 100.24 (2008), p. 246808.

[132] Erhai Zhao and Arun Paramekanti. "BCS-BEC crossover on the two-dimensional honeycomb lattice". In: *Physical review letters* 97.23 (2006), p. 230404.

[133] Bruno Uchoa and AH Castro Neto. "Superconducting states of pure and doped graphene". In: *Physical review letters* 98.14 (2007), p. 146801.

[134] Hubert B Heersche et al. "Bipolar supercurrent in graphene". In: *Nature* 446.7131 (2007), pp. 56–59.

[135] F Miao et al. "Phase-coherent transport in graphene quantum billiards". In: *science* 317.5844 (2007), pp. 1530–1533.

[136] A Shailos et al. "Proximity effect and multiple Andreev reflections in few-layer graphene". In: *Europhysics Letters* 79.5 (2007), p. 57008.

[137] Xu Du, Ivan Skachko, and Eva Y Andrei. "Josephson current and multiple Andreev reflections in graphene SNS junctions". In: *Physical Review B* 77.18 (2008), p. 184507.

[138] Kostya S Novoselov et al. "Two-dimensional gas of massless Dirac fermions in graphene". In: *nature* 438.7065 (2005), pp. 197–200.

[139] Z Jiang et al. "Infrared spectroscopy of Landau levels of graphene". In: *Physical review letters* 98.19 (2007), p. 197403.

[140] Guohong Li and Eva Y Andrei. "Observation of Landau levels of Dirac fermions in graphite". In: *Nature physics* 3.9 (2007), pp. 623–627.

[141] Guohong Li, Adina Luican, and Eva Y Andrei. "Scanning tunneling spectroscopy of graphene on graphite". In: *Physical review letters* 102.17 (2009), p. 176804.

[142] Peng Cheng et al. "Landau quantization of topological surface states in Bi 2 Se 3". In: *Physical review letters* 105.7 (2010), p. 076801.

[143] T Hanaguri et al. "Momentum-resolved Landau-level spectroscopy of Dirac surface state in Bi 2 Se 3". In: *Physical Review B* 82.8 (2010), p. 081305.

[144] Tsuneya Ando, Takeshi Nakanishi, and Riichiro Saito. "Berry's phase and absence of back scattering in carbon nanotubes". In: *Journal of the Physical Society of Japan* 67.8 (1998), pp. 2857–2862.

[145] Thomas Dahm et al. "Nodal quasiparticle lifetimes in cuprate superconductors". In: *Physical Review B* 72.21 (2005), p. 214512.

[146] Pedram Roushan et al. "Topological surface states protected from backscattering by chiral spin texture". In: *Nature* 460.7259 (2009), pp. 1106–1109.

[147] John Stewart Bell and Roman W Jackiw. "A PCAC puzzle: $\pi^0 \to \gamma\gamma$ in the σ-model". In: *Nuovo cimento* 60.CERN-TH-920 (1969), pp. 47–61.

[148] Stephen L Adler. "Axial-vector vertex in spinor electrodynamics". In: *Physical Review* 177.5 (1969), p. 2426.

[149] Holger Bech Nielsen and Masao Ninomiya. "The Adler-Bell-Jackiw anomaly and Weyl fermions in a crystal". In: *Physics Letters B* 130.6 (1983), pp. 389–396.

[150] Pavan Hosur and Xiaoliang Qi. "Recent developments in transport phenomena in Weyl semimetals". In: *Comptes Rendus Physique* 14.9-10 (2013), pp. 857–870.

[151] Heon-Jung Kim et al. "Dirac versus Weyl fermions in topological insulators: Adler-Bell-Jackiw anomaly in transport phenomena". In: *Physical review letters* 111.24 (2013), p. 246603.

[152] Kenji Fukushima, Dmitri E Kharzeev, and Harmen J Warringa. "Chiral magnetic effect". In: *Physical Review D* 78.7 (2008), p. 074033.

[153] AA Burkov. "Giant planar Hall effect in topological metals". In: *Physical Review B* 96.4 (2017), p. 041110.

[154] Dmitri E Kharzeev et al. *Strongly interacting matter in magnetic fields: a guide to this volume*. Springer, 2013.

[155] *The Daily Science*. 2023. URL: `https://www.thedailyscience.org/new-intrinsic-nonlinear-planar-hall-effect-discovered.html` (visited on 02/02/2024).

[156] Julio Cesar Pérez-Pedraza, J E Barrios-Vargas, and A Raya. "Impact of impurities on the topological boundaries and edge state localization in a staggered chain of atoms: SSH model and its topoelectrical circuit realization". In: *Revista Mexicana de Física*. Vol. To be published. 2024.

[157] Klaus Von Klitzing. "The quantized Hall effect". In: *Reviews of Modern Physics* 58.3 (1986), p. 519.

[158] K v Klitzing, Gerhard Dorda, and Michael Pepper. "New method for high-accuracy determination of the fine-structure constant based on quantized Hall resistance". In: *Physical review letters* 45.6 (1980), p. 494.

[159] Horst L Stormer, Daniel C Tsui, and Arthur C Gossard. "The fractional quantum Hall effect". In: *Reviews of Modern Physics* 71.2 (1999), S298.

[160] Navketan Batra and Goutam Sheet. "Physics with Coffee and Doughnuts". In: *Resonance* 25.6 (June 2020), pp. 765–786. ISSN: 0973-712X. DOI: 10.1007/s12045-020-0995-x. URL: https://doi.org/10.1007/s12045-020-0995-x.

[161] János K. Asbóth, László Oroszlány, and András Pályi. *A Short Course on Topological Insulators*. Vol. 919. 2016. DOI: 10.1007/978-3-319-25607-8.

[162] Panagiotis Kotetes. *Topological Insulators*. 2053-2571. Morgan Claypool Publishers, 2019. ISBN: 978-1-68174-517-6. DOI: 10.1088/978-1-68174-517-6. URL: https://dx.doi.org/10.1088/978-1-68174-517-6.

[163] Alexei Kitaev. "Periodic table for topological insulators and superconductors". In: *AIP Conference Proceedings* 1134.1 (May 2009), pp. 22–30. ISSN: 0094-243X. DOI: 10.1063/1.3149495. eprint: https://pubs.aip.org/aip/acp/article-pdf/1134/1/22/11584243/22_1_online.pdf. URL: https://doi.org/10.1063/1.3149495.

[164] W. P. Su, J. R. Schrieffer, and A. J. Heeger. "Solitons in Polyacetylene". In: *Phys. Rev. Lett.* 42 (25 June 1979), pp. 1698–1701. DOI: 10.1103/PhysRevLett.42.1698. URL: https://link.aps.org/doi/10.1103/PhysRevLett.42.1698.

[165] W. P. Su, J. R. Schrieffer, and A. J. Heeger. "Soliton excitations in polyacetylene". In: *Phys. Rev. B* 22 (4 Aug. 1980), pp. 2099–2111. DOI: 10.1103/PhysRevB.22.2099. URL: https://link.aps.org/doi/10.1103/PhysRevB.22.2099.

[166] M. Z. Hasan and C. L. Kane. "Colloquium: Topological insulators". In: *Rev. Mod. Phys.* 82 (4 Nov. 2010), pp. 3045–3067. DOI: 10.1103/RevModPhys.82.3045. URL: https://link.aps.org/doi/10.1103/RevModPhys.82.3045.

[167] Xiao-Liang Qi and Shou-Cheng Zhang. "Topological insulators and superconductors". In: *Rev. Mod. Phys.* 83 (4 Oct. 2011), pp. 1057–1110. DOI: 10.1103/RevModPhys.83.1057. URL: https://link.aps.org/doi/10.1103/RevModPhys.83.1057.

[168] R. Shankar. *Topological Insulators – A review*. 2018. arXiv: 1804.06471 [cond-mat.str-el].

[169] Alan J Heeger et al. "Solitons in conducting polymers". In: *Reviews of Modern Physics* 60.3 (1988), p. 781.

[170] Lu Yu. *Solitons and polarons in conducting polymers*. World Scientific, 1988.

[171] Shinsei Ryu et al. "Topological insulators and superconductors: tenfold way and dimensional hierarchy". In: *New Journal of Physics* 12.6 (2010), p. 065010.

[172] Yu-Gui Peng et al. "Experimental demonstration of anomalous Floquet topological insulator for sound". In: *Nature communications* 7.1 (2016), p. 13368.

[173] Alvaro Gómez-León and Gloria Platero. "Floquet-Bloch theory and topology in periodically driven lattices". In: *Physical review letters* 110.20 (2013), p. 200403.

[174] Virginia Dal Lago, M Atala, and LEF Foa Torres. "Floquet topological transitions in a driven one-dimensional topological insulator". In: *Physical Review A* 92.2 (2015), p. 023624.

[175] Fangzhao Alex An, Eric J Meier, and Bryce Gadway. "Engineering a flux-dependent mobility edge in disordered zigzag chains". In: *Physical Review X* 8.3 (2018), p. 031045.

[176] Beatriz Pérez-González et al. "Interplay between long-range hopping and disorder in topological systems". In: *Physical Review B* 99.3 (2019), p. 035146.

[177] C Li et al. "Topological nodal points in two coupled Su-Schrieffer-Heeger chains". In: *Physical Review B* 96.12 (2017), p. 125418.

[178] J Jünemann et al. "Exploring interacting topological insulators with ultracold atoms: The synthetic Creutz-Hubbard model". In: *Physical Review X* 7.3 (2017), p. 031057.

[179] Ning Sun and Lih-King Lim. "Quantum charge pumps with topological phases in a Creutz ladder". In: *Physical Review B* 96.3 (2017), p. 035139.

[180] Chang-An Li et al. "Dirac states in an inclined two-dimensional Su-Schrieffer-Heeger model". In: *Physical Review Research* 4.2 (2022), p. 023193.

[181] Dizhou Xie et al. "Topological characterizations of an extended Su–Schrieffer–Heeger model". In: *npj Quantum Information* 5.1 (2019), p. 55.

[182] Linhu Li, Zhihao Xu, and Shu Chen. "Topological phases of generalized Su-Schrieffer-Heeger models". In: *Physical Review B* 89.8 (2014), p. 085111.

[183] Aayushi Agrawal and Jayendra N Bandyopadhyay. "Cataloging topological phases of N stacked Su-Schrieffer-Heeger chains by a systematic breaking of symmetries". In: *Physical Review B* 108.10 (2023), p. 104101.

[184] Jia-Rui Li et al. "Topological properties in non-Hermitian tetratomic Su-Schrieffer-Heeger lattices". In: *Physical Review Research* 4.2 (2022), p. 023009.

[185] A Sivan and M Orenstein. "Topology of multiple cross-linked Su-Schrieffer-Heeger chains". In: *Physical Review A* 106.2 (2022), p. 022216.

[186] J Zak. "Berry's phase for energy bands in solids". In: *Physical review letters* 62.23 (1989), p. 2747.

[187] Yonatan Betancur-Ocampo et al. *Twofold topological phase transitions induced by third-nearest-neighbor interactions in 1D chains*. 2023. arXiv: 2306.05595 [cond-mat.mtrl-sci].

[188] Bo Wang, Tian Chen, and Xiangdong Zhang. "Experimental observation of topologically protected bound states with vanishing Chern numbers in a two-dimensional quantum walk". In: *Physical Review Letters* 121.10 (2018), p. 100501.

[189] Chao Chen et al. "Observation of topologically protected edge states in a photonic two-dimensional quantum walk". In: *Physical review letters* 121.10 (2018), p. 100502.

[190] Meng Xiao et al. "Geometric phase and band inversion in periodic acoustic systems". In: *Nature Physics* 11.3 (2015), pp. 240–244.

[191] BK Stuhl et al. "Visualizing edge states with an atomic Bose gas in the quantum Hall regime". In: *Science* 349.6255 (2015), pp. 1514–1518.

[192] Eric J Meier, Fangzhao Alex An, and Bryce Gadway. "Observation of the topological soliton state in the Su–Schrieffer–Heeger model". In: *Nature communications* 7.1 (2016), p. 13986.

[193] Eric J Meier et al. "Observation of the topological Anderson insulator in disordered atomic wires". In: *Science* 362.6417 (2018), pp. 929–933.

[194] Han Cai et al. "Experimental observation of momentum-space chiral edge currents in room-temperature atoms". In: *Physical Review Letters* 122.2 (2019), p. 023601.

[195] Nathan Goldman, Jan C Budich, and Peter Zoller. "Topological quantum matter with ultracold gases in optical lattices". In: *Nature Physics* 12.7 (2016), pp. 639–645.

[196] Gregor Jotzu et al. "Experimental realization of the topological Haldane model with ultracold fermions". In: *Nature* 515.7526 (2014), pp. 237–240.

[197] Motohiko Ezawa. "Electric-circuit simulation of the Schrödinger equation and non-Hermitian quantum walks". In: *Phys. Rev. B* 100 (16 Oct. 2019), p. 165419. DOI: 10.1103/PhysRevB.100.165419. URL: https://link.aps.org/doi/10.1103/PhysRevB.100.165419.

[198] Russell Yang Qi Xun. "Topological Circuits - A Stepping Stone in the Topological Revolution". In: *Molecular Frontiers Journal* 04.Supp01 (2020), pp. 9–14. DOI: 10.1142/S2529732520970020. eprint: https://doi.org/10.1142/S2529732520970020. URL: https://doi.org/10.1142/S2529732520970020.

[199] Alexandre Blais et al. "Circuit quantum electrodynamics". In: *Rev. Mod. Phys.* 93 (2 May 2021), p. 025005. DOI: 10.1103/RevModPhys.93.025005. URL: https://link.aps.org/doi/10.1103/RevModPhys.93.025005.

[200] Ching Hua Lee et al. "Topolectrical Circuits". In: *Communications Physics* 1.1 (July 2018), p. 39. ISSN: 2399-3650. DOI: 10.1038/s42005-018-0035-2. URL: https://doi.org/10.1038/s42005-018-0035-2.

[201] Erhai Zhao. "Topological circuits of inductors and capacitors". In: *Annals of Physics* 399 (2018), pp. 289–313. ISSN: 0003-4916. DOI: https://doi.org/10.1016/j.aop.2018.10.006. URL: https://www.sciencedirect.com/science/article/pii/S0003491618302689.

[202] Junkai Dong, Vladimir Juri či ć, and Bitan Roy. "Topolectric circuits: Theory and construction". In: *Phys. Rev. Res.* 3 (2 Apr. 2021), p. 023056. DOI: 10.1103/PhysRevResearch.3.023056. URL: https://link.aps.org/doi/10.1103/PhysRevResearch.3.023056.

[203] Russell Yang Qi Xun. "Topological Circuits-A Stepping Stone in the Topological Revolution". In: *Molecular Frontiers Journal* 4.Supp01 (2020), pp. 9–14.

[204] Jia Ningyuan et al. "Time-and site-resolved dynamics in a topological circuit". In: *Physical Review X* 5.2 (2015), p. 021031.

[205] Weiwei Zhu et al. "Simulating quantum spin Hall effect in the topological Lieb lattice of a linear circuit network". In: *Physical Review B* 97.7 (2018), p. 075310.

[206] phythTB. *Python Tight Binding*. 2016. URL: https://www.physics.rutgers.edu/pythtb/ (visited on 09/18/2023).

[207] PySpice. *PySpice*. 2021. URL: https://pypi.org/project/PySpice/ (visited on 05/15/2021).

[208] Ugo Fano. "Effects of configuration interaction on intensities and phase shifts". In: *Physical review* 124.6 (1961), p. 1866.

[209] Bo Lv et al. "Analysis and modeling of Fano resonances using equivalent circuit elements". In: *Scientific reports* 6.1 (2016), p. 31884.

[210] M. Ilchenko and A. Zhivkov. "Bridge Equivalent Circuits for Microwave Filters and Fano Resonance". In: *Advances in Information and Communication Technologies*. Ed. by Mykhailo Ilchenko, Leonid Uryvsky, and Larysa Globa. Cham: Springer International Publishing, 2019, pp. 278–298. ISBN: 978-3-030-16770-7.

[211] Mario I Molina. "Fano resonances in an electrical lattice". In: *Physics Letters A* 428 (2022), p. 127948.

[212] József Cserti, Gábor Széchenyi, and Gyula Dávid. "Uniform tiling with electrical resistors". In: *Journal of Physics A: Mathematical and Theoretical* 44.21 (2011), p. 215201.

[213] Leslie L. Foldy and Siegfried A. Wouthuysen. "On the Dirac Theory of Spin 1/2 Particles and Its Non-Relativistic Limit". In: *Phys. Rev.* 78 (1 Apr. 1950), pp. 29–36. DOI: 10.1103/PhysRev.78.29. URL: https://link.aps.org/doi/10.1103/PhysRev.78.29.

[214] Roman Jackiw and Cláudio Rebbi. "Solitons with fermion number 1/2". In: *Physical Review D* 13.12 (1976), p. 3398.

[215] David Valenzuela, Julio César Pérez Pedraza, and Alfredo Raya. "Non-relativistic representation of the Jackiw-Rebbi soliton". In: *Revista Mexicana de Física E* 20.2 Jul-Dec (2023), pp. 020501–1.

[216] Tsung L. Li and Kelin J. Kuhn. "Band-offset ratio dependence on the effective-mass Hamiltonian based on a modified profile of the GaAs-$Al_xGa_{1-x}As$ quantum well". In: *Phys. Rev. B* 47 (19 May 1993), pp. 12760–12770. DOI: 10.1103/PhysRevB.47.12760. URL: https://link.aps.org/doi/10.1103/PhysRevB.47.12760.

[217] F. S. A. Cavalcante et al. "Form of the quantum kinetic-energy operator with spatially varying effective mass". In: *Phys. Rev. B* 55 (3 Jan. 1997), pp. 1326–1328. DOI: 10.1103/PhysRevB.55.1326. URL: https://link.aps.org/doi/10.1103/PhysRevB.55.1326.

[218] Shen Shun-Qing Shen. *Topological Insulators. Dirac Equation in Condensed Matters*. 1st ed. Springer Berlin, Heidelberg, 2012, p. 225.

[219] Edward Witten. "Dynamical breaking of supersymmetry". In: *Nuclear Physics B* 188.3 (1981), pp. 513–554.

[220] Juan D García-Muñoz, Julio Cesar Pérez-Pedraza, and A Raya. "Dirac materials in parallel electromagnetic fields generated by supersymmetry". In: *Journal of Physics: Conference Series*. Vol. 2667. 1. IOP Publishing. 2023, p. 012053.

[221] Julio Cesar Pérez-Pedraza, Juan D García-Muñoz, and A Raya. "Dirac materials in parallel non-uniform electromagnetic fields generated by SUSY: A new class of chiral Planar Hall Effect?" In: *arXiv preprint arXiv:2306.16399* (2023).

[222] Claude Cohen-Tannoudji, Bernard Diu, and Franck Laloë. *Quantum mechanics; 1st ed.* Trans. of : Mécanique quantique. Paris : Hermann, 1973. New York, NY: Wiley, 1977. URL: https://cds.cern.ch/record/101367.

[223] Jun John Sakurai. *Modern quantum mechanics; rev. ed.* Reading, MA: Addison-Wesley, 1994. URL: https://cds.cern.ch/record/1167961.

[224] David Griffiths. *Introduction of Quantum Mechanics*. Prentice Hall, Inc., 1995.

[225] L. Landau. "Diamagnetismus der Metalle". In: *Zeitschrift für Physik* 64.9 (Sept. 1930), pp. 629–637. ISSN: 0044-3328. DOI: 10.1007/BF01397213. URL: https://doi.org/10.1007/BF01397213.

[226] Vladimir A. Miransky and Igor A. Shovkovy. "Quantum field theory in a magnetic field: From quantum chromodynamics to graphene and Dirac semimetals". In: *Physics Reports* 576 (2015). Quantum field theory in a magnetic field: From quantum chromodynamics to graphene and Dirac semimetals, pp. 1–209. ISSN: 0370-1573. DOI: https://doi.org/10.1016/j.physrep.2015.02.003. URL: https://www.sciencedirect.com/science/article/pii/S0370157315001775.

[227] Tsuneya Ando, Yukio Matsumoto, and Yasutada Uemura. "Theory of Hall Effect in a Two-Dimensional Electron System". In: *Journal of the Physical Society of Japan* 39.2 (1975), pp. 279–288. DOI: 10.1143/JPSJ.39.279. eprint: https://doi.org/10.1143/JPSJ.39.279. URL: https://doi.org/10.1143/JPSJ.39.279.

[228] K. v. Klitzing, G. Dorda, and M. Pepper. "New Method for High-Accuracy Determination of the Fine-Structure Constant Based on Quantized Hall Resistance". In: *Phys. Rev. Lett.* 45 (6 Aug. 1980), pp. 494–497. DOI: 10.1103/PhysRevLett.45.494. URL: https://link.aps.org/doi/10.1103/PhysRevLett.45.494.

[229] D. C. Tsui, H. L. Stormer, and A. C. Gossard. "Two-Dimensional Magnetotransport in the Extreme Quantum Limit". In: *Phys. Rev. Lett.* 48 (22 May 1982), pp. 1559–1562. DOI: 10.1103/PhysRevLett.48.1559. URL: https://link.aps.org/doi/10.1103/PhysRevLett.48.1559.

[230] R. B. Laughlin. "Quantized Hall conductivity in two dimensions". In: *Phys. Rev. B* 23 (10 May 1981), pp. 5632–5633. DOI: 10.1103/PhysRevB.23.5632. URL: https://link.aps.org/doi/10.1103/PhysRevB.23.5632.

[231] K. S. Novoselov et al. "Two-dimensional gas of massless Dirac fermions in graphene". In: *Nature* 438.7065 (Nov. 2005), pp. 197–200. ISSN: 1476-4687. DOI: 10.1038/nature04233. URL: https://doi.org/10.1038/nature04233.

[232] Yuanbo Zhang et al. "Experimental observation of the quantum Hall effect and Berry's phase in graphene". In: *Nature* 438.7065 (Nov. 2005), pp. 201–204. ISSN: 1476-4687. DOI: 10.1038/nature04235. URL: https://doi.org/10.1038/nature04235.

[233] V. P. Gusynin and S. G. Sharapov. "Unconventional Integer Quantum Hall Effect in Graphene". In: *Phys. Rev. Lett.* 95 (14 Sept. 2005), p. 146801. DOI: 10.1103/PhysRevLett.95.146801. URL: https://link.aps.org/doi/10.1103/PhysRevLett.95.146801.

[234] A. K. Geim and K. S. Novoselov. "The rise of graphene". In: *Nature Materials* 6.3 (Mar. 2007), pp. 183–191. ISSN: 1476-4660. DOI: 10.1038/nmat1849. URL: https://doi.org/10.1038/nmat1849.

[235] RB Laughlin. "The relationship between high-temperature superconductivity and the fractional quantum Hall effect". In: *Science* 242.4878 (1988), pp. 525–533.

[236] J. D. Brandenburg, W. Zha, and Z. Xu. "Mapping the electromagnetic fields of heavy-ion collisions with the Breit-Wheeler process". In: *The European Physical Journal A* 57.10 (Oct. 2021), p. 299. ISSN: 1434-601X. DOI: 10.1140/epja/s10050-021-00595-5. URL: https://doi.org/10.1140/epja/s10050-021-00595-5.

[237] Dmitri E. Kharzeev, Larry D. McLerran, and Harmen J. Warringa. "The Effects of topological charge change in heavy ion collisions: 'Event by event P and CP violation'". In: *Nucl. Phys. A* 803 (2008), pp. 227–253. DOI: 10.1016/j.nuclphysa.2008.02.298. arXiv: 0711.0950 [hep-ph].

[238] Dmitri E. Kharzeev. "The Chiral Magnetic Effect and anomaly-induced transport". In: *Progress in Particle and Nuclear Physics* 75 (2014), pp. 133–151. ISSN: 0146-6410. DOI: https://doi.org/10.1016/j.ppnp.2014.01.002. URL: https://www.sciencedirect.com/science/article/pii/S0146641014000039.

[239] Kenji Fukushima, Dmitri E. Kharzeev, and Harmen J. Warringa. "Chiral magnetic effect". In: *Phys. Rev. D* 78 (7 Oct. 2008), p. 074033. DOI: 10.1103/PhysRevD.78.074033. URL: https://link.aps.org/doi/10.1103/PhysRevD.78.074033.

[240] Mohamed Abdallah et al. "Search for the chiral magnetic effect with isobar collisions at $\sqrt{s_{NN}}$=200 GeV by the STAR Collaboration at the BNL Relativistic Heavy Ion Collider". In: *Phys. Rev. C* 105.1 (2022), p. 014901. DOI: 10.1103/PhysRevC.105.014901. arXiv: 2109.00131 [nucl-ex].

[241] Volker Koch et al. "Status of the chiral magnetic effect and collisions of isobars". In: *Chin. Phys. C* 41.7 (2017), p. 072001. DOI: 10.1088/1674-1137/41/7/072001. arXiv: 1608.00982 [nucl-th].

[242] Qiang Li et al. "Chiral magnetic effect in ZrTe5". In: *Nature Physics* 12.6 (June 2016), pp. 550–554. ISSN: 1745-2481. DOI: 10.1038/nphys3648. URL: https://doi.org/10.1038/nphys3648.

[243] Cai-Zhen Li et al. "Giant negative magnetoresistance induced by the chiral anomaly in individual Cd3As2 nanowires". In: *Nature communications* 6.1 (2015), p. 10137.

[244] Guolin Zheng et al. "Transport evidence for the three-dimensional Dirac semimetal phase in $ZrTe_5$". In: *Phys. Rev. B* 93 (11 Mar. 2016), p. 115414. DOI: 10.1103/PhysRevB.93.115414. URL: https://link.aps.org/doi/10.1103/PhysRevB.93.115414.

[245] Xiaochun Huang et al. "Observation of the Chiral-Anomaly-Induced Negative Magnetoresistance in 3D Weyl Semimetal TaAs". In: *Phys. Rev. X* 5 (3 Aug. 2015), p. 031023. DOI: 10.1103/PhysRevX.5.031023. URL: https://link.aps.org/doi/10.1103/PhysRevX.5.031023.

[246] Shi-Han Zheng et al. "Origin of planar Hall effect on the surface of topological insulators: Tilt of Dirac cone by an in-plane magnetic field". In: *Phys. Rev. B* 101 (4 Jan. 2020), p. 041408. DOI: 10.1103/PhysRevB.101.041408. URL: https://link.aps.org/doi/10.1103/PhysRevB.101.041408.

[247] S. Nandy et al. "Chiral Anomaly as the Origin of the Planar Hall Effect in Weyl Semimetals". In: *Phys. Rev. Lett.* 119 (17 Oct. 2017), p. 176804. DOI: 10.1103/PhysRevLett.119.176804. URL: https://link.aps.org/doi/10.1103/PhysRevLett.119.176804.

[248] A. Martín-Ruiz, M. Cambiaso, and L. F. Urrutia. "The magnetoelectric coupling in electrodynamics". In: *International Journal of Modern Physics A* 34.28 (2019), p. 1941002. DOI: 10.1142/S0217751X19410021. eprint: https://doi.org/10.1142/S0217751X19410021. URL: https://doi.org/10.1142/S0217751X19410021.

[249] E. McCann and M. Koshino. "The electronic properties of bilayer graphene". In: *Rep. Prog. Phys.* 76 (2013), p. 056503. DOI: 10.1088/0034-4885/76/5/056503.

[250] Andrei Shytov et al. "Atomic collapse, Lorentz boosts, Klein scattering, and other quantum-relativistic phenomena in graphene". In: *Solid State Communications* 149.27 (2009). Recent Progress in Graphene Studies, pp. 1087–1093. ISSN: 0038-1098. DOI: https://doi.org/10.1016/j.ssc.2009.02.043. URL: https://www.sciencedirect.com/science/article/pii/S0038109809001434.

[251] G Margía et al. "The electron propagator in external electromagnetic fields in lower dimensions". In: *Am. J. Phys* 78 (2010), pp. 700–707.

[252] S. Kuru, J. Negro, and L. M. Nieto. "Exact analytic solutions for a Dirac electron moving in graphene under magnetic fields". In: *J. Phys.: Condens. Matter* 21 (2009), p. 455305. DOI: 10.1088/0953-8984/21/45/455305.

[253] P. Ghosh and P. Roy. "Bound states in graphene via Fermi velocity modulation". In: *The European Physical Journal Plus* 132.1 (Jan. 2017), p. 32. ISSN: 2190-5444. DOI: 10.1140/epjp/i2017-11323-2. URL: https://doi.org/10.1140/epjp/i2017-11323-2.

[254] A. Gangopadhyaya, J. Mallow, and C. Rasinariu. *Supersymmetric Quantum Mechanics*. Second. Singapore: World Scientific, 2018.

[255] G. Junker. *Supersymmetric Methods in Quantum, Statistical and Solid State Physics*. Second. Bristol: IOP Publishing Ltd, 2019.

[256] D. J. Fernández. "Trends in Supersymmetric Quantum Mechanics". In: *Integrability, Supersymmetry and Coherent States: A Volume in Honour of Professor Véronique Hussin*. Ed. by Şengül Kuru, Javier Negro, and Luis M. Nieto. Cham: Springer International Publishing, 2019, pp. 37–68. ISBN: 978-3-030-20087-9. DOI: 10.1007/978-3-030-20087-9_2. URL: https://doi.org/10.1007/978-3-030-20087-9_2.

[257] Tarun Kanti Ghosh. "Exact solutions for a Dirac electron in an exponentially decaying magnetic field". In: *Journal of Physics: Condensed Matter* 21.4 (Dec. 2008), p. 045505. DOI: 10.1088/0953-8984/21/4/045505. URL: https://dx.doi.org/10.1088/0953-8984/21/4/045505.

[258] P Ghosh and P Roy. "Dirac equation in (1 + 1) dimensional curved spacetime: Bound states and bound states in continuum". In: *Physica Scripta* 96.2 (Dec. 2020), p. 025303. DOI: 10.1088/1402-4896/abce38. URL: https://dx.doi.org/10.1088/1402-4896/abce38.

[259] David J. Fernández C., Juan D. García M., and Daniel O-Campa. "Electron in bilayer graphene with magnetic fields leading to shape invariant potentials". In: *J. Phys. A: Math. Theor.* 53.43 (Oct. 2020), p. 435202. DOI: 10.1088/1751-8121/abb6ad. URL: https://doi.org/10.1088/1751-8121/abb6ad.

[260] David J Fernandez, Juan Domingo García, and Daniel Ortiz Campa. "Bilayer graphene in magnetic fields generated by supersymmetry". In: *Journal of Physics A: Mathematical and Theoretical* (Apr. 2021). DOI: 10.1088/1751-8121/abf870. URL: https://doi.org/10.1088/1751-8121/abf870.

[261] David J. Fernández C. and Juan D. García-Muñoz. "Graphene in complex magnetic fields". In: *The European Physical Journal Plus* 137.9 (Sept. 2022), p. 1013. ISSN: 2190-5444. DOI: 10.1140/epjp/s13360-022-03221-5. URL: https://doi.org/10.1140/epjp/s13360-022-03221-5.

[262] C-L Ho and P Roy. "On zero energy states in graphene". In: *Europhysics Letters* 108.2 (2014), p. 20004.

[263] Axel Schulze-Halberg and Pinaki Roy. "Construction of zero-energy states in graphene through the supersymmetry formalism". In: *Journal of Physics A: Mathematical and Theoretical* 50.36 (2017), p. 365205.

[264] Ali Mostafazadeh. "Pseudo-Hermiticity versus PT symmetry: The necessary condition for the reality of the spectrum of a non-Hermitian Hamiltonian". In: *Journal of Mathematical Physics* 43.1 (2002), pp. 205–214. DOI: 10.1063/1.1418246. eprint: https://doi.org/10.1063/1.1418246. URL: https://doi.org/10.1063/1.1418246.

[265] Ali Mostafazadeh. "Pseudo-Hermiticity versus PT-symmetry. II. A complete characterization of non-Hermitian Hamiltonians with a real spectrum". In: *Journal of Mathematical Physics* 43.5 (2002), pp. 2814–2816.

[266] Suvendu Ghosh et al. "Chirality-dependent planar Hall effect in inhomogeneous Weyl semimetals". In: *Phys. Rev. B* 102 (12 Sept. 2020), p. 121105. DOI: 10.1103/PhysRevB.102.121105. URL: https://link.aps.org/doi/10.1103/PhysRevB.102.121105.

[267] Chao-Xing Liu, Peng Ye, and Xiao-Liang Qi. "Chiral gauge field and axial anomaly in a Weyl semimetal". In: *Phys. Rev. B* 87 (23 June 2013), p. 235306. DOI: 10.1103/PhysRevB.87.235306. URL: https://link.aps.org/doi/10.1103/PhysRevB.87.235306.

[268] N Levy et al. "Strain-induced pseudo–magnetic fields greater than 300 tesla in graphene nanobubbles". In: *Science* 329.5991 (2010), pp. 544–547.

[269] Nikolai N Klimov et al. "Electromechanical properties of graphene drumheads". In: *Science* 336.6088 (2012), pp. 1557–1561.

[270] Alexey A Gorlach et al. "Photonic Jackiw-Rebbi states in all-dielectric structures controlled by bianisotropy". In: *Physical Review B* 99.20 (2019), p. 205122.

[271] Sayan Jana, Arijit Saha, and Sourin Das. "Jackiw-Rebbi zero modes in non-uniform topological insulator nanowire". In: *Physical Review B* 100.8 (2019), p. 085428.

[272] Leopold Infeld and TE Hull. "The factorization method". In: *Reviews of modern Physics* 23.1 (1951), p. 21.

[273] PA Deift. "Applications of a commutation formula". In: (1978).

[274] Robert Wayne Carroll. *Transmutation and operator differential equations*. Elsevier, 1979.

[275] Georg Junker. *Supersymmetric methods in quantum, statistical and solid state physics*. IOP Publishing Bristol, 2019.